

Synthesis and properties of heterostructures in nanowires and 2-D materials

Présentée le 26 janvier 2022

Faculté des sciences et techniques de l'ingénieur
Laboratoire des matériaux semiconducteurs
Programme doctoral en science et génie des matériaux

pour l'obtention du grade de Docteur ès Sciences

par

Akshay BALGARKASHI

Acceptée sur proposition du jury

Dr A. Hessler-Wyser, présidente du jury
Prof. A. Fontcuberta i Morral, directrice de thèse
Dr Ph. Caroff, rapporteur
Dr E. Alarcón-Lladó, rapporteuse
Dr A. Magrez, rapporteur

Nothing in life is to be feared,
it is only to be understood.
— Marie Curie

To my grandmother, my family and my teachers...

Acknowledgements

The last four years have been an incredibly enriching experience to say the least. This thesis was made possible due to the support of many individuals who made a direct or indirect contribution, both professionally and otherwise.

Firstly, I would like to express my heartfelt gratitude to **Anna Fontcuberta i Morral** for offering me the opportunity to pursue a PhD in her group. She offered me not only scientific guidance but a great deal of personal and emotional support. Her compassion, selflessness and patience is a source of inspiration to me. Thank you for helping me grow as a scientist and a person. I admire her dedication towards various responsibilities but always making her students a priority. Thank you for being such a caring mentor even during difficult times. Thank you for everything, Anna!

I would like to thank members of the jury **Aïcha Hessler, Arnaud Magrez, Philippe Caroff and Esther Alarcon-Llado** for agreeing to be on my PhD defense committee and taking time to review my thesis manuscript. I look forward to the discussion.

I would like to acknowledge all my collaborators within and outside EPFL. I thank **Christophe Couteau** for hosting me during my secondment in Troyes. **Mackrine Nahra** for help with the optical measurements. Thank you **Andres Castellanos** and **Riccardo Frisenda** for welcoming me in Madrid and the collaboration on viscoelastic stamping. Special thank you to **Paulina Plochocka** for the fruitful collaboration on the 2-D project and dedicating significant lab resources for the measurements. Thanks are due to **Alessandro Surrente** for the collaboration, discussions and insights on the 2-D project. I would like to specially thank **Jakub Jasiński** for the measurements, discussions and help with countless requests for data.

I would like to thank **Mitali Banerjee** for making the experimental work on the 2-D project possible at EPFL. Thank you for being a caring mentor and a friend to me. **Jin**, for the countless hours you spent optimizing exfoliation and lending us your expertise. **Paritosh Karnatak** for the many insights and useful discussions during your visit to EPFL. **Mario di Luca**, it was a pleasure spending time with you during your stay at EPFL.

I would like to acknowledge funding through **project LIMQUET** for the first three years of my PhD and **SNSF** for funding during the final year.

I would like to thank the **LIMQUET co-ordinators** for managing the project and organizing the training schools and workshops in nice locations. All LIMQUET **ESRs** for the memorable times. **NCCR-QSIT** for the scientific workshops in Arosa.

Acknowledgements

These four years at LMSC were so much fun because of the people in the lab. I would like to thank: **Monika Salas** for all the help and support with the administration. Everything at LMSC goes so smoothly, but this is not possible without your tireless efforts behind the scenes. **Luca Francaviglia** for mentoring me during the first year of my PhD. Thank you for always being there to answer my questions and support during my candidacy. **Dmitry Mikulik**, though we did not get a chance to collaborate much, I appreciated being able to discuss many aspects of device fabrication and cleanroom processing with you. **Jelena Vukajlovic-Plestina** for your lively presence in the lab. I will remember watching the football world cup finals at your place. **Pablo Romero-Gómez** for the nice interactions.

The MBE gang: **Jean-Baptiste Leran**, thank you for leading us in keeping the MBE up and running. I admire your no non-sense approach to fixing problems with the MBE. I cannot recall how many times I have needed your assistance around the lab. I will cherish the tennis games with you. Thanks to you and **Melanie** for your generosity hosting me at your chalet. **Martin Friedl**, you were my go to person in case of any scientific questions on MBE growth. I also appreciated our spiritual discussions about meditation and Buddhism. Thanks to you and **Irene** for organizing the Indian dinner. **Wonjong Kim**, it was so much fun sharing the same office with you for three years. Thank you for optimizing the growth of nanowire arrays. All my work has depended on that. We also had some great times outside the lab, be it going for climbing or dinner outings. **Lucas Güniat**, I could benefit from your valuable insights on MBE growth. I admire your unique enthusiasm for small things in life. It was fun sharing the same house for a year. Thank you for always helping me navigate general aspects of life in Switzerland. **Didem Dede**, thank you for our many discussions about growth. Thanks for bringing a positive energy and enthusiasm to the lab and being a great friend to me. **Nicholas Morgan**, I have learnt how to deal with difficult problems with a smile from you. Thanks for bringing an American spirit to the lab and sharing your love for spicy food.

Santhanu Ramanandan, you made a significant contribution to the first part of my work, thank you for that. I admire your passion and drive to solve problems. Thanks for your energetic presence around the lab and enriching discussions. I will miss the competitive carrom games.

Mirjana Dimitrievska and **Valerio Piazza**, thanks for making the second part of my thesis work possible. **Mira**, you have been an incredible mentor to me, with whom I could share many insights about science and life in general. Your strength is an inspiration to me. **Valerio**, it has been a pleasure working with you. You have guided me through some tough times at the end of my thesis. Thank you for always lifting my spirit. For this, I am truly grateful.

Nicolas Tappy, thanks for sharing your immense knowledge of optics and CL with me and always being there to help. Thanks also for your support on a personal level. I will cherish our friendship very much. **Elias Stutz**, thank you for lending your expertise and invaluable help and patience in making the Raman and PL setups work. Thanks for sharing some great times together. **Rajrupa Paul**, I found in you a great friend and colleague in both good and bad times. **Andrea Giunto**, I thoroughly enjoyed all our collaborations and the insights you bring

while approaching a scientific problem. Thanks for sharing a similar passion for sports. **Anna Kukolova**, thanks for your lively presence in the lab and sharing some good times. Thanks for inviting us to the new years party. **Lea Ghisalberti**, I enjoyed our initial collaboration on the In droplets and could benefit from your theoretical insights. Thanks for being a fellow meditator and the nice philosophical discussions we had. **Mahdi Zamani**, thank you for the scientific insights you brought to the lab and always asking so many important questions. **Simon Escobar Steinvall**, thank you for lending your expertise in electron microscopy and sharing your love for Indian food. **Nuño Amador-Mendez**, what can I say! Even when you were visiting EPFL, you always felt like a lab member (yes, I believe you are a part of LMSC!). Thank you for coming to my wedding and welcoming me in Paris.

Claire Blaga, thanks for making the collaboration on the 2-D project so much fun. Thanks for the funny banter around the lab and sharing my passion for badminton. **Michele Zandrini**, it was nice collaborating with you on the nanowire growths and fixing issues together. **Antonia Gundel Hager**, though we did not get a chance to collaborate much, it was nice to have discussions about science and yoga with you. Thanks for sharing some nice badminton games. **Oscar Garcia**, **Ignasi Mundó Tijeras**, **Christian Jürgensen** for some nice hikes and trips during my first year. **Léo Garin** for hosting me in Neuchatel and for a great hike. **Mintae Chung** and **Sho Watanabe**, thank you for some great times in Lausanne. Special thank you to all LMGN group members for the nice interactions. Thank you to PBL group members **Hale Bila** and **Eva Kurisinkal** for your energetic presence next to the lab. **Eva**, thanks for the support and nice chats in the corridor.

I would like to thank all my semester students **Elif Nur Dayi**, **Rachel Wong Min**, **Zsófia Sajo**, **Pranav Kulkarni** and **Mohammadhossein Montazerian** for their contributions. I hope you could learn from me as much as I could learn from you.

I would like to thank the **CMi** staff for keeping the cleanroom up and running so we can carry out our research work smoothly. Special thanks to **CIME** staff at EPFL for scientific and technical support with electron microscopy.

I also looked forward to life outside the lab which was a lot more fun with the **Yuva-Indians** community at EPFL. Special thanks to **Mukeshchand Thakur** who started the PhD journey with me and has been a great friend to discuss science and life. **Pranit Iyengar**, **Sagar Joshi** and **Nagabhushan Hegde** for the memorable trips to Croatia and Ticino. **Shreyas Joglekar** for bringing his musical aura around us. Rest of the Indian community at EPFL and in Lausanne for striving to keep the Indian spirit alive in Switzerland.

Some more people have contributed to this journey who need special mention. Special thanks to this lovely couple in Troyes, **Anisha Gokarna** and her husband **Gérard Barreau** for a very warm and welcoming stay in Troyes. **Sambhav Paul** for going out of his way to help me during my visit to Troyes. **Ralf** and **Claude Schafhirt** for welcoming me in their home for the first six months in Lausanne. Ralf, it was great to share our interest in tennis and fandom of Roger Federer. Claude, thank you for your kindness and care. Then I spent an unforgettable year in the Cats' house. Thank you **Beatrix Mokhtari** for making this possible and caring for us.

Acknowledgements

Guillaume, Merlin, Armin and Sam for the nice times. And special thanks to **Filou**, my stress buster.

I am forever indebted to Acharya **S. N. Goenka** for his teachings of Vipassana. It has helped me become a better human being and keep my sanity during difficult times.

All this would not have been possible without the strongest pillar, my family. My grandmother, **Padma Maiya** who was my first tutor. My parents **Mohan and Meenal Balgarkashi** who have raised me with such high morals and values. No matter where I was, a shadow of their blessings has always been on me. They have always valued and encouraged the pursuit of education and been supportive of my decisions. Thank you for everything! My brother, **Tanay** who I can always talk to. I would very much like to thank the rest of my family for their immense love and support.

Lastly my better half, **Mounika**. I know times have been unusually difficult for the past two years. But your constant love and support is what kept me going. I only hope I could make it easier for you. Thank you for everything you have done for me.

Lausanne, January 4, 2022

A. B.

Abstract

Modern solid-state devices were made possible by the discovery of semiconductor heterostructures. Heterostructures offer the ability to fabricate low-dimensional nanostructures such as quantum dots which can restrain carriers in all three-directions. Quantum dots as single photon sources can be used as building blocks in quantum photonics and information processing applications. In this thesis, we explore heterostructures in nanowires and 2-D materials towards fabrication of quantum dots.

In the first part, we show how facet-driven nanostructure self-assembly can be used to grow axial and radial QDs in lattice-mismatched NW heterostructures. We investigate the growth of InAs/GaAs nanowire heterostructure arrays on Si substrates using the Ga-catalyzed method. We show how the nanowire tip morphology affects the formation of axial In(Ga)As clusters. The occurrence of In-rich clusters on the nanowires is elucidated by electron microscopy. We also show how the In(Ga)As cluster formation on the nanowire sidewalls is driven by the convex nature of the {11-2} corner facets. Cathodoluminescence and photoluminescence maps close to the NW tip evidence the presence of optically active emission centers along the NW sidewalls.

The second part is dedicated to heterostructures using monolayer 2-D transition-metal dichalcogenides. Firstly, we study the heterojunction between monolayer MoS₂ and gold. We provide a detailed understanding of the microscopic origins behind Raman mode splitting in monolayer MoS₂ exfoliated on gold substrates. We show that splitting in the Raman modes is a convolution of two effects: structural perturbations in MoS₂ due to the Au-S interaction and breaking of symmetry rules by the metallic plasmons. We confirm the proposed hypothesis by using Al as the metal which does not show any peak splitting.

In the last part, we successfully combine monolayer MoS₂ with a GaAs NW array as a first step towards integrating monolayer 2-D materials with III-V nanowire arrays. Using detailed structural investigation, we show three different configurations of the MoS₂ monolayer on NWs. Through confocal Raman and photoluminescence mapping, we show variations in the properties of the monolayer due to nanowires. We show how the vibrational properties are mainly affected by strain and charge transfer due to the nanowires. A blueshift in the luminescence attributing to an enhanced dielectric screening due to GaAs nanowires is observed. We show how III-V nanowires can be used to engineer the properties and enhance light extraction from monolayer 2-D materials.

Abstract

Keywords

heterostructures, nanowires, nanostructures, quantum dots, 2-D materials, transition-metal dichalcogenides, molecular beam epitaxy, Raman spectroscopy, photoluminescence, transmission electron microscopy

Résumé

Les dispositifs solid-state modernes ont été rendus possibles grâce aux hétérostructures de matériaux semi-conducteurs. Les hétérostructures offrent la possibilité de fabriquer des éléments comme des boîtes ou puits quantiques, pouvant confiner les porteurs de charge dans trois ou deux directions. Les boîtes quantiques (QDs) peuvent être utilisées comme sources de photons uniques, et sont ainsi d'excellents outils dans la photonique quantique et le traitement de l'information. Dans cette thèse, nous explorons des hétérostructures formées par des nanofils et matériaux 2-D pour la fabrication de boîtes quantiques.

Dans la première partie, nous montrons comment la fabrication de nanostructures à facettes auto déterminées peut être utilisée pour faire croître des QDs axiaux et radiaux dans des hétérostructures de nanofils à grande différence de paramètre de maille. Nous avons étudié la croissance par gouttes de Ga de réseaux d'hétérostructures de nanofils InAs/GaAs sur substrat de Si. Nous avons également montré comment la morphologie de la pointe du nanofil influence la formation de clusters axiaux d'In(Ga)As. L'apparition d'amas riches en In sur les nanofils est révélée par microscopie électronique. Nous montrons également comment la formation d'amas d'In(Ga)As sur les parois latérales des nanofils est induite par la convexité des facettes 11-2. Des cartes hyperspectrales de cathodoluminescence et photoluminescence à proximité de la pointe du NW ont mis en évidence la présence de centres d'émission optiquement actifs le long des parois latérales du NW.

La deuxième partie est consacrée aux hétérostructures utilisant des dichalcogénures de métaux de transition 2-D monocouches. Tout d'abord, nous étudions l'hétérojonction entre du MoS₂ monocouche et or. Nous fournissons une explication détaillée des origines microscopiques de la séparation des modes Raman dans le MoS₂ monocouche exfolié sur de l'or. Nous montrons que le fractionnement des modes Raman est une convolution de deux effets : les perturbations structurelles dans le MoS₂ dues à l'interaction Au-S et la rupture des règles de symétrie par les plasmons métalliques. Nous confirmons l'hypothèse en comparant ces résultats avec des expériences analogues mais en remplaçant l'Au par de l'Al, et montrons une absence du dédoublement de pic.

Dans la dernière partie, nous combinons avec succès une monocouche de MoS₂ avec un réseau de nanofils de GaAs, ce qui constitue une première étape vers l'intégration de matériaux 2-D monocouches avec des NW III-V. Nous montrons qu'il existe trois types d'interaction entre les deux matériaux. Grâce à une étude structurale détaillée, nous montrons trois configurations différentes de la monocouche de MoS₂ sur les nanofils. Grâce à la cartographie

Résumé

confocale Raman et à la photoluminescence, nous montrons les variations des propriétés de la monocouche dues aux nanofils. Nous montrons comment les propriétés vibratoires sont principalement affectées par la déformation et le transfert de charge dus aux nanofils. Nous observons un décalage vers le bleu de la luminescence dû à un meilleur blindage diélectrique grâce aux nanofils de GaAs. Nous montrons comment les nanofils III-V peuvent être utilisés pour modifier les propriétés et améliorer l'extraction de la lumière des matériaux 2-D monocouches.

Mots-clés :

hétérostructures, nanofils, nanostructures, boîtes quantiques, matériaux 2-D, dichalcogénures de métaux de transition, épitaxie par faisceau moléculaire, spectroscopie Raman, photoluminescence, microscopie électronique à transmission.

Contents

| | |
|--|-----------|
| Acknowledgements | i |
| Abstract (English/Français) | v |
| List of Figures | xi |
| 1 Introduction | 1 |
| 1.1 Objectives | 3 |
| 1.2 Thesis outline | 3 |
| 2 Motivation and Context | 5 |
| 2.1 Nanowire-based axial quantum dots | 5 |
| 2.1.1 Quantum dots | 5 |
| 2.1.2 Nanowires | 8 |
| 2.1.3 Axial heterostructures | 10 |
| 2.1.4 Growth challenges | 12 |
| 2.2 Combination of 2-D materials with nanostructures | 14 |
| 2.2.1 Introduction to 2-D transition-metal dichalcogenides | 14 |
| 2.2.2 Strain in 2-D materials | 18 |
| 2.2.3 Strain at the nanoscale: Quantum emitters | 19 |
| 2.2.4 Integration with III-V nanostructures | 21 |
| 3 Methods | 23 |
| 3.1 Growth and Fabrication | 23 |
| 3.1.1 Molecular Beam Epitaxy | 23 |
| 3.1.2 Exfoliation and transfer of 2-D materials | 26 |
| 3.2 Characterization | 29 |
| 3.2.1 Electron Microscopy | 29 |
| 3.2.2 Optical spectroscopy | 34 |
| 4 Results and Discussion | 39 |
| 4.1 Facet-driven formation of axial and radial In(Ga)As clusters in GaAs nanowires | 39 |
| 4.1.1 Abstract | 41 |
| 4.1.2 Introduction | 41 |
| 4.1.3 Experimental Details | 42 |

Contents

| | | |
|-------|--|------------|
| 4.1.4 | Results and Discussion | 43 |
| 4.1.5 | Conclusion | 49 |
| 4.2 | On the origin of Raman peak splitting in monolayer 2-D materials-metal inter- faces: MoS ₂ /Au | 51 |
| 4.2.1 | Abstract | 52 |
| 4.2.2 | Introduction | 53 |
| 4.2.3 | Experimental Results | 54 |
| 4.2.4 | Discussion | 56 |
| 4.2.5 | Conclusion | 65 |
| 4.3 | Spatial modulation of vibrational and luminescence properties of monolayer MoS ₂ using a GaAs nanowire array | 68 |
| 4.3.1 | Abstract | 68 |
| 4.3.2 | Introduction | 68 |
| 4.3.3 | Results and Discussion | 69 |
| 4.3.4 | Conclusion | 78 |
| 5 | Conclusions and Outlook | 81 |
| A | Supplementary: Facet-driven formation of axial and radial In(Ga)As clusters in GaAs nanowires | 85 |
| B | Supplementary: On the origin of Raman peak splitting in monolayer 2D materials- metal interfaces: MoS₂Au | 87 |
| C | Supplementary: Spatial modulation of vibrational and luminescence properties of monolayer MoS₂ using a GaAs nanowire array | 95 |
| D | InAs growth on GaAs nanoneedles | 99 |
| | Bibliography | 101 |
| | Curriculum Vitae | 125 |

List of Figures

| | | |
|-----|--|----|
| 1.1 | (a) Epitaxial In(Ga)As quantum dot embedded within a GaAs matrix. Reprinted by permission from Springer: Nature Nanotechnology, Senellart et. al. [1] ©2017. (b) Single photon emitter hosted in a strained monolayer 2-D material (WSe ₂). Adapted from Pardo et. al. [2] licensed under CC BY 4.0. | 2 |
| 2.1 | InAs QD formation on a GaAs substrate as a result of strain relaxation, based on Stranski-Krastanov growth mechanism. | 6 |
| 2.2 | Excitonic state configuration and the corresponding spin-state configurations in a QD for (a) exciton, (b) negative trion, (c) positive trion and (d) biexciton. σ . . | 7 |
| 2.3 | (a) Planar QDs showing the limited collection angle and losses due to total internal reflection at the interface. (b) QD in NW structure, where the extraction efficiency is enhanced by coupling the emission to the fundamental NW waveguide mode. | 8 |
| 2.4 | (a) Self-catalyzed VLS growth; Selective Area Growth and (b) Patterned VLS growth of nanowires | 11 |
| 2.5 | (a) Zincblende (along [111] direction) and (b) Wurtzite (along [0001] direction) structures showing the ABCABC and ABAB stacking sequences respectively. Reprinted from [3], with the permission of AIP Publishing. and (c) Reprinted (adapted) with permission from [4]. ©2020 American Chemical Society. | 11 |
| 2.6 | (a) Kinking and (b) interface grading during the growth of axial NW heterostructures. | 12 |
| 2.7 | Top and side view of lattices in different types (metallic, semiconducting and insulating) of monolayer two-dimensional van der Waals materials. | 14 |
| 2.8 | (a) Lattice structure of monolayer MoS ₂ forming a trigonal prism. (b) Top view of monolayer MoS ₂ lattice with the unit cell highlighted. (c) The first Brillouin zone in a ML MoS ₂ indicating the high symmetry points (K and Γ); band structure around the K and K' points of the Brillouin zone showing the spin-orbit split valence bands. The inset on the right shows the A and B excitonic transitions between the conduction band minimum and the spin-orbit split valence bands. | 15 |

List of Figures

| | | |
|------|--|----|
| 2.9 | (a) Band structure showing the evolution of bandgap with number of layers in MoS ₂ . The bandgap changes from indirect to direct for ML MoS ₂ . Adapted with permission from [5]. ©2010 American Chemical Society. (b) PL spectra from multilayer and monolayer WSe ₂ . The PL intensity increases multifold for ML due to a transition of bandgap from indirect to direct. | 16 |
| 2.10 | (a) Raman spectrum of monolayer MoS ₂ indicating the dominant in-plane (E_{2g}^1) and out-of-plane (A_{1g}) vibrational modes. (b) Evolution of Raman peak positions and their frequency difference as a function of the number of layers. Appropriate credit for the requested material should be given as follows: Adapted with permission from [6]. ©2010 American Chemical Society. | 17 |
| 2.11 | Different techniques to apply strain in 2-D materials. (a) Homogeneous uniaxial strain using substrate bending [7]. (b) Homogeneous uniaxial strain using substrate elongation [8]. (c) Homogeneous biaxial strain using a piezoelectric substrate [9]. | 18 |
| 2.12 | Schematic illustration depicting a monolayer TMD conforming to a nanopillar substrate. | 20 |
| 2.13 | SEM images of (a) a vertical nanowire array and (b) a horizontal nanowire cross. | 21 |
| 2.14 | (a). Types of band alignment in semiconductors. (b) Types of heterostructures formed between monolayer TMDs and various III-V semiconductors [10] | 22 |
| 3.1 | Schematic illustration of the growth chamber in an MBE system | 24 |
| 3.2 | (a) An effusion cell. (b) Arsenic valved cracker cell | 25 |
| 3.3 | Scotch tape exfoliation process. The inset shows an optical image of MoS ₂ flakes exfoliated onto an SiO ₂ /Si substrate | 27 |
| 3.4 | A manual transfer station used for flake transfer. | 27 |
| 3.5 | Illustration of the polymer transfer method showing the side view, top view and optical image taken at each step during the transfer process. | 28 |
| 3.6 | Schematic showing different signals resulting from the interaction of a high energy electron beam with a sample. | 29 |
| 3.7 | Ray diagram illustrating the path of electrons when the TEM is operated in imaging vs. diffraction mode. | 30 |
| 3.8 | Electronic transitions generating X-rays as a result of ejection of an inner shell electron. | 32 |
| 3.9 | Schematic of the CL setup. | 33 |
| 3.10 | (a) Vibrational energy levels involved in Raman scattering. (b) Feynman diagram of the one-photon (Stokes) Raman scattering. | 34 |
| 3.11 | A schematic of the optical setup configured for both Raman and photoluminescence measurements. A flip mirror is used to divert the signal towards either the triple Raman system or the PL detection system. LL: laser line; ND: Neutral density; BS: Beamsplitter; HPF: Highpass filter. | 35 |

| | |
|--|----|
| 3.12 Radiative recombination mechanisms in PL (a) band-to-band recombination, (b) free-to-bound transition, (c) free exciton recombination, (d) bound exciton recombination and (e) donor-acceptor pair transition. VB: valence band, CB: conduction band. | 37 |
| 4.1 Understanding the preferential accumulation of InAs clusters on GaAs NWs. . . | 40 |
| 4.2 (a) A TEM image showing overview of a GaAs NW core viewed along the $\langle 1-10 \rangle$ zone axis (scale bar: $1\mu\text{m}$). Higher magnification images of (b) the bottom, (c) intermediate and (d) top sections of the NW as indicated in (a). The insets in (b) and (d) show the selected-area electron diffraction (SAED) pattern taken from the encircled regions (scale bars: 100 nm). | 43 |
| 4.3 SEM and TEM image showing morphology of the nanowire sample with droplet consumption at 630°C . (a) An overview of the NW array with 55 nm nanohole diameter and $2\mu\text{m}$ pitch (inter-wire distance) (scale bar: $1\mu\text{m}$). (b)-(e) Magnified images of the resultant NW tip after the droplet consumption step (scale bars: 50 nm). (f)-(h) HR-TEM image of the NW tip taken along $\langle 1-10 \rangle$ zone axis. Insets in (f) and (h) show SAED patterns taken from the respective sections of the NW. | 44 |
| 4.4 HAADF-STEM image of the GaAs NW tip after 5 s of InAs deposition under a V/III ratio of 45 at 630°C . (a) HAADF image of the (a) upper (wurtzite) and (b) lower (zincblende) sections of the NW. (c) A magnified image of the NW tip and (d) and (e) simultaneous EDX elemental distributions of Ga and In, respectively. (f) and (g) HAADF-STEM images of two selected sections from the NW super imposed with the EDX map of In. | 45 |
| 4.5 (a) and (b) SEM images of a NW sample after InAs deposition at low temperature (440°C) for 5 mins. (c) Illustration of the proposed material transport mechanisms. The red arrow indicates the adatom diffusion driven by strain relaxation. (d) HAADF-STEM image of the tip of a NW taken from the sample after GaAs shell capping. | 47 |
| 4.6 Spatially-averaged CL spectra of two representative NWs from the sample after shell capping. The spectra correspond to the emission averaged over the region close to the NW tips. The left and right insets indicate energy-filtered CL emission maps and CL-SEM images of the NWs respectively. The inset on the top right in (b) corresponds to a HAADF image of the region indicated by the green box. . . | 48 |
| 4.7 Micro-PL spectra acquired at 4 K from a NW lying horizontally on the as-grown substrate. The spectra are acquired at four different illumination positions on the NW as shown in the inset. The sharp peaks are a clear indication of quantized energy levels in the In(Ga)As clusters on the NW sidewalls. | 49 |
| 4.8 Raman setup configuration. Schematic illustration (left) of the configuration used for Raman spectroscopy in back-scattering mode showing a monolayer of MoS_2 on gold nanoparticles. The inset on the right shows the chemical interaction between S atoms of MoS_2 and Au responsible for the plasmon-phonon interaction. | 54 |

- 4.9 **Characterization of MoS₂ monolayers on Au.** Optical micrographs of ML MoS₂ on (a) 285 nm SiO₂/Si substrate (reference sample) and (b)-(d) on 2, 4 and 7 nm gold deposited on the identical oxidized silicon substrate. Scale bars: 5 μ m (e) Raman and (f) photoluminescence (PL) spectra from the MoS₂ reference, and the MoS₂ on 2, 4 and 7 nm gold respectively. The intensity of the Raman spectra has been normalized to the E_{2g} peak. The dashed curves in (f) show the PL spectra from bare gold substrates. 55
- 4.10 **Peak splitting: literature vs. current work.** Comparison of peak splitting for A_{1g} and E_{2g} modes caused by the interaction of MoS₂ monolayers with Au nanoparticles from various studies and current work. The peak splitting for both the Raman modes remains nearly constant for gold thicknesses up to 200 nm [11–15]. 57
- 4.11 **Raman peak shift and splitting.** A_{1g} and E_{2g} peak shift and splitting predicted and observed as a function of (a) strain (uniaxial [7] and biaxial [16]) and (b) electron density [17], [18]. 58
- 4.12 **Phonon dispersions of MoS₂ monolayers.** Phonon dispersions of the in-plane (LO₂) and out-of-plane (ZO₂) phonons in monolayer MoS₂ obtained from ref. [19], and corresponding to E_{2g} and A_{1g} modes at the Γ -point, respectively. The lines show the positions of A_{1g} and A_{1g}' peaks (red); and E_{2g} and E_{2g}' peak (blue), observed from Raman spectra of MoS₂ on gold thin films in this work. The red and blue rectangles indicate the positions in the Brillouin zone from where the A_{1g}' and E_{2g}' peaks probably originate, which is around the K-point. 62
- 4.13 **Au-sandwiched MoS₂ structure and MoS₂ on Al.** (a) Raman and (b) PL spectra before and after 1nm Au deposition on top of monolayer MoS₂ on a 2 nm Au. Inset in (a) shows an optical image of the MoS₂ flake (Scale bar: 10 μ m). The excitonic peaks in the sandwiched structure are fully quenched due to the charge transfer between Au nanoparticles on both sides of MoS₂. (c) Raman and (d) PL spectra from reference and monolayer MoS₂ on 2 nm Al deposited on 285 nm SiO₂/Si. The PL intensity from reference sample is divided by 2.5 for better comparison. 63
- 4.14 Schematic and corresponding SEM image of a GaAs NW array (a) after growth, (b) after Ga droplet removal and (c) after MoS₂ flake stamping. 70
- 4.15 (a) Bright-field optical image of the MoS₂ flake after transfer to GaAs NW array. (b) Magnified optical image from the bottom left corner of the NW array as indicated in (a). The insets show magnified views of NWs with three different types of optical contrast labeled as type-I, II and III. (c) A 3-D AFM image from the area denoted by yellow box in (b). The dotted rectangles denote the three different configurations of the flake on NWs. 3-D AFM and SEM images, respectively, of (d)-(e) type-I and (f)-(g) type-II configurations as indicated by red and blue dotted rectangles in (c). 71

| | | |
|------|---|----|
| 4.16 | (a) Optical image of region of the flake on NWs mapped in Raman measurements. (b) Raman spectra corresponding to the points indicated in the optical image in (a). The spectra are grouped according to the flake configuration labeled as “folded” (points 3, 4 and 7), “tent-like” (points 11, 12, 13 and 14), “pierced” (points 1, 5, 9) and wrap-around (points 2, 6, 8 and 10). “ref” indicates a reference point on the ML outside the array. (c) and (d) show the Raman maps representing E_{2g}^1 and A_{1g} peak positions acquired from the area depicted in the optical image. The black dashed lines in (a), (c) and (d) indicate edges of the NW array. | 73 |
| 4.17 | (a) An optical image of the region mapped in the PL measurements. (b) and (c) show the PL energy and intensity maps, respectively, corresponding to the area shown in (a). The dashed black lines indicate edges of the NW array. (d) PL spectra extracted from the points indicated in (a) and (b), corresponding to the points used in the Raman measurements except the reference. A new reference point is taken for PL spectral comparison, denoted as “ref (PL).” (e) An intensity linescan across the cross-section indicated by a dashed yellow line in (c). | 76 |
| A.1 | HAADF-STEM images from tip of NWs in samples 2 and 3 as indicted in table A.1 | 86 |
| B.1 | Illustration of sample preparation methods. (a) exfoliation of MoS_2 on SiO_2/Si and Au substrates using the scotch tape method. (b) Polymer transfer method used for transfer of exfoliated MoS_2 flake on Al deposited on SiO_2/Si substrate. | 87 |
| B.2 | Determination of monolayer MoS_2 on gold. (a) Optical micrograph of an MoS_2 flake (b) Green channel image of the MoS_2 flake obtained by splitting the RGB channels of image in (a) using analysis software ImageJ. (c) Optical contrast linescan profile, as indicated in (b) used in determination of a monolayer MoS_2 on Au: $(GV_{\text{substrate}} - GV_{\text{flake}}) / GV_{\text{substrate}}$, where $GV = \text{Gray value}$. In case of monolayers, the optical contrast difference was found to be $\sim 15\%$. (d) AFM image and (e) linescan profile of the MoS_2 flake shown in (a). A thickness of 0.65 nm confirms the thickness to be a monolayer. | 88 |
| B.3 | (a), (b) and (c) SEM and (d), (e) and (f) AFM images for (a) 2 nm, (b) 4 nm and (c) 7 nm Au, respectively. The roughness of the Au substrates was obtained from the AFM image analysis and varies between 0.2-0.25 nm. The grain sizes obtained from SEM image of the 7nm Au were found to be in the range of 10-15 nm. | 89 |
| B.4 | Optical micrographs (left) and Raman spectra (right) acquired from different regions of MoS_2 exfoliated on 2nm Au. (a) Raman spectra acquired from a thicker MoS_2 flake (MS01), monolayer MoS_2 flake (MS02) and Au substrate (MS03). The Raman peak splitting is observed only in case of monolayer MoS_2 . (b) Raman spectra taken from two different MoS_2 monolayers (MS01 and MS03) and Au substrate (MS02). Both the monolayers exhibit peak splitting in the Raman spectra. | 90 |

List of Figures

| | | |
|------|---|----|
| B.5 | Deformation of MoS₂ monolayer on nanocones vs Au. (a) MoS ₂ monolayers on SiO ₂ nanocones from ref [20]. (b) MoS ₂ monolayers on Au substrates in this work. (c) Deformation of MoS ₂ monolayers on top of SiO ₂ nanocones and Au, calculated from TEM and AFM measurements, respectively. The much higher aspect ratio in the case of nanocones (75) when compared to Au substrate (4) shows that the mechanical deformation induced by Au can be considered negligible. (d) Comparison of Raman spectra of MoS ₂ monolayers on SiO ₂ nanocones (obtained from reference [20]) and Au (this work). Shift in Raman peaks in case of nanocones is smaller than in the case of Au, clearly showing the origin of peak splitting is not induced by the mechanical strain due to MoS ₂ deformation. | 91 |
| B.6 | (a)-(b) Raman peak positions and (c) peak splitting of the E _{2g} and A _{1g} Raman modes in monolayer MoS ₂ on 2 nm Au without and with 1 nm Au deposited on top. | 92 |
| B.7 | Polarization-resolved Raman spectra for monolayer MoS ₂ reference on SiO ₂ /Si. | 92 |
| B.8 | Polarization-resolved Raman spectra of monolayer MoS ₂ on 2 nm Au. | 93 |
| B.9 | Excitation wavelength-dependent Raman spectra for MoS ₂ on (a) 2 nm, (b) 4 nm and (c) 7 nm Au respectively, using 488 nm and 532 nm excitation laser sources. The second-order Raman bands are observed around 450 cm ⁻¹ [21]. However, the relative intensities compared to the first-order Raman modes is low to comment on the behavior of these modes. | 93 |
| B.10 | Raman linescans along the ML MoS ₂ on (a) 2 nm, (b) 4 nm and (c) 7 nm Au respectively, using 532 nm excitation. The spectra show presence of both the main and split Raman peaks in all cases where MoS ₂ ML is on top of Au. | 94 |
| C.1 | (a) Optical image of a representative MoS ₂ flake exfoliated on a PDMS film. The monolayer can be identified from the optical contrast. (b) Schematic showing the laser spot location for Raman and PL point measurements. (c) and (d) Room-temperature Raman and PL spectra measured from the flake on array. The monolayer thickness is also confirmed from the frequency difference between the E ₁ ^{2g} and A _{1g} modes (19 cm ⁻¹) and the A- and B-exciton energies around 1.91 and 2.04 eV, respectively. | 95 |
| C.2 | (a) AFM image and (b) linescan profiles from type-III (tent-like) NWs (c) SEM image of a tent-like NW. | 96 |
| C.3 | Identification of the three different types of configurations the flake adopts on top of NWs from the optical and SEM images. | 96 |
| C.4 | SEM image of a folded region of the flake in the vicinity of point-3. | 96 |
| C.5 | Photoluminescence spectra from a monolayer WSe ₂ flake on SiO ₂ , planar GaAs and GaAs NW substrates. The spectra on GaAs substrates show a blueshift in the PL emission peak in comparison to the ML on SiO ₂ substrate. | 97 |
| C.6 | Results of Lorentzian peak fitting to the PL spectra from monolayer MoS ₂ on (a) SiO ₂ and (b) GaAs. | 97 |

| | | |
|-----|--|----|
| D.1 | STEM-EDX of two NN structures with InAs clusters on top. (a),(e) Overview HAADF image of two GaAs NNs: (b),(f) Magnified HAADF image of the tip of the NNs; (c),(g) STEM-EDX image of the tips shown in (b) and (f) showing the In and Ga composition of the NNs and (d),(h) Linescans along the direction indicated in (c) and (g), respectively. | 99 |
|-----|--|----|

1 Introduction

Electronic devices such as personal computers, smartphones, digital cameras and integrated circuits have become a central part of our daily lives. These devices are based on semiconductor technology, which utilizes silicon due to its abundance in nature, high mechanical strength and ease of doping. Extensive research and development on silicon technology over the past few decades has led to mature and high-volume manufacturing processes for electronics.

Photonics, on the other hand, is the technology that deals with the generation, guiding, manipulation and detection of light. Over the past few decades, photonics has led to the development of many breakthrough technologies including optical communications, lighting, health care and data security. The applications of silicon in photonics are limited owing to its indirect bandgap. Compound semiconductors, on the other hand, are often characterized by a direct bandgap which makes them efficient for light-matter interaction in comparison to silicon. Compound semiconductors can also be combined together to form alloys. Tuning the alloy composition allows control over its optical and electronic properties.

Most photonic applications are based on III-V compound semiconductors such as lasers, light-emitting diodes and photodetectors. These devices have been made possible by the ability to combine semiconductors into heterostructures. Heterostructures consist of two or more semiconductor layers stacked together. They provide additional degrees of freedom to vary the material properties spatially within a device such as bandgap, carrier effective mass, mobility and refractive index [22]. When a heterostructure consists of a lower bandgap semiconductor as a middle layer sandwiched between a higher bandgap material, charge carriers can be confined. When the thickness is on the order of few nanometers, the electronic energy levels are strongly affected due to confinement and change in character compared to bulk structures. The electrons are confined in the direction perpendicular to the layers. By reducing the size in all three dimensions, a quantum dot (QD) can be formed with fully discrete energy levels.

QD-based heterostructures are usually grown by epitaxial methods such as molecular beam epitaxy (MBE). Epitaxial QDs are embedded within a matrix material (figure 1.1 (a)) and

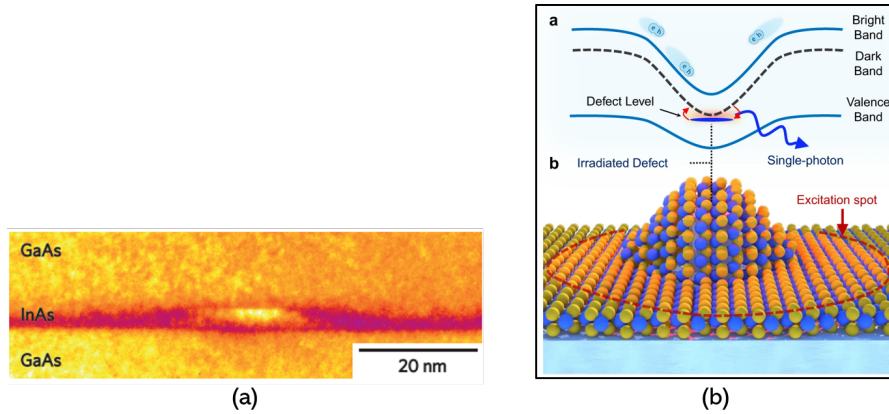


Figure 1.1 – (a) Epitaxial In(Ga)As quantum dot embedded within a GaAs matrix. Reprinted by permission from Springer: Nature Nanotechnology, Senellart et. al. [1] ©2017. (b) Single photon emitter hosted in a strained monolayer 2-D material (WSe₂). Adapted from Parto et. al. [2] licensed under CC BY 4.0.

offer bright, pure and optically stable single photon emission. A wide range of material combinations allow the formation of III-V QDs such as III-arsenide and phosphides for near infrared emission and III-nitrides for emission in the visible and UV spectral range. InAs/GaAs QDs, in particular, have demonstrated the highest single photon emitter performance till date [23]. Such QDs are normally grown on planar substrates and suffer from poor light extraction efficiency. Significant improvement in the extraction efficiency can be obtained by embedding the QDs in photonic waveguiding-like structures such as nanowires [24–26]. However, most QD-based single photon emitters (SPEs) exhibit spatial and spectral non-uniformities, i.e each QD size and emission energy is not identical. Optimization of growth methods for formation of homogeneous QDs is needed to obtain large scale arrays of identical single photon emitters. Nanowire (NW) QDs (NWQDs) offer an attractive choice to achieve this. NWs have enabled integration of III-V compound semiconductors with Si substrates, even in the form of large-scale arrays. By embedding a QD on the NW axis, the emission can be out-coupled to external optics efficiently and the coupling of QD emission to the NW waveguide modes enhances their brightness [27].

In recent years, two-dimensional (2-D) materials have been shown to host single photon emitters. These are most commonly attributed to atomic defects present in these materials that can localize excitons, as shown in figure 1.1 (b). For example, defect-based SPEs have been observed in MoS₂ [28] and WSe₂ [29–32] operating at cryogenic temperatures, whereas SPEs in hexagonal BN have shown room temperature operation [33]. The brightness and purity of such SPEs has been on par with epitaxial semiconductor QD-based SPEs. SPEs in 2-D materials can also be fabricated deterministically by inducing defects. He⁺-ion irradiation [28] in MoS₂ or integration of WSe₂ with nanopillars [34, 35] are two such examples. However, spectral diffusion and instability due to charge traps remains an issue to be resolved. Integration with III-V materials is one approach that can improve stability of SPEs in 2-D materials.

One inherent advantage of suspended atomically thin 2-D materials is the naturally efficient light extraction. [36]. Well-developed transfer processes also enable integration with different substrates [37]. However, the current bottleneck for the application of 2-D SPEs is the low optical absorption (few percent) in these materials when transferred onto a substrate [38]. This, in turn, severely limits the photon extraction efficiency from SPEs in monolayer 2-D materials. One possible solution is to couple emitters in 2-D materials with photonic structures such as nanowires. This can provide four-fold enhancement in the extraction efficiency [39]. Therefore, combining 2-D materials with III-V nanowires would be an interesting pathway towards efficient SPEs in 2-D materials.

1.1 Objectives

The objectives of this thesis are divided into two parts:

- **Objective-1:** The first objective is growth of InAs/GaAs nanowire heterostructure arrays on Si substrates using Ga-catalyzed method. Here, the aim is to position an InAs segment on the axis of a GaAs NW and study optical properties. Ideally, we want to obtain single QDs in NWs to act as single photon emitters. By changing the In(Ga)As material composition, we want to control the emission wavelength of the QD segments.
- **Objective-2:** The second objective is combining 2-D semiconducting monolayer transition-metal dichalcogenides (TMDs) with III-V nanowires to modify their optical properties. We want to use nanowires to induce local strain in monolayer TMDs to deterministically generate single photon emitters in the TMD monolayer.

1.2 Thesis outline

The thesis is divided into four chapters.

Chapter-1 serves as a brief introduction to the thesis and places the topic into its broader context.

Chapter-2 provides the essential background on various topics relevant to the thesis. In the first part, quantum dots, nanowires, and nanowire heterostructures are introduced. Then the challenges faced in the growth of axial nanowire quantum dots are explained. In the second part, 2-D materials are introduced with an emphasis on transition-metal dichalcogenides (TMDs). This is followed by a discussion on how strain can be used to create quantum emitters in 2-D materials. The chapter concludes with a discussion on combining 2-D materials with III-V nanostructures.

Chapter-3 introduces basics of the experimental techniques and setups used in this thesis. Firstly, fabrication of samples using molecular beam epitaxy (MBE) and polymer transfer

Introduction

method are described. Secondly, different characterization techniques are described, including transmission/scanning electron microscopy (TEM/SEM), cathodoluminescence (CL), Raman spectroscopy and photoluminescence (PL).

Chapter-4 presents the main experimental results obtained in this work. Section 4.1 reports on the growth, structural characterization and optical spectroscopy of axial and radial In(Ga)As segments in GaAs NWs. Section 4.2 discusses the physical origins behind the Raman peak splitting in MoS₂ on gold. Section 4.3 presents the results on combination of monolayer MoS₂ with a GaAs NW array.

Chapter-5 summarizes the main conclusions of this work and provides an outlook for further developments based on this thesis.

2 Motivation and Context

In this chapter, the motivation and the background essential for this work are provided. The chapter is divided into two parts. The first part is dedicated to quantum dots (QDs) in nanowires (NWs). In the second part, we discuss the integration of 2-D materials with nanostructures with the perspective of also creating organized single photon emitter structures.

2.1 Nanowire-based axial quantum dots

In this section, nanowire-based axial heterostructures are discussed. These structures allow for enhanced emission and efficient coupling of QD emission to external environment. Firstly, the growth and properties of planar QDs are discussed. This is followed by a motivation on why NWQDs structures can be designed as better single photon sources compared to planar QDs. We then look at the properties and growth of NWs. Axial heterostructures in NWs are discussed in detail along with the challenges hindering growth of defect-free axial NWQDs.

2.1.1 Quantum dots

Quantum dots (QDs) are nanostructures that can confine carriers in all three dimensions. Due to a 3-D confinement, the electronic energy levels in a QD are discrete. This results in discrete atom-like emission lines [40]. Due to quantum confinement effect, the properties of these QDs depend on their size and composition. Thus, the optical properties, such as emission wavelength, can be tuned by changing the QD size or material composition [41]. A major interest in QDs stems from their ability to emit single photons on-demand which enables fundamental studies on light-matter interactions [42]. From a technological perspective, QD-based single photon sources have been explored as building blocks for quantum information processing [43]. Many solid-state materials can host QDs [44]. However, semiconductor QDs have an advantage over other solid-state QDs due to a lot of development on their synthesis and integration into devices over the past few decades [45, 46].

Semiconductor QDs can be synthesized either by colloidal synthesis [47–49] or epitaxial

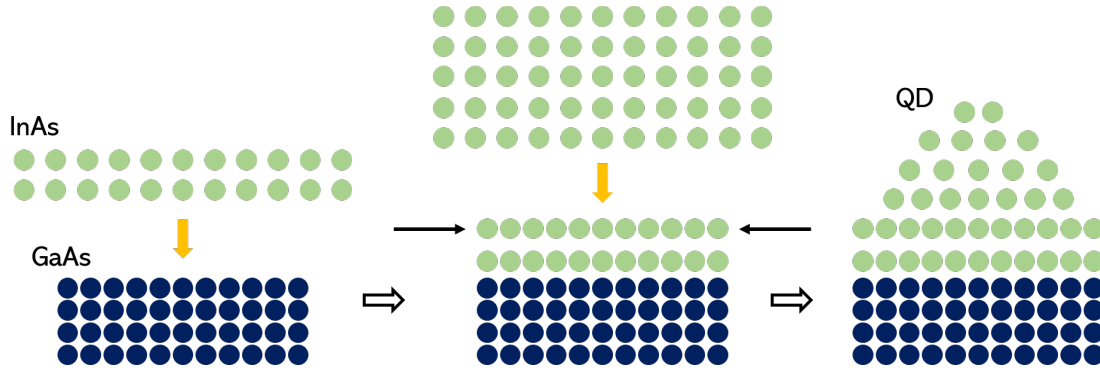


Figure 2.1 – InAs QD formation on a GaAs substrate as a result of strain relaxation, based on Stranski-Krastonov growth mechanism.

growth [50]. III-V semiconductor QDs, in particular, are obtained by embedding a lower bandgap material into a higher bandgap matrix. Due to their high sensitivity to defects and impurities, they are mostly obtained using epitaxial methods such as MBE under ultrahigh vacuum (UHV) conditions. A typical example is, InAs QDs embedded within a GaAs matrix [1] which are grown by the Stranski-Krastonov (S-K) method based on self assembly. The large lattice mismatch (7%) between InAs and GaAs leads to strain at the interface when InAs is deposited on GaAs. Beyond a critical thickness, the strain is relaxed in the form of island formation. These islands have a lens-like shape with widths less than 30 nm and few nm in height. They can confine carriers in the vertical direction and are referred to as QDs. A GaAs capping layer is then deposited to embed the QDs. The growth mechanism of QDs is illustrated in figure 2.1.

We now discuss the optical properties of III-V semiconductor QDs using the particular case of InAs QDs embedded in a GaAs matrix. The valence bands of InAs and GaAs consist of degenerate heavy hole (HH) and light hole (LH) bands along with a downshifted split-off (SO) band due to spin-orbit interactions [51]. The band alignment at the InAs and GaAs interface is type-I. This confines both the electrons and holes in conduction and valence bands, respectively. Due to the confinement, the degeneracy between HH and LH bands is lifted. The degeneracy is further lifted due to strain in InAs/GaAs QDs. Thus, the lowest energy transition occurs between lowest conduction band edge and the HH state. In QDs, a strong Coulomb interaction exists between electrons and holes. Therefore, the transitions in a QD are excitonic.

The valence and conduction bands in QDs consist of discrete energy levels. Under low excitation conditions, the electrons and holes in an excited state in a QD relax to the lowest ground state within each band via phonon-mediated transitions. These then recombine by radiative recombination between the s-shells. A QD is, therefore, approximated as a two-level system. Using optical excitation, a QD can be loaded into four possible excitonic configurations: (a) an electron and a hole (exciton, X), (b) two electrons and one hole (negative trion, X^-), (c) one electron and two holes (positive trion, X^+) and (d) two electrons and two holes (biexciton,

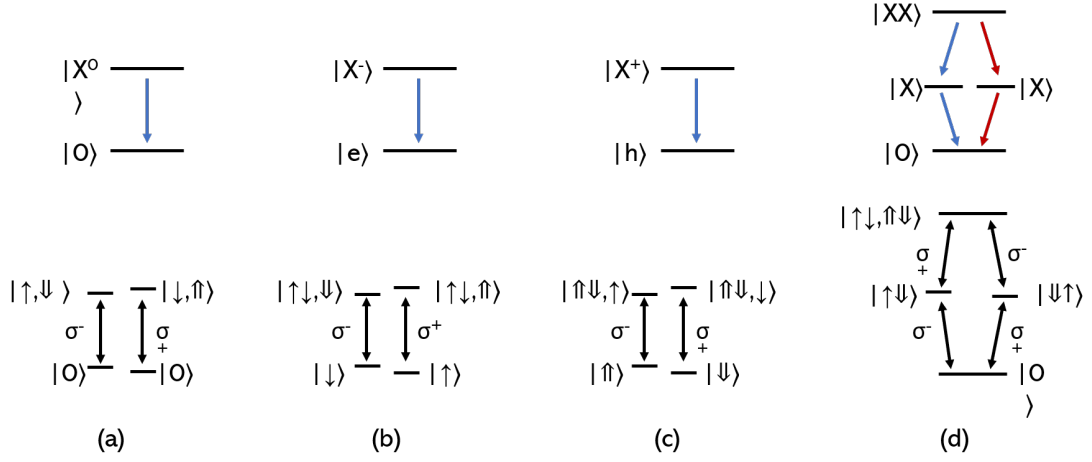


Figure 2.2 – Excitonic state configuration and the corresponding spin-state configurations in a QD for (a) exciton, (b) negative trion, (c) positive trion and (d) biexciton. σ

XX), in the conduction and valence bands respectively. The recombination of an electron and a hole results in emission of a photon. The recombination paths for different excitonic configurations are shown in the top half of figure 2.2 considering only the heavy-hole (HH) state. In the effective mass description ($k.p$ model), the heavy-hole state and electron state are constructed from the $(J, J_z = 3/2, \pm 3/2)$ and $(S, S_z = 1/2, \pm 1/2)$ Bloch states, respectively [52]. The subscript 'z' represents confinement in vertical direction. The total angular momentum quantum number is given as $J = S + L$, where L is the orbital quantum number. The conservation of angular momentum dictates that the orbital angular momentum be quantized ($L = \pm 1$). Therefore, the states indicated in the bottom half of figure 2.2 will result in bright optical transitions. These transitions will result in emission of a photon with either right-handed (σ^+) or left-handed (σ^-) polarization [52].

QDs grown by the S-K mechanism shown above in figure 2.1 form at random locations and their position cannot be easily controlled. Before any characterization and processing, the QDs must be precisely located. This limits their integration into photonic devices. To overcome this limitation, site-controlled QDs have been fabricated using growth in etched holes [53–56] and pre-defined growth templates [57, 58] or V-grooves [59]. This allows for a more deterministic growth of QDs. Despite narrow linewidth, high optical stability and bright single photon emission, semiconductor QDs grown on planar substrates suffer from poor light extraction efficiency due to losses by total internal reflection at the semiconductor-air interface. Due to the high refractive index contrast, light can only escape within a narrow solid angle limiting extraction to the order of a few percent. This is illustrated in 2.3 (a). Numerous efforts were undertaken to improve the light extraction from planar QDs such as embedding them in microcavities [60, 61], microdisks [62] and photonic crystals [63, 64]. It is important to note that the brightness and yield of these sources is limited by the alignment accuracy between the QDs and the photonic structure [42].

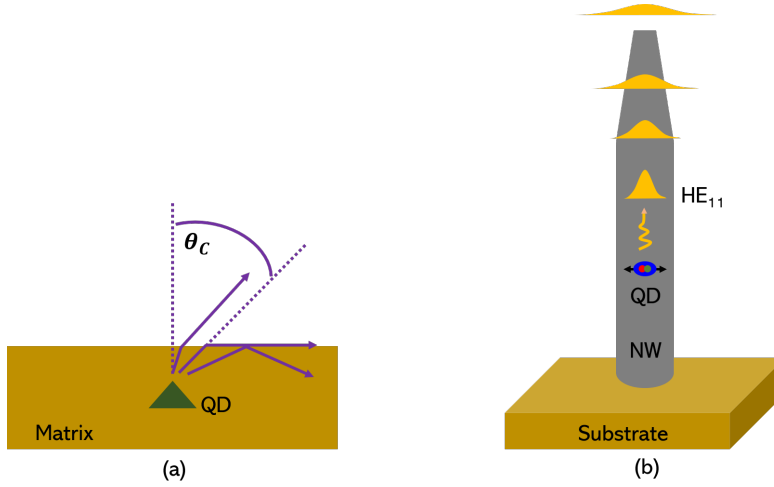


Figure 2.3 – (a) Planar QDs showing the limited collection angle and losses due to total internal reflection at the interface. (b) QD in NW structure, where the extraction efficiency is enhanced by coupling the emission to the fundamental NW waveguide mode.

In NW structures, this is translated in the need of positioning the QD in the center of the cross-section, so that the QD emission couples to the fundamental waveguide mode of NWs (HE_{11}) is possible. Photon emission can then be extracted efficiently through waveguiding in the NWs [27]. Not only can the extraction efficiency be improved, but also the spontaneous emission of the QD can be enhanced to a desired optical mode by suppressing emission into other modes [27]. This is expressed in terms of the β factor as: $\beta = \frac{\Gamma}{\Gamma + \gamma}$, where Γ is the spontaneous emission rate into the desired optical mode and γ is the spontaneous emission rate into all other modes. For QDs in NWs, the β -factor can be above 90% for a wide range of diameters as demonstrated by Friedler *et. al.* [27]. This is obtained by simply positioning the emitter (QD, in this case) on the NW axis which inhibits emission into non-waveguiding (γ) modes unlike microcavities which require emitter-cavity mode coupling. This is illustrated in figure 2.3 (b). The extraction efficiency can be further enhanced by tapering the NW tip. Tapering enables an adiabatic expansion of the fundamental NW mode into a Gaussian far-field profile, thus minimizing the output beam divergence and reflection at the semiconductor-air interface [65].

2.1.2 Nanowires

The initial work on nanowhiskers by Wagner and Ellis [66] in 1964 established the foundations for the bottom-up growth of NWs. Using gold droplets, they showed that it was possible to grow silicon in the form of filamentary crystals. This type of growth is termed Vapor-Liquid-Solid (VLS) growth. The three main steps involved are: (a) deposition of a catalyst droplet; (b) dissolution of precursors from vapor phase into the liquid droplet; (c) supersaturation of the droplet and precipitation of NWs beneath the droplet. This is shown schematically in figure

2.4 (a). The VLS method can be used to grow various semiconductors materials in the form of nanowires, for example, Germanium, GaAs, InAs, GaSb and other III-V semiconductors. This work is based on GaAs nanowires. The focus will, therefore, be mainly on the growth and properties of GaAs nanowires. The method used by Wagner and Ellis involved the use of gold droplets as catalysts. Gold is known to create deep level traps in semiconductors such as GaAs and thus, degrades its electronic properties. A well-established alternative is to use self-catalyzed technique, where the catalyst droplet is a constituent of the NW material itself [67]. In case of GaAs, this would be a Ga droplet. On the substrates generally used for growth (GaAs, for example), the naturally formed oxide consists of pinholes. The Ga droplets form in these locations and define the position of nanowires. Nanowires grown in this way form at random locations on the substrate. This technique is referred to as self-catalyzed growth.

It is also possible to grow NWs in pre-defined positions [68, 69]. This technique has technological importance since it provides a good control over the NW growth and device integration. This can be done by opening an array of holes on a substrate covered with a dielectric mask using e-beam lithography. Providing precursors under suitable growth conditions results in nanowire growth. This technique is referred to as selective area epitaxy/growth (SAE/G). The growth follows Vapor-Solid (VS) mechanism and a catalyst droplet is absent. This is shown schematically in figure 2.4 (b). Another way to grow nanowires in pre-defined positions is patterned VLS method. As shown schematically in figure 2.4 (c), nanoholes can be defined lithographically on the substrate. These act as sites where Ga droplets can be localized and used to grow nanowires [68]. SAE is mainly done using Metal-organic vapor phase epitaxy (MOVPE) and patterned VLS is mainly carried out using a molecular beam epitaxy (MBE) system. The NWs studied in this work are grown by the patterned VLS method in an MBE system. A detailed description of an MBE system and the growth parameters are discussed in section 3.1.1.

Nanowires are one-dimensional filamentary crystals with high length-to-width ratios. The typical length of NWs ranges from a few hundreds of nanometers to several micrometers while the diameter is typically < few hundred nanometers. They can behave as waveguides with high refractive index contrast between the NW material and surrounding environment. This makes light extraction and external coupling efficient [65]. Combining two materials with different lattice constants typically leads to strain in the structure [70]. When this happens in the bulk, the strain is released by the formation of defects such as dislocations. When this happens in case of NWs, due to the small diameter, the strain can be relaxed on the NW sidewalls and the structure is rendered almost defect-free [71]. Thus, nanowires can accommodate much higher lattice mismatch compared to their bulk counterparts. This provides an additional degree of freedom for combining different materials in a defect-free way, such as in axial heterostructures. Axial heterostructures are discussed further in section 2.1.3.

We now discuss the crystal structure of GaAs NWs. In the bulk form, GaAs exhibits a cubic zincblende (ZB) crystal structure. In NWs form, the hexagonal wurtzite (WZ) and other polytypic phases becomes possible [72–75]. As a simplified explanation, stable ZB vertical NW

growth occurs in the $\langle 111 \rangle$ crystal direction. This is closely related to the $\langle 0001 \rangle$ crystal growth direction of the hexagonal WZ phase. The two crystal phases and their stacking sequences are shown in figure 2.5 (a) and (b). The ZB phase follows a stacking sequence ...ABCABC... whereas the WZ phase follows a stacking sequence ...ABAB..., where A, B and C denote one of the three possible positions of the III-V atomic layer pairs aligned in the growth direction. The stacking sequence in the growth of NWs is often interrupted by the insertion of a fault plane. For example, an ...ABC... stacking sequence can change to ...ABC**B**, where B is the fault plane. If a ZB stacking continues on top of this plane, a "rotational twin" is created resulting in a stacking sequence ABC**B**AC, where the preceding **C** plane is called a mirror plane. On the other hand, nucleation of another fault plane on top of ABC**B** will result in formation of a WZ segment. Initially, the stable growth of WZ phase in NWs was attributed to the high surface-to-volume ratio [76]. However, recent studies have shown that the droplet contact angle is the sole parameter that dictates the crystal phase in self-catalyzed NWs [4]. This is shown in figure 2.5 (c). For smaller ($< 100^\circ$) and larger ($> 125^\circ$) contact angles, the phase is ZB, while for intermediate contact angles between these, the WZ phase is observed [4]. Thus, changes in the droplet size, and therefore, the contact angle, can lead to an intermixing of crystal phases during NW growth [77]. The microscopic mechanism behind this can be attributed to different interface energies for WZ and ZB. For nucleation at the vapor-liquid-solid triple phase line (interface at the solid NW-liquid droplet), WZ formation is favored due to a lower interface energy than ZB [73]. This has been shown experimentally at higher droplet supersaturation during the NW growth [73, 75].

2.1.3 Axial heterostructures

In a planar geometry, heterostructures are layered stacks of different semiconductors that can be used to alter their optical and electronic properties. Heterostructures of III-V semiconductors can be grown with a monolayer precision using epitaxial techniques such as MBE and MOVPE. This enables us to change the material composition abruptly and has enabled the growth of artificial lattices, such as superlattices and quantum wells [78, 79]. Superlattices consist of two semiconductors grown alternatively in a periodic manner, one example is GaAs and AlAs distributed Bragg reflectors [80]. Quantum wells, on the other hand, consist of a few layers of a lower bandgap material sandwiched between a higher bandgap material. This leads to a confinement in the vertical direction. Further reducing the size in all three dimensions, QDs can be grown. As discussed in section 2.1.1, planar QDs grown in this way suffer from poor light extraction and QDs in NWs overcome this problem by coupling the QD emission to fundamental mode of NW and enhancing the out-coupling. A QD segment positioned on the NW axis is referred to as an axial heterostructure.

Here, we review the state-of-the-art of axial heterostructures from a growth perspective. Combining materials with a high lattice mismatch in NWs is easier since the strain can be effectively relaxed on the NW sidewalls. Early attempts at defining heterostructures in NWs were promising and aimed at InAs/GaAs [81], InAs/InP [82] and GaAs/GaP [83] systems which find wide

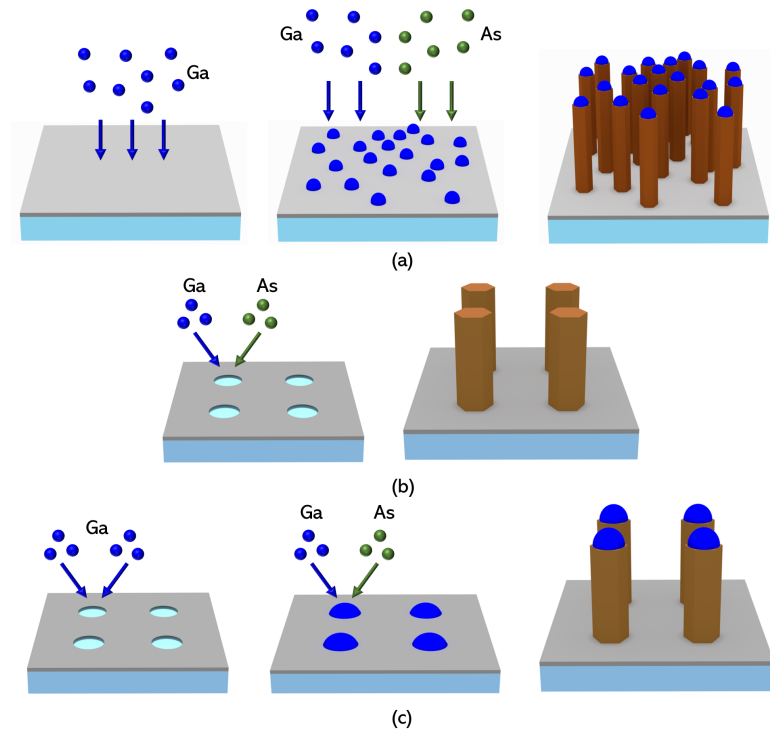


Figure 2.4 – (a) Self-catalyzed VLS growth; Selective Area Growth and (b) Patterned VLS growth of nanowires .

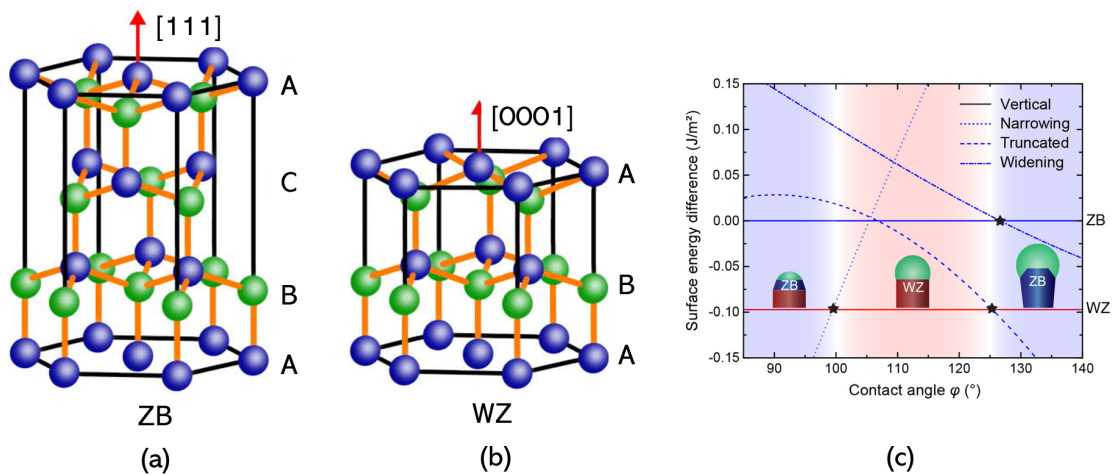


Figure 2.5 – (a) Zincblende (along [111] direction) and (b) Wurtzite (along [0001] direction) structures showing the ABCABC and ABAB stacking sequences respectively. Reprinted from [3], with the permission of AIP Publishing. and (c) Reprinted (adapted) with permission from [4]. ©2020 American Chemical Society.

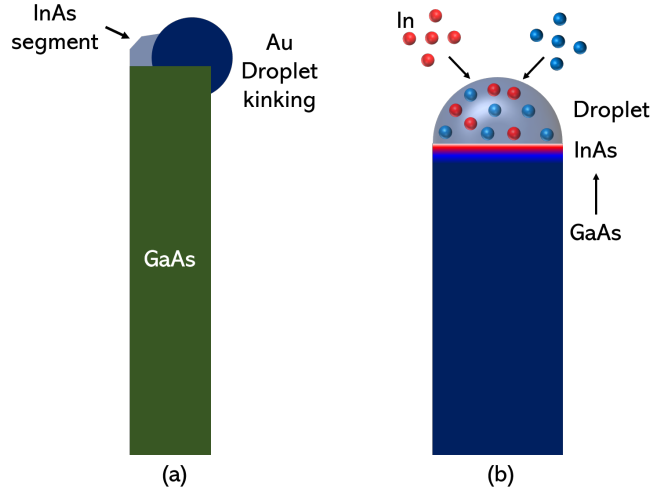


Figure 2.6 – (a) Kinking and (b) interface grading during the growth of axial NW heterostructures.

applications in optoelectronics. Even materials with extreme lattice mismatch, InSb on GaAs, were combined using NW heterostructures [84]. Out of all III-V semiconductor material combinations, InAs/GaAs QD system is of particular interest since the single photon emission purity can be as high as 99% [85]. By changing the composition of the ternary In(Ga)As alloy, the emission wavelength can be continuously tuned in the mid-infrared range. Of particular interest is the ability to tune the emission wavelength to 1.3 and 1.55 μm which is compatible with the low-loss telecom window of optical fibers. In this work, nanowires are grown on Si substrates using patterned VLS growth method with Ga as a catalyst, as shown in figure 2.4. Si substrates offer a cheaper alternative compared to expensive GaAs substrates and patterned VLS method allows controlled growth and positioning of NWQDs.

2.1.4 Growth challenges

An axial QD in NW consists of a thin axial heterostructure, where a small QD segment is embedded within the nanowire material (for example, InAs segment in a GaAs NW). For pure single photon emission, the QD environment should be free of defects and impurities. Also, a grading in the interface between the QD segment and the surrounding matrix will reduce the barrier height and thus, the QD confinement. The interface between the QD material and the barrier is termed as heterointerface. Although group-V material can be easily switched during the growth of NW heterointerfaces [86], the interchange of group-III elements is more challenging. Combining III-V materials, InAs and GaAs in particular, faces two main challenges: (a) kinking, to minimize the surface energy [87] and (b) interface grading, as a result of reservoir effect [88]. These two phenomena are illustrated in figure 2.6 at the nanowire tip and further explained here below..

Kinking refers to an instability in the catalyst droplet during growth which results in a change of growth direction and failure of axial growth. [87]. It is caused by the modification of the wetting of the droplet during the formation of the heterostructure. When using an Au droplet to grow InAs/GaAs NW heterostructure, switching between In and Ga leads to the Au droplet moving to the NW sidewalls. This is explained by the difference in interfacial surface energies for the Au-InAs and Au-GaAs interfaces ($\gamma_{\text{Au-GaAs}} < \gamma_{\text{InAs-GaAs}} + \gamma_{\text{Au-InAs}}$) [87], such that the Au droplet tries to maintain an interface with GaAs. Kinking was avoided to some extent in Au-catalyzed NWs by tuning the growth parameters to obtain WZ InAs segments which grow vertically [89]. Reservoir effect refers to accumulation of one group-III species in the Au droplet due to different solubility. When the group-III element is switched, the previously accumulated material continues to be incorporated for some time into the NW during the growth of a new material segment. This leads to a graded interface. Grading in Au-catalyzed axial NW heterointerfaces was overcome by reducing droplet diameters below 40nm [90] or by switching to the vapor-solid-solid mechanism [91].

In case of Ga-catalyzed VLS growth, kinking can be avoided [92]. For In(Ga)As/GaAs heterostructures, the material can be switched from GaAs to In(Ga)As by adding In to the droplet [93]. Using this method, however, the In concentration of the In(Ga)As alloy is limited to around 5% [94]. Therefore, the presence of Ga droplet limits the maximum In concentration and abruptness of the InAs-GaAs heterointerface. Completely consuming Ga droplet used in the growth of NWs provides a flat NW top facet that can be used to crystallize InAs segments in GaAs NWs [95]. By depositing In droplets and crystallizing into InAs at a reduced growth temperature, Scarpellini *et. al.* [95] reported an interface abruptness of $< 1.5\text{nm}$ at the InAs/GaAs interface. The radial growth is also suppressed due to lower In diffusivity at lower temperatures [96]. GaAs axial growth can then be resumed by re-positioning a Ga droplet at the nanowire tip [97]. Therefore, this method provides a pathway to grow self-catalyzed InAs/GaAs NW heterostructures.

2.2 Combination of 2-D materials with nanostructures

This section provides a brief introduction to 2-D transition-metal dichalcogenides (TMDs). Their crystal structure and optical properties are discussed. This is followed by a discussion on methods to introduce strain in 2-D materials and how strain affects their properties. The method of introducing local strain in monolayer TMDs, which allows for deterministic creation of single photon emitters, is discussed in detail. Lastly, the prospect of integrating monolayer TMDs with III-V nanostructures and its advantages are discussed.

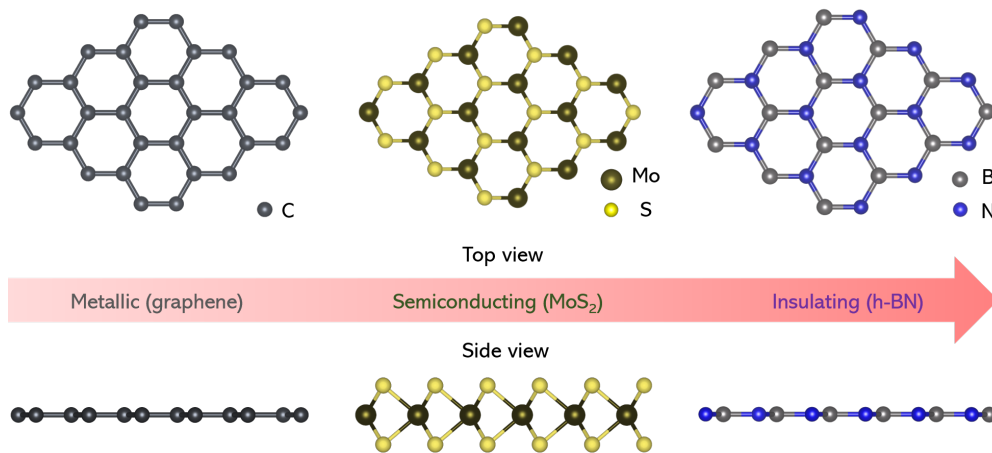


Figure 2.7 – Top and side view of lattices in different types (metallic, semiconducting and insulating) of monolayer two-dimensional van der Waals materials.

2.2.1 Introduction to 2-D transition-metal dichalcogenides

The discovery of graphene [98], a single layer of carbon atoms, opened up a whole new avenue of research into two-dimensional materials. Two-dimensional materials subsequently explored span a whole range of optical and electronic properties from metals to insulators (figure 2.7). Two-dimensional transition-metal dichalcogenides (TMDs) are one such class of materials exhibiting very interesting optical and electronic properties which make them relevant for fundamental studies and device applications. Group-VI TMDs are of special interest since they exhibit semiconducting properties. It is possible to tune their bandgap by varying the number of layers. In the bulk form, these TMDs exhibit an indirect bandgap. A transition of the bandgap from indirect to direct occurs, when their thickness is reduced to a single layer [5].

Semiconducting TMDs are compounds of type MX₂, where M represents a transition metal atom (Molybdenum (Mo) or Tungsten (W)) and X represents a chalcogen atom (Sulfur (S) or Selenium (Se)). Each layer of metal atoms (M) is sandwiched between two layers of chalcogen (X) atoms. Each layer consists of covalently bonded atoms, whereas the layers are held together by weak van der Waals forces. The most widely studied TMD material is MoS₂. In the

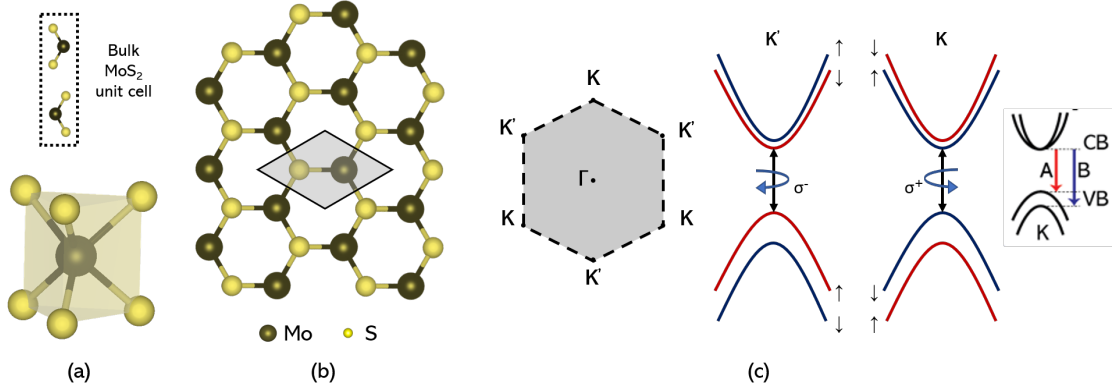


Figure 2.8 – (a) Lattice structure of monolayer MoS₂ forming a trigonal prism. (b) Top view of monolayer MoS₂ lattice with the unit cell highlighted. (c) The first Brillouin zone in a ML MoS₂ indicating the high symmetry points (K and Γ); band structure around the K and K' points of the Brillouin zone showing the spin-orbit split valence bands. The inset on the right shows the A and B excitonic transitions between the conduction band minimum and the spin-orbit split valence bands.

bulk form, it exhibits a 2H hexagonal crystal structure with two trigonal prisms on top of each other (figure 2.8 (a)). In addition, the metastable 1T phase has also been observed with an octahedral crystal structure. However, most exfoliation and growth methods result in the stable 2H phase.

Bulk MoS₂ belongs to the D_{6h}^4 ($P6_3/mmc$) space group with an inversion symmetry. In case of a monolayer, this inversion symmetry is broken. A 3-D and a top view of the monolayer MoS₂ lattice are shown in figure 2.8 (a) and (b), respectively. The highlighted region in (b) indicates a unit cell and the first Brillouin zone with corresponding high symmetry points is shown in figure 2.8 (c). The direct bandgap in monolayer TMDs is located at K and K' points. In graphene, the K and K' valleys at corners of the Brillouin zone are degenerate since all the C atoms are similar. In case of MoS₂, the lattice is made up of sublattices, consisting two different atoms (Mo and S). This lifts the degeneracy between two adjacent corners of the Brillouin zone making them distinguishable as K and K' valleys (figure 2.8 (c)). While there should not be any surface states, point defects and wrinkles often result into deviations from the ideal functional properties [99, 100].

Another interesting feature of monolayer TMDs is the spin- and valley-dependent properties as a consequence of the broken inversion symmetry. The K and K' points at the edges of the Brillouin zone can be represented by a binary pseudospin that behaves like a spin-1/2 system. For example, the electrons in the K valley can be thought of as having a pseudospin-up while the electrons in K' valley can be thought of as having a pseudospin-down. This is schematically shown in figure 2.8 (c). The strong spin-orbit interactions in TMDs lift the spin degeneracy and couple each type of spin (spin-up and spin-down) to one of the valley pseudospins. This

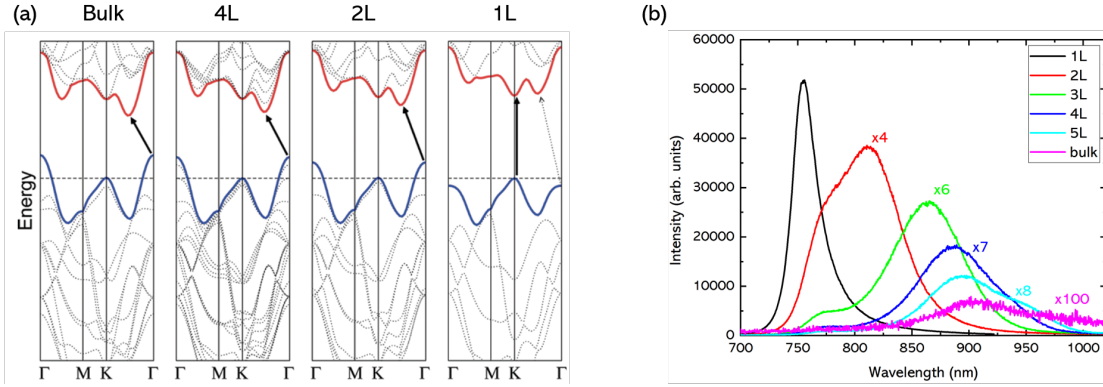


Figure 2.9 – (a) Band structure showing the evolution of bandgap with number of layers in MoS₂. The bandgap changes from indirect to direct for ML MoS₂. Adapted with permission from [5]. ©2010 American Chemical Society. (b) PL spectra from multilayer and monolayer WSe₂. The PL intensity increases multifold for ML due to a transition of bandgap from indirect to direct.

is referred to as spin-valley coupling. These valley pseudospins can be optically addressed with circularly polarized light, the so-called valley-dependent optical selection rule. This feature has significant implications for optically driven valleytronic devices which may find applications in optical information processing.

The nature and value of bandgap in TMDs depends on the number of layers. The bandgap in bulk and few-layer TMDs is indirect and becomes direct as the thickness is reduced down to a monolayer. Taking MoS₂ as an example, figure 2.9 (a) shows the bandstructure of bulk, quadrilayer, bilayer and monolayer MoS₂ calculated using density functional theory (DFT). For bulk and few-layer MoS₂, the maxima of the valence band lies at the Γ point and the minima of the conduction band lies midway between K and Γ point (Q point) of the Brillouin zone. In case of a monolayer, the indirect bandgap increases drastically becoming higher than the transition energy at the K point. This results in a transition from an indirect to a direct bandgap. This can be explained on the basis of difference in the contributions of orbitals to the energy bands. The energy states near Γ and Q point arise from the linear combination of Mo d-orbitals and S p_z orbitals and have a strong layer-dependent coupling. Whereas, the contributions at the K point mainly comes from only the Mo d-orbitals with a minimal interlayer coupling. This is applicable to other TMDs as well. The main effect is an emergence of higher intensity in the photoluminescence spectrum of a monolayer TMD. This is shown by the PL spectra of multilayer and monolayer WSe₂ in 2.9 (b). The PL intensity keeps monotonously increasing as the number of layers is reduced from the bulk and is the highest in case of a monolayer.

The absence of dangling bonds at the surface of monolayer TMDs implies absence of any surface states and provides them with robust optical and electrical properties. In addition, due to the two-dimensional nature, the excitonic binding energies are an order of magnitude higher compared to conventional semiconductors. This makes it easier to observe the excitonic

2.2. Combination of 2-D materials with nanostructures

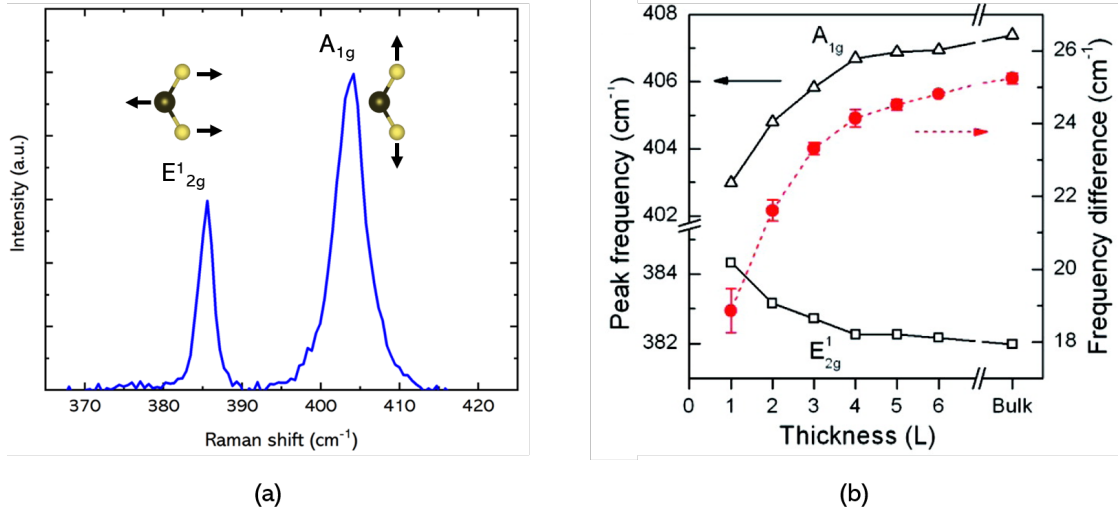


Figure 2.10 – (a) Raman spectrum of monolayer MoS₂ indicating the dominant in-plane (E_{12g}) and out-of-plane (A_{1g}) vibrational modes. (b) Evolution of Raman peak positions and their frequency difference as a function of the number of layers. Appropriate credit for the requested material should be given as follows: Adapted with permission from [6]. ©2010 American Chemical Society.

features even at room temperature. The room temperature PL spectrum of monolayer TMDs is characterized by two dominant excitonic peaks. These arise from transitions between the two spin-orbit split valence band maxima and the conduction band minima, denoted as A- and B-excitons as shown in figure 2.8 (c).

Similar to the optical properties, TMDs exhibit interesting vibrational properties. A bulk MoS₂ the unit cell consists of 6 atoms, resulting in 18 (3 x number of atoms in a unit cell) Brillouin zone center (Γ) phonons. The irreducible representation of zone center phonons is given as [101]:

$$\Gamma \equiv A_{1g} + 2A_{2u} + B_{1u} + 2B_{2g} + E_{1g} + 2E_{1u} + E_{2u} + 2E_{2g}$$

where A_{1g}, E_{1g} and two E_{2g} are the Raman active modes, A_{2u} and E_{1u} are IR active acoustic modes and B_{2g}, B_{1u} and E_{2u} are inactive phonon modes.

The experimental Raman spectrum of MoS₂ is dominated by two intense peaks attributed to the E_{12g} and A_{1g} modes. These vibrational modes can be observed using Raman spectroscopy. Figure 2.10 (a) shows the Raman spectrum of a monolayer of MoS₂, with E_{12g} and A_{1g} peaks. The E_{12g} mode originates from the in-plane vibrations of Mo and S atoms and the A_{1g} mode originates from the out-of-plane vibrations of only S atoms. These Raman modes are also sensitive to the number of layers of MoS₂. Thus, Raman spectrum can be used to reliably identify the number of layers in MoS₂. As the number of layers increases, the E_{12g} mode shifts to lower frequencies while the A_{1g} mode shifts to higher frequencies [6]. This evolution with the number of layers is shown in figure 2.10 (b). In addition to this, the Raman modes of TMDs

are also sensitive to external perturbations such as strain [7] and doping [102].

2.2.2 Strain in 2-D materials

The possibility of tuning optical and electronic properties of semiconductors is an important design element for the development of future technological devices. One possible way of doing this is by applying strain to the semiconductor material. The ultrathin nature of 2-D materials makes them highly sensitive to any external perturbations such as strain and doping. 2-D materials can sustain unusually high amounts of strain due to the absence of dangling bonds or surface defects and high crystallinity [103]. Thus, the fracture point is ultimately determined by the strength of atomic bonds. For example, the fracture strength of an MoS₂ monolayer is $\sim 1/8$ of its Young's modulus [104]. According to Griffith's theory, this reaches the theoretical strength limit ($\sim 1/9$ of Young's modulus) for ideal brittle materials [105]. TMD monolayers can sustain strain values $>10\%$ while Si breaks at a strain of $\sim 1.5\%$ [103]. Therefore, strain engineering provides a wider tunability over the properties of TMDs in a controllable way.

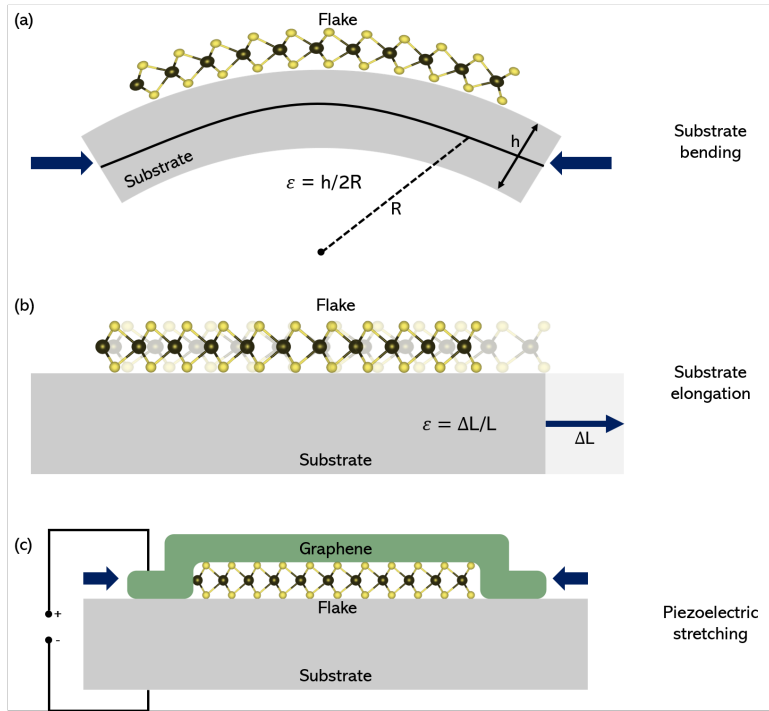


Figure 2.11 – Different techniques to apply strain in 2-D materials. (a) Homogeneous uniaxial strain using substrate bending [7]. (b) Homogeneous uniaxial strain using substrate elongation [8]. (c) Homogeneous biaxial strain using a piezoelectric substrate [9].

Broadly, strain can be applied to 2-D materials in three different ways, classified on the basis of nature of the applied strain [103, 106]: (a) Homogeneous uniaxial strain; (b) Homogeneous

biaxial strain; (c) Inhomogeneous local strain. Figure 2.11 summarizes some of the techniques to apply strain in 2-D materials. The 2-D material are exfoliated, transferred or directly grown on the target substrate. Homogeneous uniaxial strain can be applied either by bending [7] or elongation [8] of a substrate with the 2-D material deposited on top as shown in figures 2.11 (a) and (b), respectively. In case of bending, the strain is given as: $\epsilon = h / 2R$, where, h is the substrate thickness and R is the radius of curvature. Homogeneous biaxial strain can be applied by transferring the 2-D material on a piezoelectric substrate [9]. The application of an electric field causes out-of-plane elongation of the piezoelectric material and an in-plane shrinking. This leads to a biaxial compression in the 2-D material. This is illustrated schematically in figure 2.11 (c). An alternative way to apply biaxial strain is combining the 2-D material with a substrate that has a large thermal expansion mismatch with the 2-D material [107]. Heating the substrate leads to a uniform biaxial strain in the 2-D material. Another interesting way of straining 2-D materials is by applying inhomogeneous local strain. This was first demonstrated by Castellanos-Gomez *et. al.* [108] in 4L MoS₂. This method is central to this work and is discussed in the next section.

The simplicity of various techniques available for straining 2-D materials allows one to choose the most feasible technique for a specific application. However, the maximum amount of strain that can be applied varies in each case [103]. For example, in monolayer MoS₂, maximum values of strain reported till date are about 2.4% for uniaxial [7], 0.2% for biaxial [9, 107] and 2.5% [108] for inhomogeneous local strain. Application of strain to TMDs leads to changes in their optical and electronic properties. This is related to the strain-related modification in the bandstructure of TMDs. For example, the bandgap of monolayer and bilayer TMDs decreases linearly with increasing homogeneous tensile strain [7]. Applying higher amounts of strain further leads to a bandgap transition, either from direct to indirect in monolayer TMDs [7] or indirect to direct in few-layer TMDs [109]. The vibrational properties are also affected based on the nature of applied strain. The in-plane E_{2g} mode is highly sensitive to strain compared to the out-of-plane A_{1g} mode. Application of tensile or compressive strain leads to either softening [7] or stiffening [9] of the E_{2g} mode and shifts the Raman peak to lower or higher frequencies, respectively.

2.2.3 Strain at the nanoscale: Quantum emitters

Monolayer TMDs, such as WSe₂ can host single photon emitters (SPEs) which exhibit sharp QD-like emission peaks [29–32]. Linewidths as narrow as 10 μ eV have been observed from SPEs in monolayer WSe₂ [110]. Table 2.1 summarizes the experimental values of physical parameters for localized emitters observed in W- and Mo-based monolayer TMDs. Although the microscopic origin of these emitters is not accurately known, the most likely attribution is given to defects and localized strain gradients. Recent strain-dependent band profiles obtained from density-functional theory (DFT) calculations have shown a decrease in bandgap with applied strain [111, 112]. Moreover, the effective dielectric function is lowered with the applied strain [112]. The idea is that defects in such materials provide strong localization to excitons

Chapter 2. Motivation and Context

| Material | Lifetime | Linewidth | $g^2(0)$ |
|-------------------|------------------------------------|-----------------------------|------------|
| WSe ₂ | 100 ps [113] 2-225 ns [115] | 10 μ eV [114] | 0.02 [114] |
| WS ₂ | 1.4 ns [116] | \sim 3 meV [34] | 0.31 [116] |
| MoSe ₂ | 0.19 [117] | 150-500 μ eV [118, 119] | 0.29 [117] |
| MoS ₂ | 1.73 μ s [120] <150 ps [28] | 0.5-0.6 meV [28] | 0.23 [120] |

Table 2.1 – Experimental values of emission lifetime, linewidth and $g^2(0)$ for localized emitters in different monolayer TMDs. Table inspired by Chakraborty *et. al.* [121].

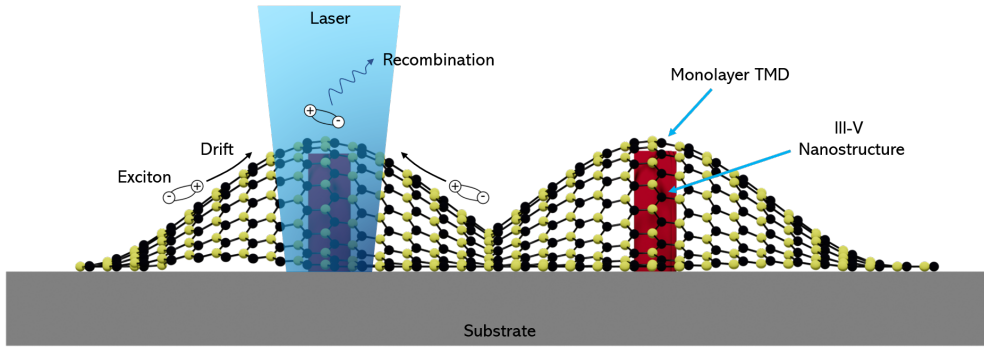


Figure 2.12 – Schematic illustration depicting a monolayer TMD conforming to a nanopillar substrate.

and the strain gradients can then funnel these excitons to points of maximum strain.

One of the remarkable aspects of straining monolayer TMDs is the possibility to engineer localized regions of high strain. This results in the formation of microscopic regions with a lower bandgap. When excited with a laser beam, excitons generated in the TMD material drift towards such lower bandgap regions before recombination, concentrating carriers in a small region of the TMD material. This is referred to as "funnel effect." Such a device structure was proposed and demonstrated as a tunable broad spectrum solar energy funnel [112]. This is schematically illustrated in figure 2.12, where a monolayer of TMD (MoS₂, for example) is deposited on an array of nanopillars. This device structure allows for deterministic and scalable creation of SPEs. Monolayer WSe₂ was deposited on SiO₂ nanopillar array to induce local strain [34, 35]. A near-perfect (96%) yield of SPEs can be obtained by this method [34]. Moreover, the dimensions of the nanopillars affect the properties of SPEs. For example, the spectral stability and density of emitters depends on the height of the nanopillars [34, 35]. Thus, by modifying the underlying nanostructure morphology the strain profile, funneling effect and carrier collection can all be modified.

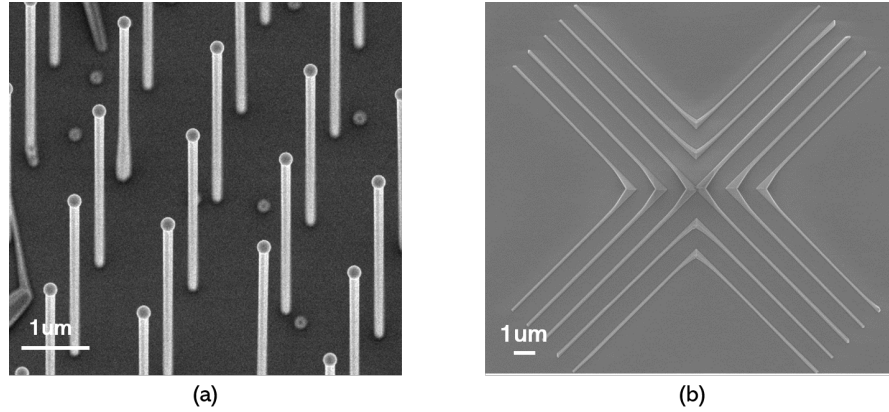


Figure 2.13 – SEM images of (a) a vertical nanowire array and (b) a horizontal nanowire cross.

2.2.4 Integration with III-V nanostructures

We now look at how combining monolayer TMDs with III-V semiconductor materials presents several advantages. Firstly, the properties of the SPEs hosted by TMDs can be drastically improved. Secondly, how various strain profiles can be imposed in the TMDs using different III-V nanostructure geometries.

Charge and/or electric field fluctuations are often observed in solid-state SPEs. Such fluctuations are caused by the charge traps that exist in the environment surrounding the SPEs. They can generate fluctuating electric and magnetic fields which lead to a variation in the energy of the photons emitted. In case of TMDs, deterministic SPEs were mostly fabricated on SiO_2 substrates. The varying charge environment in SiO_2 leads to spectral wandering and blinking of the SPEs [122] which can be on the order of several meVs [29]. On the other hand, monolayer WSe_2 deposited on InGaP substrates was shown to practically eliminate spectral wandering and reduce the emission linewidth [122]. Thus, high quality III-V substrates could further enhance the quality of SPEs in monolayer TMDs.

High-quality III-V semiconductors can be grown using well-developed epitaxial techniques such as MBE. Defect-free III-V nanostructures can be grown in many different geometries, such as vertical nanowire arrays and horizontal nanomembranes as shown in figure 2.13. Combining monolayer TMDs with III-V nanostructures, varying amounts of strain can be applied to TMDs depending on the nanowire shape and dimensions. The width and pitch of the nanowire arrays provides an additional knob for strain tuning. The geometry of nanowires has an added advantage. The light emission and absorption in vertical NWs is known to be efficient compared to the planar configuration, as discussed in section 2.1.1. The photons emitted due to recombination of localized excitons funneling to the NW tip can be extracted efficiently.

Band alignment at the III-V/TMD interface

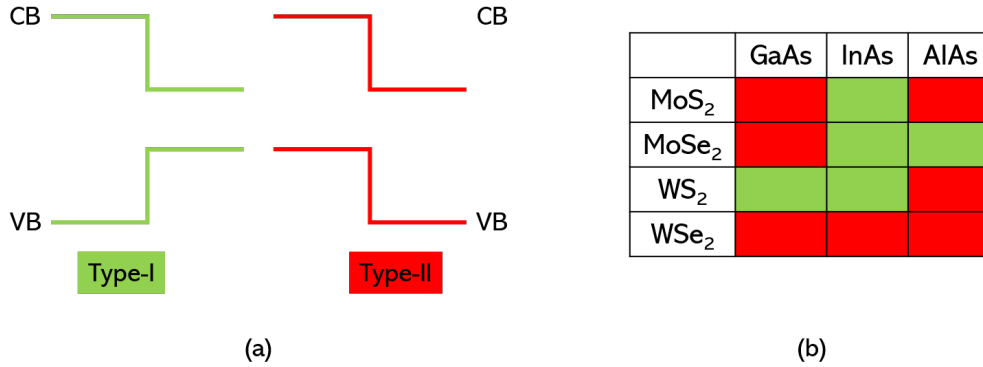


Figure 2.14 – (a). Types of band alignment in semiconductors. (b) Types of heterostructures formed between monolayer TMDs and various III-V semiconductors [10]

III-V semiconductors can be combined into multinary alloys. For example, AlAs and GaAs can be combined to form an $\text{Al}_x\text{Ga}_{1-x}\text{As}$ alloy. The bandgap of the alloy can be continuously tuned by changing the composition. Thus, combining monolayer TMDs with III-Vs enables creation of different types of band alignments at the interface. Type-I or type-II heterostructures can be formed by carefully choosing the material combinations. Figure 2.14 shows the types of band alignments calculated from first-principles DFT calculations [10] between III-As compounds and Mo- and W-based TMD monolayers. This bandgap alignment provides an additional knob for carrier injection into or out of the TMD monolayer.

The optical spectra of monolayer TMDs, such as MoS₂ and WSe₂ are dominated by excitons, which are electron-hole pairs bound together by a strong Coulomb interaction [123, 124]. By introducing an additional charge carrier, rich physical properties of charged excitons can be exploited. A charged exciton or trion consists of three charged particles (one e^- and two h^+ or two e^- and one h^+) bound together. Trions are preferred over neutral excitons since they can preserve spins on longer timescales (several ns) compared to neutral excitons [125]. The radiative relaxation of a trion to the ground state is accompanied by the emission of a circularly polarized photon and either an electron or a hole is left behind. This additional charge carrier can preserve its spin state for at least a few ns. This longer valley lifetime of trions might be sufficient for performing several quantum gate operations.

In TMDs, trions can be introduced externally either via electrostatic gating [123] or engineering the band alignment [126]. Electrostatic gating, however, requires complex fabrication processes. Doping, on the other hand, can be achieved by creating heterojunctions with a suitable band alignment. Type-II heterojunction, for example, was used to introduce trions in a WSe₂/CrI₃ heterojunction. By transferring the heterojunction to a nanopillar structure, localized trions were obtained [127]. Therefore, integration of monolayer TMDs with III-V nanostructures is promising to explore the novel optical properties in TMDs. The heterostructure integration can also enable large-scale integration of bright SPEs using strain engineering.

3 Methods

In this chapter, the basics of various experimental techniques used to obtain the results in this thesis are described. Firstly, the samples preparation methods are discussed. The samples studied in this thesis were prepared by two methods. First is the bottom-up growth of nanowires and their heterostructures by molecular beam epitaxy (MBE). The nanowires were also integrated with 2-D materials using a polymer transfer method. Secondly, we present various characterization methods. Techniques based on electron-matter interactions such as scanning and transmission electron microscopy (SEM and TEM) and cathodoluminescence (CL) and optical characterization techniques of Raman and photoluminescence (PL) spectroscopy are discussed.

3.1 Growth and Fabrication

3.1.1 Molecular Beam Epitaxy

Epitaxial techniques have gained importance since late 1960s in the growth of materials due to their unique advantages. Growth by epitaxy enables (i) obtaining high purity materials with low defect density and (ii) abrupt modulation of composition and doping profiles. Epitaxial techniques include metalorganic vapor phase epitaxy (MOVPE), chemical beam epitaxy (CBE) and molecular beam epitaxy (MBE). MBE gained much more importance since the work of Cho and Ballamy in 1975 [128], where they showed the growth of high quality monocrystalline GaAs layers. Since then, MBE has enabled the growth of novel epitaxial heterostructures and devices and led to the rapid development of quantum structures. Today, MBE is used to grow high quality materials of group-IV and III-V semiconductors as well as metal-oxide semiconductors.

MBE is a technique to grow materials on a heated crystalline substrate under ultrahigh vacuum (UHV) conditions. The typical chamber pressures range between 10^{-9} - 10^{-10} Torr, which can be further reduced by increasing the pumping power. Thus the collision mean free paths between atoms and molecules are larger or comparable to the dimensions of the MBE

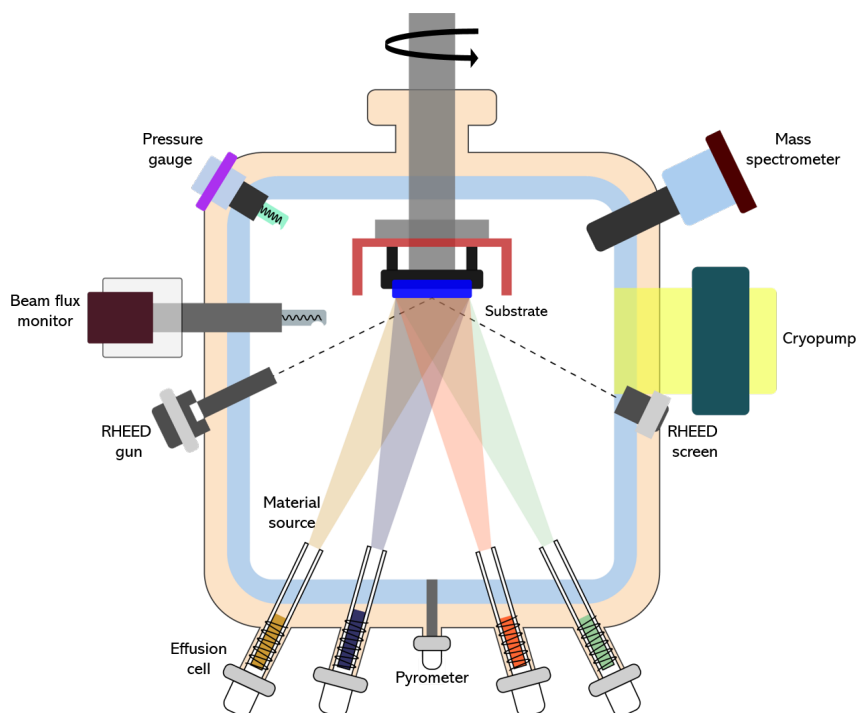


Figure 3.1 – Schematic illustration of the growth chamber in an MBE system

system. This results in ballistic, non-interacting paths of the source beams which can be abruptly interrupted using shutters. This allows to control the interface abruptness with a sub-monolayer precision. The constituent species in an MBE system are provided by atomic or molecular beams which are adsorbed on the substrate and interact to form the epitaxial layers. The use of high purity sources (6N, 99.9999 %) results in an extreme purity of the grown layers closer to the theoretical limit.

The results in this work were obtained using a DCA P600 UHV cluster MBE system. A schematic of the growth chamber is shown in figure 3.1. The substrate is loaded in the growth chamber upside down facing towards the material sources. A substrate manipulator is used to control the substrate heating and rotation during growth. A z-stage is used for loading and unloading of the sample into the growth chamber. The substrate is heated using an infrared heater element made from pyrolytic boron nitride (PBN) positioned above the substrate. The substrate temperature is maintained using a thermocouple for feedback. The temperature during growth can be monitored in-situ using a pyrometer.

The system is equipped with ten ports for various effusion cells and valved cracker cells. Each cell is combined with a pneumatically controlled shutter which provides binary control over the material fluxes. This allows for an abrupt change in the material composition. The materials are heated using a resistive heating filament to obtain the desired flux. Group-III elements such as Ga, In and Al are provided by solid-source effusion cells.

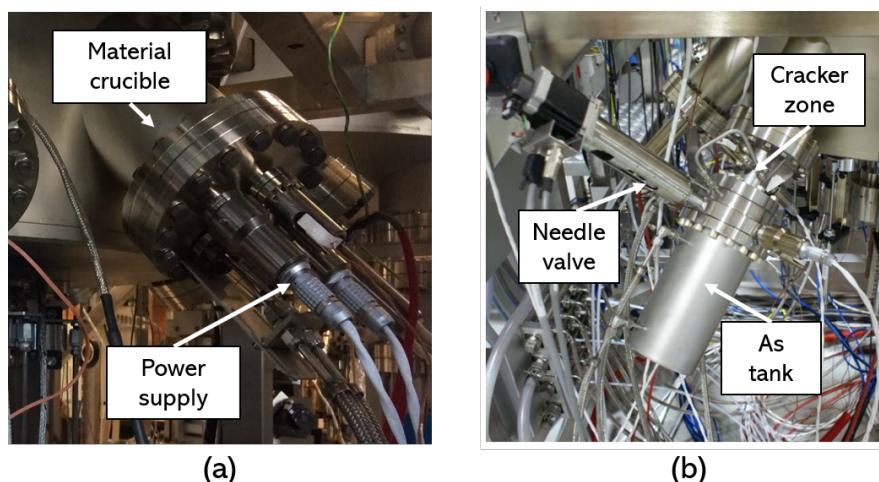


Figure 3.2 – (a) An effusion cell. (b) Arsenic valved cracker cell

Due to their high vapor pressures, group-V elements such as arsenic are supplied using a valved cracker cell. The construction of such a cell is slightly different than the standard effusion cell as shown in figure 3.2 (b). It consists of two separate temperature zones. The first zone is called as As tank and contains the bulk As material. It is heated and maintained at sublimation temperatures of As, around 350 - 400°C. Arsenic sublimates in the form of As_4 molecules. The flux of As_4 is controlled using a needle valve and passes through the cracker which is heated to much higher temperatures around 900°C. This cracks As_4 molecules into As_2 molecules. For all the nanowire growths described in this work, As_4 is used and the cracker is maintained at a relatively lower temperature of 600°C.

The high vacuum conditions in an MBE system are maintained by two cryopumps (CTI-8 and CTI-10), with a closed-loop He flow, connected to the growth chamber. The gaseous contaminants are trapped onto cold surfaces within the pump by means of cryocondensation. The chamber purity is monitored using a mass spectrometer or residual gas analyzer (RGA) to detect different gaseous species present within the growth chamber. The chamber pressures are measured using dual-filament ion gauges. A beam flux monitor (BFM) is mounted on a separate retractable arm which extends directly below the substrate and measures the source fluxes in the form of beam equivalent pressure (BEP). It is directly related to the number of atoms arriving at the substrate and after calibration, gives the deposition rate.

In an MBE system, the growth rate can be monitored in-situ using a RHEED (reflection high energy electron diffraction) technique. The system is mounted with an electron gun and a phosphorescent screen. The electron beam is incident at a grazing angle of incidence ($< 5^\circ$) which results in electron scattering only from the surface. The interference between the scattered electrons results in a RHEED pattern characteristic of the thin film structure forming at the surface. By monitoring the diffracted spot intensity, the growth rate can be calibrated with a monolayer precision. Since RHEED calibrations can be time consuming they are performed

less frequently. In our growths, they were rather linked to the BFM calibrations which are quick and can be performed more frequently for monitoring the growth rate reproducibility.

The quality of the grown sample depends on the quality of the substrate introduced. Therefore, it is essential to ensure the purity of the substrate before it is introduced into the growth chamber. MBE system consists of two dedicated chambers connected to the growth chamber it undergoes degassing processes to rid the substrate of any contaminants. (i) Loadlock chamber: substrate is heated to 120°C to degas water vapor. (ii) Degas chamber: substrate is heated to 600°C to degas organic contaminants present on the surface.

3.1.2 Exfoliation and transfer of 2-D materials

Nowadays, atomically thin 2-D materials are routinely isolated from bulk crystals using a simple scotch tape exfoliation method. One of the main reasons the field of van der Waals materials took off so rapidly was due to the development of experimental techniques that allowed us to precisely transfer them from one substrate to another. Using such transfer methods, different 2-D layers can also be stacked on top of each other like a "LEGO" set and there is no limitation on the number of layers that can be stacked together. During stacking, the alignment angle between two layers can also be defined precisely. For example, graphene and boron nitride (h-BN) monolayers are routinely stacked into artificial bilayers to study the resulting Moiré patterns [37]. Monolayers of 2-D materials can be also be capped with a protective layer which improves their optical and electronic properties [129].

In this thesis, we have used various transfer methods to integrate TMD flakes with different substrates such as Si/SiO₂, Au thin films, planar GaAs substrates and GaAs nanowires on Si and GaAs substrates. Various techniques are available for integrating 2-D flakes with different substrates [37] such as: (i) PMMA carrier layer, (ii) Elvacite sacrificial layer, (iii) wedging transfer method, (iv) PDMS dry transfer, (v) van der Waals pickup and (vi) polymer transfer methods. We have used the PDMS dry transfer method and polymer transfer methods to pick and place monolayer flakes of TMDs onto desired substrates [37]. The flakes are initially exfoliated from a bulk crystal onto an SiO₂/Si substrate. This allows easy optical identification of few layer flakes using an optical microscope. These flakes are then transferred using a transfer methods to a desired substrate. The detailed processes of exfoliation and transfer are described below.

Figure 3.3 shows the process of exfoliation of MoS₂ flakes on an SiO₂/Si substrate as an example. (a) A piece of scotch tape is pressed onto a bulk MoS₂ crystal. (b) The tape is then peeled off rapidly. The tape now consists of a few layer MoS₂ flakes. (c) This piece of tape is then pressed onto an SiO₂/Si substrate. (d) The tape is then gently peeled off, where few layer flakes get transferred to the substrate. These flakes are then inspected using an optical microscope to identify monolayers (inset in (d)). Raman and PL spectroscopy in conjunction with AFM are also used to confirm the flake thickness to be a monolayer.

3.1. Growth and Fabrication

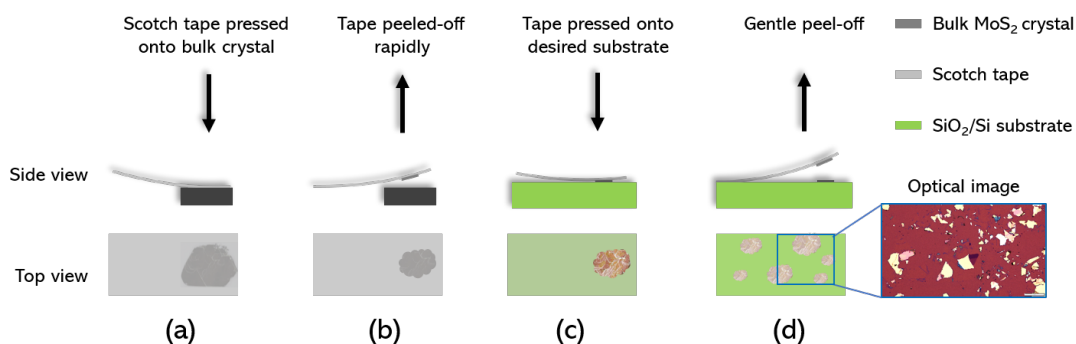


Figure 3.3 – Scotch tape exfoliation process. The inset shows an optical image of MoS₂ flakes exfoliated onto an SiO₂/Si substrate

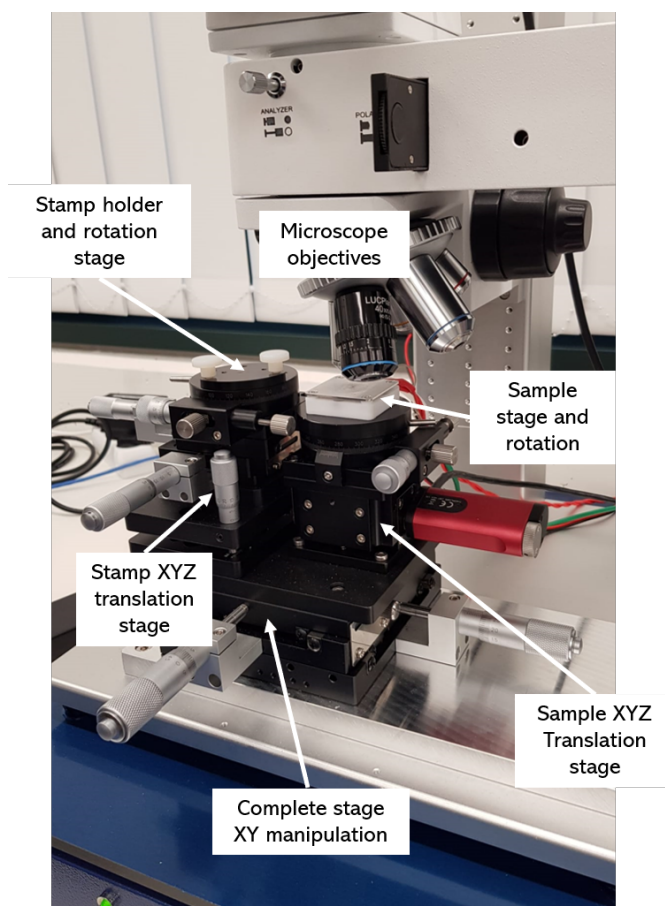


Figure 3.4 – A manual transfer station used for flake transfer.

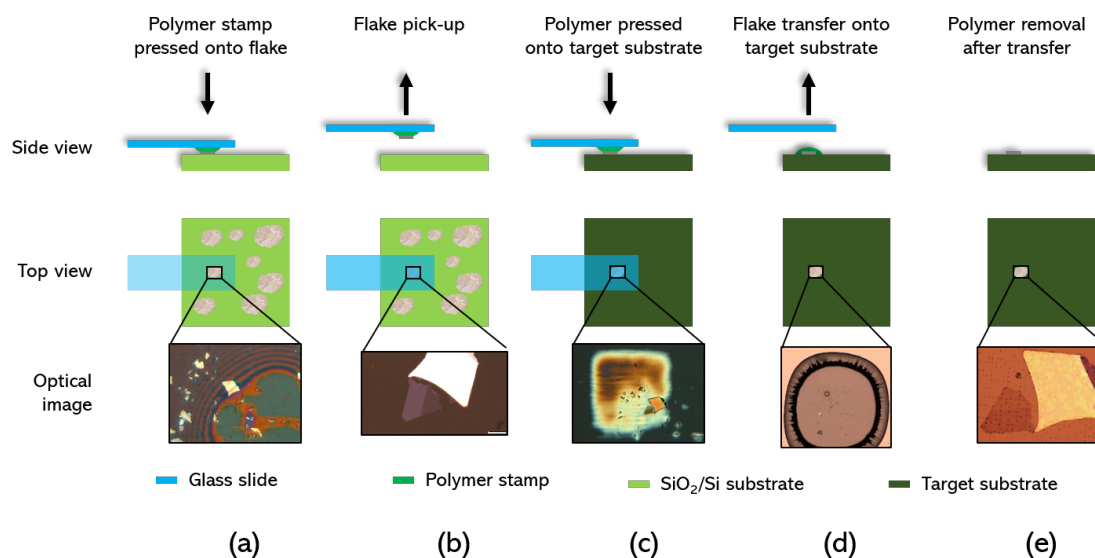


Figure 3.5 – Illustration of the polymer transfer method showing the side view, top view and optical image taken at each step during the transfer process.

Once monolayers are identified, they are then transferred to a target substrate (vertical nanowires grown on Si, for example) using one of the transfer methods. A manual or an automatic transfer stage is used for the transfer. Figure 3.4 shows the manual transfer stage which was used for this work. It consists of two main components, the stamp stage and the sample stage. The sample stage has XY translation and rotation capabilities. The sample stage has XYZ translation, rotation and heating capabilities. The sample stage can be heated up to 200°C for better polymer sticking and melting during transfers. Microscope objectives and a control software are used to optically navigate on the stamp and the sample.

A polymer transfer method is schematically illustrated in figure 3.5. The polymer stack consists of a poly bisphenol A carbonate (PC) film on a PDMS cube on a glass slide. A small cube (1 mm) is cut from a freshly prepared PDMS film and placed on the glass slide. A PC film coated onto a glass slide is peeled off using a piece of scotch tape. An aperture is cut through the tape where the floating PC film will act as a membrane and the tape surrounding it provides mechanical support. This is then placed on the PDMS cube and the glass slide is then ready to pick up the flake. The glass slide is fixed on the stamp stage and aligned with the substrate which is placed on the sample stage as shown in figure. After heating the sample stage to 70°C, the stamp is aligned with the monolayer flake on SiO₂/Si substrate. The sample stage is then brought in contact with the stamp and the temperature raised between 80 - 90°C where the PC film sticks to the flake on the substrate (figure 3.5 (a)). The temperature is then slowly reduced to pick up the flake (figure 3.5 (b)). Once the flake is on the stamp, the target substrate is then placed on the sample stage. The flake on stamp is aligned precisely with the desired area on the target substrate (nanowire arrays in our case). By bringing the stamp gently in contact with the substrate (figure 3.5 (c)), substrate temperature is slowly and steadily raised to 180°C.

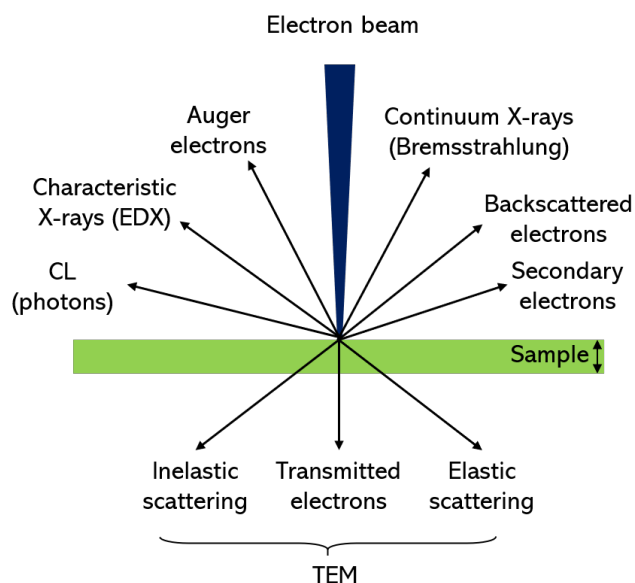


Figure 3.6 – Schematic showing different signals resulting from the interaction of a high energy electron beam with a sample.

Once the polymer melts, the melted polymer area in contact with the substrate is separated from the stamp by manipulating the z-stage (figure 3.5 (d)). The polymer blob is then cleaned in chloroform for 30 mins followed by cleaning in isopropyl alcohol for 5 mins. The flake is then successfully transferred to the desired area on the substrate (figure 3.5 (e)). An optical image of the sample at each stage of transfer is shown in the bottom insets of figure (figure 3.5).

3.2 Characterization

Following sample preparation, characterization is necessary to study the relationship between materials processing and structural/ functional properties. We have used electron microscopy to study the structural properties and optical spectroscopy to study the functional properties of the fabricated samples.

3.2.1 Electron Microscopy

Transmission Electron Microscopy

Electron microscopy can be used to gain valuable information about the structure, morphology and composition of a sample. It relies on the interaction of electrons with a material. When an electron beam impinges the sample, a multitude of signals are emitted. Figure 3.6 shows the various interactions that can occur. The interaction of electrons with the sample can be classified into two types: elastic scattering and inelastic scattering. In case of elastic scattering,

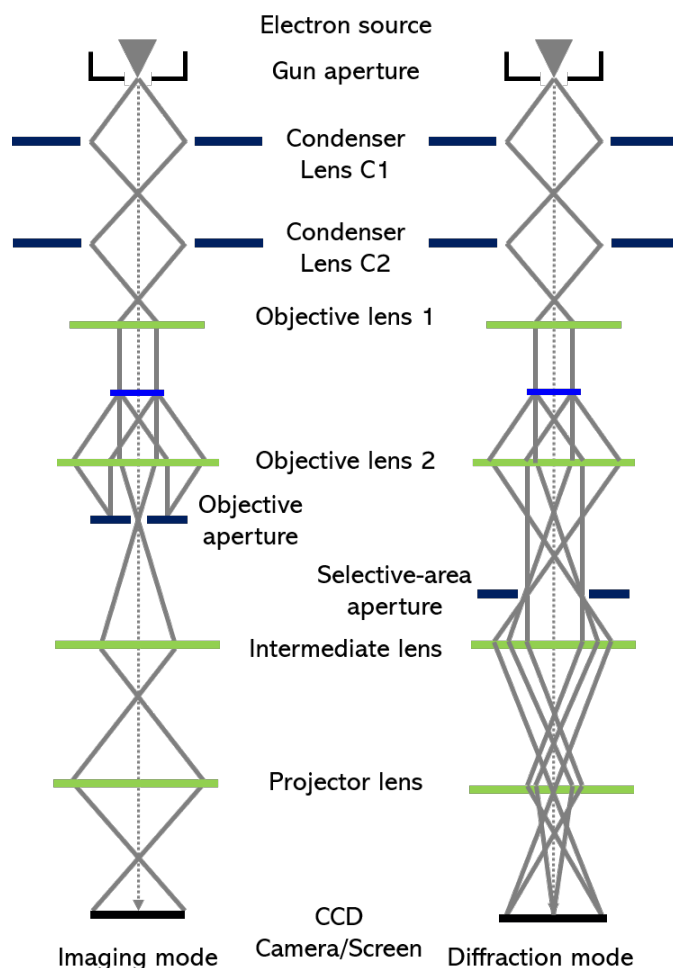


Figure 3.7 – Ray diagram illustrating the path of electrons when the TEM is operated in imaging vs. diffraction mode.

the electrons are deflected due to electrostatic interaction with atomic nuclei and surrounding electrons. The scattered electron has same energy as the incident electron. When the scattering is coherent, Bragg diffracted electrons can be used to generate diffraction patterns which hold information about the crystal lattice. Using an aperture, either the transmitted or a diffracted beam can be selected for bright-field or dark-field imaging. Since diffracted beams have strongly interacted with the sample, dark-field imaging provides higher defect contrast. Incoherent scattering results from the difference in atomic number (Z) or sample thickness. This can be used to obtain Z -contrast or mass thickness contrast for crystalline and as well as amorphous materials.

Figure 3.7 illustrates the path of electrons within a TEM operated in imaging and diffraction modes. Electrons ejected from the source accelerate towards the sample. The two condenser lenses (C1 and C2) define the probe and control the illumination area on the sample, ensuring sample illumination by a parallel beam of electrons. A combination of upper and lower

objective lenses form the image. An objective aperture is placed at what is called the back focal plane where the diffracted beams are formed. In the imaging mode, either the transmitted or one of the diffracted beams can be selected using the objective aperture and the system can be configured for bright-field or dark-field imaging. In the diffraction mode, a selective-area aperture is inserted in the image plane to obtain diffraction pattern from only a small region of the sample. The intermediate lenses are adjusted to switch between imaging and diffraction modes as well as change the image magnification and compensate for image rotation as a result of spiraling of electrons. Lastly, projector lens is used to magnify the image onto a detector.

The electron interaction with the sample can also result in inelastic scattering where the scattered electrons lose energy when they interact with the sample. This can result in the emission of characteristic X-rays, secondary electrons, backscattered electrons, Auger electrons, phonons, plasmons and photons. The emission of characteristic X-rays provides a powerful analytical tool for composition analysis. An incident electron can transfer part of its energy to another electron in the inner shell of an atom. When the inner shell electron is ejected, an electron from a higher state relaxes to fill the vacancy. This results in the emission of an X-ray photon with energy which is the characteristic of an inner shell transition and is unique for each atom. Thus, elemental composition of the sample can be identified using the X-ray fingerprint within an error of few percent. This scattering usually occurs at high scattering angles. Therefore, a high-angle annular dark-field (HAADF) detector is mounted in the TEM column which can collect these X-rays. Using energy-dispersive X-ray (EDX) spectroscopy combined with sample mapping, local composition variations within few nanometers can be studied.

The TEM system used throughout this work was an FEI Talos F200S microscope with a high-brightness field emission gun source. The microscope is operated at 200 keV and operating currents of 100 pA for high-resolution TEM and 1 nA for STEM imaging. The resolution was on the order of 0.25 nm. The system is equipped with BF and DF detectors and two HAADF detectors for EDX spectroscopy. The samples are loaded on a double tilt holder which allows for the sample alignment on the zone axis for high-resolution TEM imaging. We have used HR-TEM to study the morphology, defects and stacking faults in the InAs/GaAs nanowire heterostructures. HAADF-STEM and EDX were used to obtain elemental contrast and mapping in the nanowires.

Scanning Electron Microscopy

SEM was routinely used for checking the growth of nanowires. The SEM microscopes used in this work are Zeiss LEO 1550 and Zeiss Merlin equipped with field emission gun source and in-lens and secondary electron detectors. The in-lens detector is located in the beam path and detects only the secondary electrons. While in case of the SE detector, electrons are attracted by a collector and detects secondary and backscattered electrons. The collector bias can be tuned to reject low energy backscattered from the sample producing a

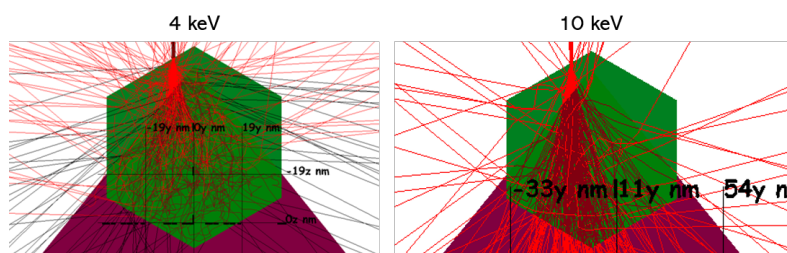


Figure 3.8 – Electronic transitions generating X-rays as a result of ejection of an inner shell electron.

backscattered image enhancing the topographic contrast. The secondary and backscattered electrons emitted from the sample are collected to obtain information about the sample morphology and surface topography. Low beam energies in the range of 3 - 5 keV were used. Higher beam energies were sometimes used for subsequent generation and detection of X-rays using an EDX detector and obtain quantitative elemental information. The resolution of SEM-EDX is lower compared to STEM-EDX..

Cathodoluminescence

When a semiconductor is hit by an electron beam, some of the electrons can contribute to the generation of electron-hole pairs. The electrons from the valence band are promoted to the conduction band. The electrons relax from the excited state by recombining with a hole followed by the emission of a photon. This generation of luminescence upon excitation with an electron beam is termed as cathodoluminescence (CL). The electron excitation is carried out in an SEM microscope, hence it is commonly referred to as SEM-CL. SEM-CL combines the high spatial resolution of SEM with optical spectroscopy. In a CL measurement, the sample is typically scanned with an electron beam and an optical emission spectrum is acquired at each point. This type of measurement results in hyperspectral maps where each point contains an intensity vs. wavelength spectrum. The maps can then be analyzed alongside STEM maps to study the correlation between the material structure and properties.

When an electron interacts with a sample, multiple scattering events can occur before the electron exits the sample. This region of the sample where electron-sample interactions take place is called the interaction volume. If the accelerating voltage is high enough, the interaction volume can spread well beneath the sample surface. This can then limit the spatial resolution of CL. This is illustrated with an example in figure 3.8 where a nanowire is bombarded with an electron beam with energies of 4 keV and 10 keV. The results are obtained using Monte-Carlo simulations using the software CASINO. When the energy is lower (4 keV), most of the interaction is limited closer to the surface. When the beam energy is increased to 10 keV, the beam penetrates deeper within the sample and results in a much larger interaction volume. Lower accelerating voltages can be used to limit the interaction volume. This can result in a lower number of photons generated per electron, thus, a lower CL signal. Nevertheless, lower accelerating voltages can still help in improving the CL resolution. Carriers generated from CL

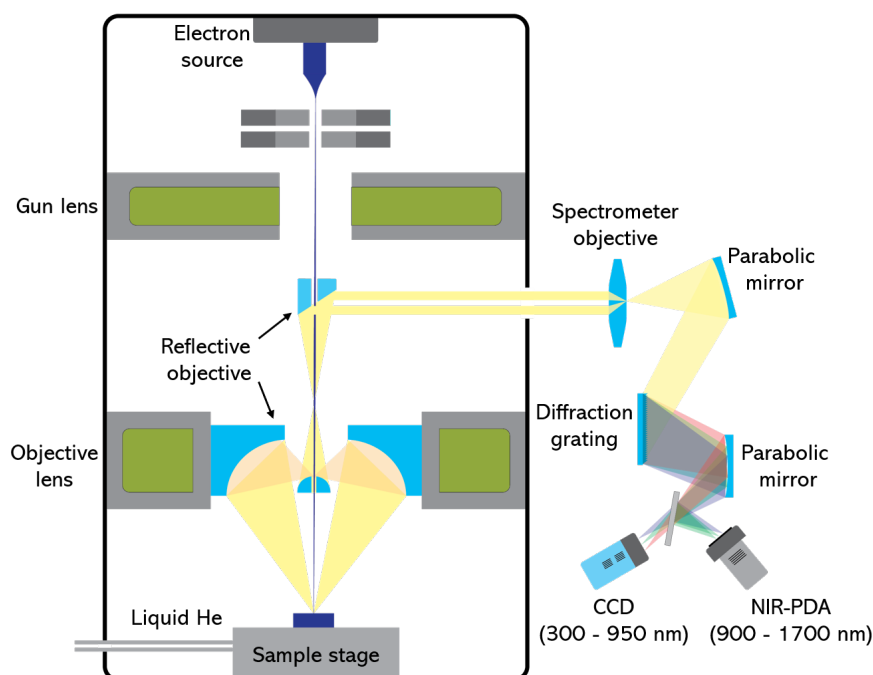


Figure 3.9 – Schematic of the CL setup.

excitation can also diffuse spatially before they can recombine. This is specially pronounced when surface defects or traps are present. The emission signal is then generated far from the point of excitation. In nanostructures, the diffusion length can be still be limited within 1 μm range. The overall resolution of CL depends on the accelerating voltage used, interaction volume within the sample and carrier diffusion process.

The CL system used in this work is an Attolight Rosa dedicated SEM-CL microscope. A schematic of the system is depicted in figure 3.9. The microscope is equipped with a column similar to a standard SEM microscope with a Schottky thermal field emission gun source. The electron beam energy can varied between 1 - 10 keV. Gun lens and objective lenses focus the electron beam onto the sample with a spot size of 10 nm. The sample sits on a liquid He-cooled holder which can cool down the sample down to 10 K. The system is equipped with a Faraday cup. The probe current in the microscope can vary between 5 and 20 nA. The sample can be imaged using an Everhart-Thornley secondary electron detector.

The optical components to collect the CL signal consist of a reflective objective and a tilted parabolic mirror along the microscope column. These are pierced with a hole to allow the electron beam to pass. The reflective objective and parabolic mirror focus and direct the CL signal into the spectrometer. The spectrometer assembly consists of an objective which focuses the incoming signal to the entrance slit where parabolic mirrors and diffraction grating work in conjunction to spectrally resolve the CL signal (into an intensity vs. wavelength spectrum) and direct it to the charge-coupled detector (CCD). The signal can be directed to two different CCDs for detection of light either in the near UV-Visible light (300 - 950 nm)

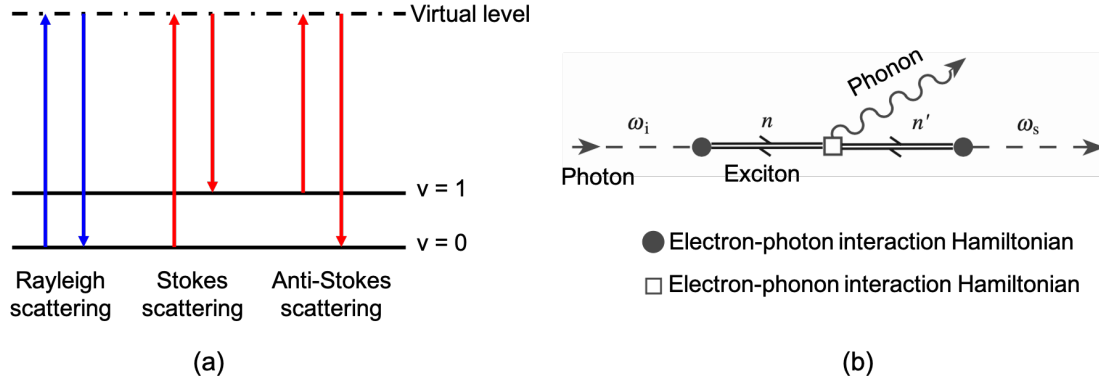


Figure 3.10 – (a) Vibrational energy levels involved in Raman scattering. (b) Feynman diagram of the one-photon (Stokes) Raman scattering.

range (Si CCD) or in the near infrared (NIR, $0.9 \mu\text{m} - 1.7 \mu\text{m}$) range. The spectrum at each point is recorded along with 2-D pixel coordinates to obtain hyperspectral maps.

3.2.2 Optical spectroscopy

Raman spectroscopy

Raman spectroscopy, discovered by Dr. C. V. Raman, is a non-destructive technique used to study the structure and composition of materials by characterizing their vibrational properties. The sample under study is excited using a laser beam and the scattered light is detected. Most of the incident laser light is scattered elastically such that the energies of the incident and scattered photons is the same ($\lambda_{\text{scattered}} = \lambda_{\text{laser}}$), otherwise known as Rayleigh scattering. A small fraction of light (1 in 10^7 photons) is scattered inelastically, where the scattered photons have an energy either lower (Stokes scattering) or higher (anti-Stokes scattering) than the incident photons. Raman effect is a result of the interaction of photons with the electric dipole of a molecule. Figure 3.10 (a) shows an energy level description of Raman scattering. The laser photon excites the molecule to a virtual state which can then relax to either same (Rayleigh), lower (Stokes) or higher (anti-Stokes) vibrational level. The intensity of scattered light is then plotted against the Raman shift, which is the energy difference between incident and scattered photons. Raman shift is commonly expressed in wavenumbers (cm^{-1}) and calculated as:

$$\nu = 1/\lambda_{\text{laser}} - 1/\lambda_{\text{scattered}}$$

According to the microscopic theory of scattering, the Raman process proceeds in three steps [51],

(a) An incoming photon with frequency ω_i excites the semiconductor into an intermediate state $|n\rangle$ and creates an electron-hole pair or exciton. The process is mediated by the electron-

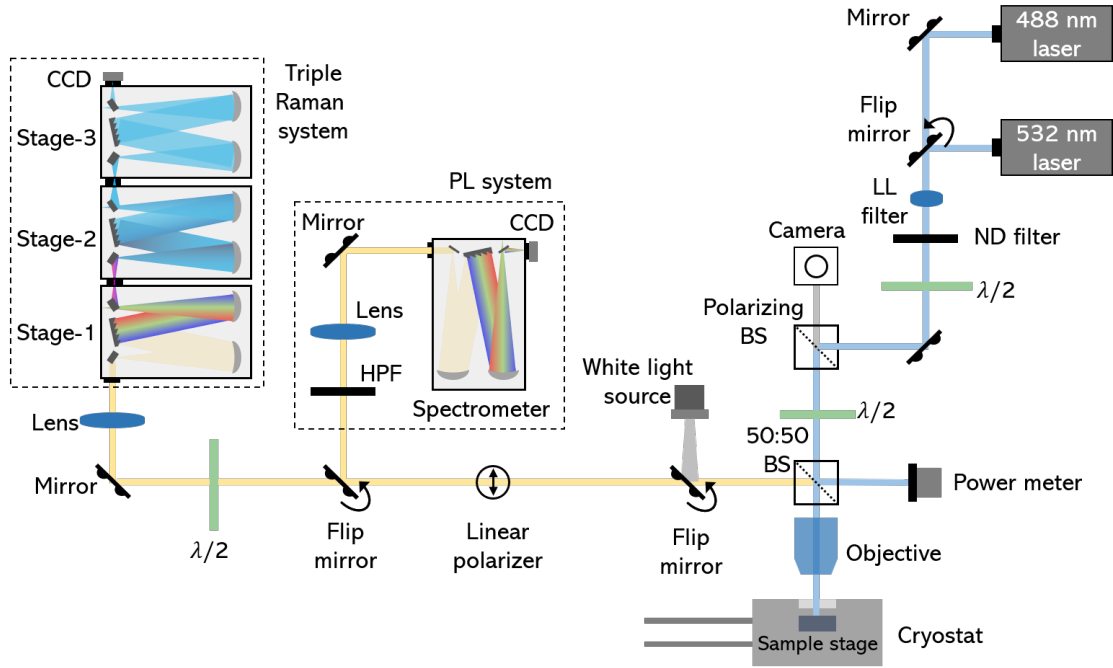


Figure 3.11 – A schematic of the optical setup configured for both Raman and photoluminescence measurements. A flip mirror is used to divert the signal towards either the triple Raman system or the PL detection system. LL: laser line; ND: Neutral density; BS: Beamsplitter; HPF: Highpass filter.

radiation interaction Hamiltonian H_{e-r} .

(b) The electron-hole pair is scattered into another state $|n'\rangle$ by the lattice by emitting a phonon. This process is mediated by the electron-phonon interaction H_{e-ion} .

(c) The electron-hole pair in state $|n'\rangle$ recombines radiatively and a scattered photon with frequency ω_s is emitted, mediated by H_{e-r} .

This process is illustrated by the Feynman diagram in figure 3.10 (b). The electrons mediate the Raman scattering process although they remain unchanged after the scattering process. The transitions involving electrons are, thus, virtual. The interactions shown in figure 3.10 (b) proceed sequentially as a function of time. Other possible scattering processes can be derived by permuting the time order of the three vertices in (b). As a result of time reversal invariance, the Feynman diagrams in figure 3.10 read from right to left will describe the anti-Stokes Raman scattering process.

Two different setups have been used in this work to carry out the Raman measurements. The first is a Renishaw inVia confocal Raman system (not shown here) configured for use with four different lasers (405 nm, 532 nm, 488 nm and 785 nm). The system is coupled with a charge-coupled detector via a high resolution spectrometer consisting of gratings to disperse the Raman signal. The 532 nm laser combined with a 3000 l/mm grating provides a maximum

Chapter 3. Methods

Raman spectral resolution of 0.8 cm^{-1} . Raman spectrum is plotted in terms of photon energy shift of the Raman signal with respect to the incident laser energy. For the materials studied here (TMDs), this is typically around 50 meV, which is very close to the laser energy. This results in a strong laser background, resulting from Rayleigh scattering, which interferes with the Raman signal. A common approach is to use a separate holographic notch filter (Rayleigh filter) to block the laser line, as applied in this setup.

The second setup represents a more versatile configuration for laser line suppression and stray light rejection. Figure 3.11 shows a schematic of such a setup. The main difference lies in the detection stage labeled as triple Raman system consisting of three 500 mm focal length monochromator stages. Each stage consists of two gratings 900 l/mm and 1800 l/mm. The setup can be operated in subtractive or additive mode. In subtractive mode, Raman signal entering the first monochromator stage is dispersed by the first grating. The intermediate slit between first and second stage acts as a bandpass filter selecting only part of the spectrum. This filters out the laser line and stray light thereby providing a high signal-to-noise ratio. The grating in the second stage collects this light and focuses it onto the entrance slit of the third stage. The third stage grating then disperses this light and focuses it onto the detector. The setup can also be used in additive mode, where each stage further disperses the incoming light from the previous stage to providing a maximum resolution for the setup. The setup provides a maximum resolution of 0.2 cm^{-1} at 500 nm when used in the additive mode. The triple Raman system is configured for use with two different semiconductor lasers (488 nm and 532 nm). The incoming laser power can be tuned using ND filters. Alternatively, a half waveplate in conjunction with a polarizing beamsplitter, which transmits only vertical polarization of light, can be used to tune the power continuously. A 50:50 beamsplitter is then used to divert the incoming signal towards a power meter which is used to monitor the laser power. A 63x objective with NA 0.85 is used to focus the signal onto the sample and also collects the signal emitted from the sample. This setup provides a spatial resolution of about $1\text{ }\mu\text{m}$. The sample stage consists of a liquid He-cooled cryostat placed on an XYZ translation stage which was used to carry out measurements from room temperature down to 10K. A white light source in conjunction with a camera is used for sample imaging and navigation. The Raman signal is detected using a liquid nitrogen-cooled Si charge-coupled device. For polarization-dependent Raman measurements, the polarization of the scattered signal can be selected using a combination of a linear polarizer and a half waveplate.

Photoluminescence

Photoluminescence (PL) is a commonly used spectroscopy technique to study the optical properties of semiconductors. In PL, a semiconductor is optically excited using a source with energy higher than the bandgap. This leads to creation of electron-hole pairs. The electrons and holes thermalize non-radiatively and relax to the conduction and valence band edges. Following this, they recombine radiatively with the emission of a photon. Electrons and holes can recombine through various recombination processes as shown in figure 3.12. These are (a) band-to-band recombination, (b) free to bound transition between a free carrier and a carrier

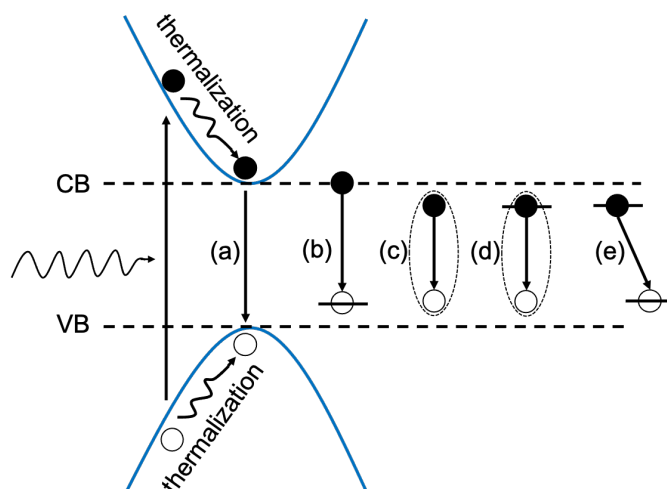


Figure 3.12 – Radiative recombination mechanisms in PL (a) band-to-band recombination, (b) free-to-bound transition, (c) free exciton recombination, (d) bound exciton recombination and (e) donor-acceptor pair transition. VB: valence band, CB: conduction band.

bound to a defect, (c) free exciton recombination, (d) defect-bound exciton recombination and (e) donor-acceptor pair transition due to capture of electron to a donor impurity and hole to an acceptor impurity.

The energy of the emitted photon depends on the bandstructure and energy levels of the sample. The emission is detected using a suitable detector and the intensity of emitted signal is plotted as a function of its wavelength (or energy). Various features of a PL spectrum provide information on the properties of the sample being studied. PL intensity indicates the material quality, since defects can reduce luminescence via non-radiative recombination channels. Peak position depends on the sample composition. Linewidth determines the homogeneous and inhomogeneous broadening. At room temperature, phonon-assisted homogeneous broadening can suppress the inhomogeneous broadening caused by local structural fluctuations. Therefore, it is common to carry out PL measurements at low temperature to suppress phonon-assisted scattering processes.

PL measurements in this work were carried out using the same setup shown in figure 3.11. A flip mirror is used to divert the emitted signal to the PL system. The optical setup before the flip mirror is the same as the Raman setup. The PL system consists of a highpass filter to spectrally filter out the laser peak allowing only the lower energy PL signal to pass through. The signal is dispersed using a diffraction grating (300, 600 and 1200 l/mm) onto a thermoelectrically cooled CCD.

In addition to the optical setups described above, additional Raman and PL mapping measurements were carried out using a custom-built Raman setup in the group of Prof. Paulina Plochcka, at the Wrocław University of Science and Technology. The basic working principle

Chapter 3. Methods

remains the same as the triple Raman system. In addition, motorized translation stages are used for mapping and the setup was used in a confocal configuration to improve the spatial resolution.

4 Results and Discussion

This chapter is a compilation of the main results of this thesis in the form of three manuscripts. Firstly, a brief summary of each manuscript along with my contributions is provided followed by the presentation of results.

4.1 Facet-driven formation of axial and radial In(Ga)As clusters in GaAs nanowires

A. Balgarkashi^{*}, S. P. Ramanandan^{*}, Nicolas Tappy, Mackrine Nahra, Wonjong Kim, Lucas Güniat, Martin Friedl, Nicolas Morgan, Didem Dede, Jean-Baptiste Leran, Christophe Couteau and Anna Fontcuberta i Morral.

Journal of Optics, Volume 22, Number 8 (2020)

^{*}equal contribution

This work is the result of first half of my PhD research work. Here, the focus was on growth of InAs/GaAs nanowire heterostructures. The aim of this work was to position a small InAs segment on the axis of a GaAs nanowire to act as a single photon emitter. GaAs NW arrays were grown on patterned Si substrates using Ga droplet as the catalyst. Whereas an ideal axial heterostructure requires sharp interface between the QD segment and surrounding barrier for a stronger quantum confinement, incorporating In directly into the Ga droplet during NW growth can result in a graded interface. We approached this issue by completely consuming the Ga droplet under As₄ flux before switching the NW material from GaAs to InAs. During this droplet consumption step, the droplet shrinks with a variation in the contact angle. This causes fluctuations in the morphology and crystal structure at the NW tip. We studied carefully the morphology and crystal structure at the NW tip using SEM and HR-TEM measurements. The tip was found to exhibit different morphologies and most of the NWs exhibited a truncated pyramidal tip.

Growth conditions (In flux and substrate temperature during growth) were then examined for placing a small (< 50 nm) axial segment of InAs on the NW. InAs was deposited in two different

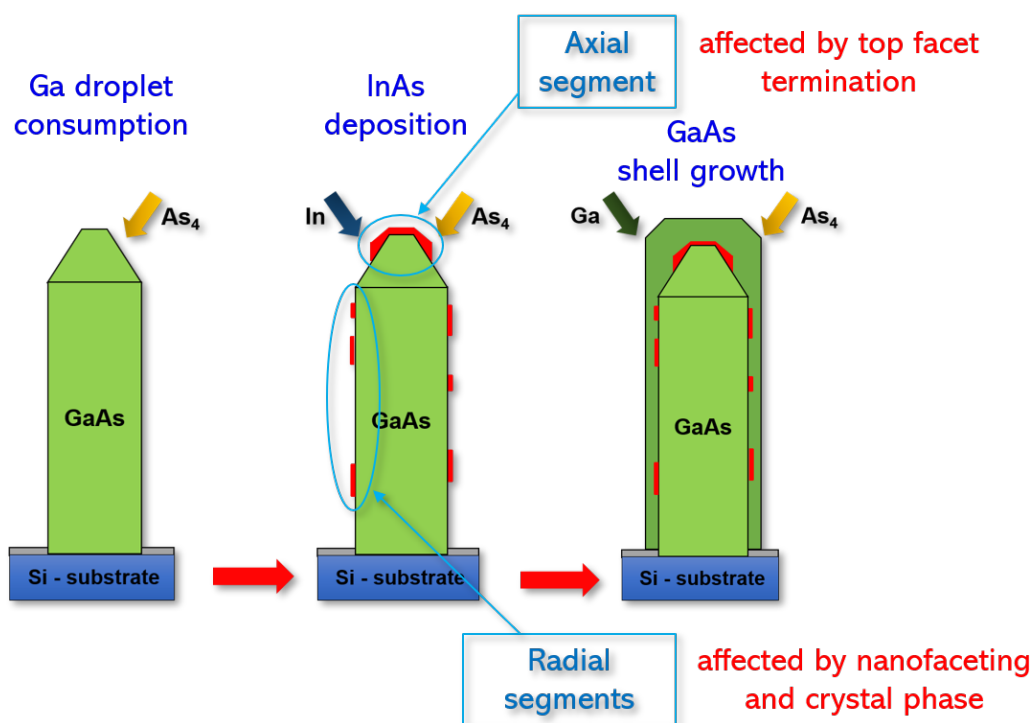


Figure 4.1 – Understanding the preferential accumulation of InAs clusters on GaAs NWs.

ways: (i) deposition of In droplet on NWs followed by crystallization under As_4 flux (*VLS method*), and (ii) direct deposition of InAs under (In + As_4 fluxes, *V-S method*). It was found that, when using the VLS method, In deposition at a planar growth rate as low as $\text{\AA}0.1/\text{s}$ for 5s resulted in droplet sizes of 90 nm. Therefore, the preferred method was direct V-S deposition to keep the InAs cluster size smaller.

The InAs segment was then capped with a GaAs shell for passivation and confinement. Uncapped and capped clusters were examined using HAADF-STEM atomic contrast and EDX maps were used to check their composition. In addition to a small InAs segment at the NW tip, InAs clusters were also found to accumulate along the NW sidewalls. This is shown with the help of a schematic in figure 4.1. Since the NW tip is faceted, preferential accumulation of InAs either on one of the facets or at the intersection of two facets is expected. However, it was challenging to determine the exact location of such segments. On the other hand, In(Ga)As clusters were observed only along the nanofacets present at the edges separating the two 110 NW side facets. Once the GaAs capping layer was grown, the clusters on NW sidewalls were found to be optically active. However, the axial segment emission was fully quenched due to a high density of defects induced during the capping layer growth.

My contribution to this work involved the substrate preparation, growth and imaging of all the samples. The TEM study was done in collaboration with master thesis student, Mr. S. Ramanandan. The optical characterization was done using PL and CL spectroscopy. I carried

4.1. Facet-driven formation of axial and radial In(Ga)As clusters in GaAs nanowires

out the CL measurements and analysis at EPFL. The PL measurements were carried out in the lab of Prof. Christophe Couteau at the Université de technologie de Troyes. I took part in the PL measurements done in collaboration with PhD student Dr. M. Nahra. I also analyzed the PL data.

4.1.1 Abstract

Embedding quantum dots in nanowires constitutes one promising building block for quantum photonic technologies. Earlier attempts to grow InAs quantum dots on GaAs nanowires were based on the Stranski-Krastanov growth mechanism. Here, we propose a novel strain-driven mechanism to form 3-D In-rich clusters on the NW sidewalls and also on the NW top facets. The focus is on ternary InGaAs nanowire quantum dots which are particularly attractive for producing single photons at telecommunication wavelengths. In(Ga)As clusters were realized on the inclined top facets and also on the {11-2} corner facets of GaAs NW arrays by depositing InAs at a high growth temperature (630°C). High-angle annular dark-field scanning transmission electron microscopy combined with energy-dispersive x-ray spectroscopy confirms that the observed 3-D clusters are indeed In-rich. The optical functionality of the as-grown samples was verified using optical technique of cathodoluminescence. Emission maps close to the NW tip shows the presence of optically active emission centers along the NW sidewalls. Our work illustrates how facets can be used to engineer the growth of localized emitters in semiconducting NWs.

4.1.2 Introduction

Single photon emitters (SPEs) are envisioned to play a central role in the future of quantum photonics. Their development is important for applications in quantum computation, quantum communication and quantum cryptography [130]. An ideal single-photon source is identified by a high fidelity and a high degree of anti-bunching ($g^2(0) \sim 0$), high brightness and narrow emission linewidth [131]. In recent years, bright single-photon emitters have been demonstrated by embedding semiconducting quantum dots (QDs) within nanowires (NWs) [24, 25, 132, 133]. Semiconductor QDs are three-dimensionally confined nanostructures with discrete, atom-like emission lines. Due to quantum confinement, electronic levels in a QD can be tuned by changing their size [134] and composition [133]. Conventional QDs are grown by planar epitaxy and embedded in a three-dimensional matrix of a higher bandgap material [135]. However, the total internal reflection at the bulk semiconductor/vacuum interface and the far-field divergence of the emission make the photon extraction highly inefficient from these structures [24, 85, 131]. NWs, on the other hand, can be designed to operate as photonic waveguides to enhance light extraction. Proper positioning of a QD on the NW axis allows the coupling of QD emission to the fundamental HE_{11} mode of the NW waveguide and coupling to other radiation modes is suppressed [24, 25, 27].

Apart from efficient light extraction, the size and morphology of the NWs offer several degrees

of freedom to form low dimensional heterostructures like QDs and quantum wells (QWs). It is possible to obtain axial and radial heterostructures in NWs by varying the material composition along the axial and radial directions, respectively [136, 137]. Moreover, NWs provide a wider choice of material combinations with a higher lattice mismatch for forming axial and radial heterostructures. For instance, in the case of III-V semiconductors, one can either change the group-III element or the group-V element to form heterostructures. Some further combinations are also possible with ternary alloys consisting of an additional group-III or group-V element (e.g., InGaAs, InAsP). The large aspect ratio of NWs helps to relax the misfit strain induced by the lattice mismatch on the sidewalls and prevents the occurrence of defects [14]. Out of the available material combinations, InGaAs nanowire quantum dots (NWQDs) are particularly of interest due to their ability to emit photons in the telecommunication wavelength range and with purity in excess of 99% ($g^2(t) < 0.01$) [44, 85]. Therefore, positioning InGaAs QDs on the axis of GaAs NWs is an attractive choice to realize single-photon sources.

Most reports on the III-V QDs in NWs are based on NWs grown using gold as the catalyst. However, the incorporation of gold into the grown semiconductor is found to be detrimental for its optical properties [138]. Although self-catalysed growth of defect-free ordered GaAs NW arrays are widely reported, NW axial heterostructures based on this method is still missing. In the case of III-V semiconductors, axial heterostructures are obtained by either changing the group-III element, like GaAs/InAs, GaP/InP, or the group-V element like GaAs/GaSb. More combinations are available if either A or B is a ternary alloy. GaAs QDs in AlGaAs NWs, InAsP QDs in InP NWs, and InGaAs QDs in GaAs NWs are a few examples. Despite the availability of a wide variety of material combinations, challenges like the reservoir effect [88] and kinking [139] limit their successful implementation.

Here, we take an alternative approach for switching between two materials (InAs and GaAs). The Ga droplet, used as a growth catalyst, is completely consumed before the deposition of InAs. Formation of axial and radial localized InGaAs clusters within self-catalysed GaAs NWs is observed. Specific focus is given to the structural characterization of the obtained heterostructures using transmission electron microscopy (TEM). Our findings provide new insights into how facets can be used to engineer the growth of QDs in semiconductor NWs.

4.1.3 Experimental Details

The GaAs NWs studied here were grown by the self-catalysed vapour-liquid-solid (VLS) method in a DCA P600 molecular beam epitaxy (MBE) system. A Si (111) wafer coated with an SiO₂ mask was patterned by e-beam lithography and used as the growth substrate. The NW growth was carried out at a substrate temperature of 630°C and at Ga and As₄ beam equivalent pressures (BEPs) of 1.4×10^{-7} Torr and 2×10^{-6} Torr, respectively. The Ga supply was interrupted after an hour of NW growth. The Ga droplet used as a catalyst in the NW growth was then completely consumed under an As₄ flux of 7.2×10^{-7} Torr. InAs was deposited for 5s at a substrate temperature of 630°C under an As₄ BEP of 5.6×10^{-6} Torr and at a V/III ratio of 45.

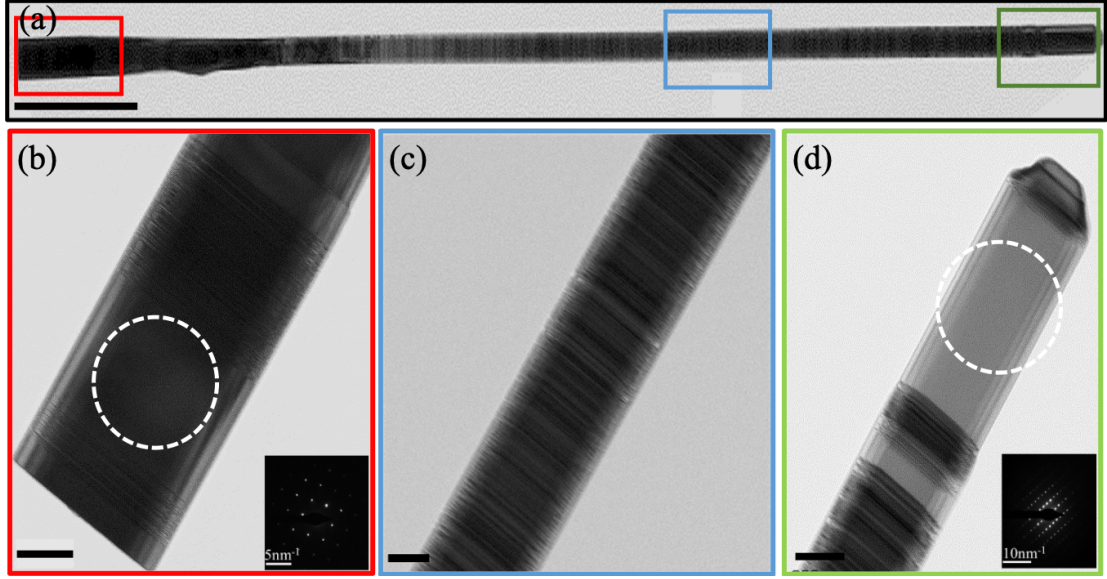


Figure 4.2 – (a) A TEM image showing overview of a GaAs NW core viewed along the $\langle 1-10 \rangle$ zone axis (scale bar: $1 \mu\text{m}$). Higher magnification images of (b) the bottom, (c) intermediate and (d) top sections of the NW as indicated in (a). The insets in (b) and (d) show the selected-area electron diffraction (SAED) pattern taken from the encircled regions (scale bars: 100 nm).

The morphology of the grown NW arrays was examined in a Zeiss Merlin scanning electron microscope (SEM). For structural investigation, the as-grown NWs were transferred onto a carbon-coated Cu grids and studied in a FEI Talos TEM operated at 200 keV in high-resolution and high-angle annular dark-field scanning TEM (HAADF-STEM) modes. Elemental maps were obtained by energy-dispersive x-ray (EDX) spectroscopy. The optical properties of the NWs were studied by micro-photoluminescence ($\mu\text{-PL}$) in a cryostat operating at around 4 K under an optical excitation provided by the 632.8 nm line of He-Ne laser. The PL signal was collected into a 300 mm focal length spectrometer and dispersed by a 150 l/mm grating onto a Peltier-cooled CCD. Cathodoluminescence (CL) measurements on the NWs were carried out in an Attolight Rosa 4634 CL-SEM microscope. The measurements were carried out at 10 K with a beam energy of 5 keV and probe currents of 5-20 nA. The CL signal was collected into a 320 mm focal length spectrometer and dispersed by a 150 l/mm grating onto an IR-sensitive Peltier-cooled InGaAs PDA detector.

4.1.4 Results and Discussion

Figure 4.2 (a) shows a representative bright-field TEM micrograph of the GaAs core taken along the $\langle 1-10 \rangle$ zone axis. Higher magnification images of some of the specific regions along the length of the NW are shown in figures 4.2 (b)–(d). A selected-area electron diffraction (SAED) pattern from the encircled regions in figures 1(b) and (d) is provided as an inset which

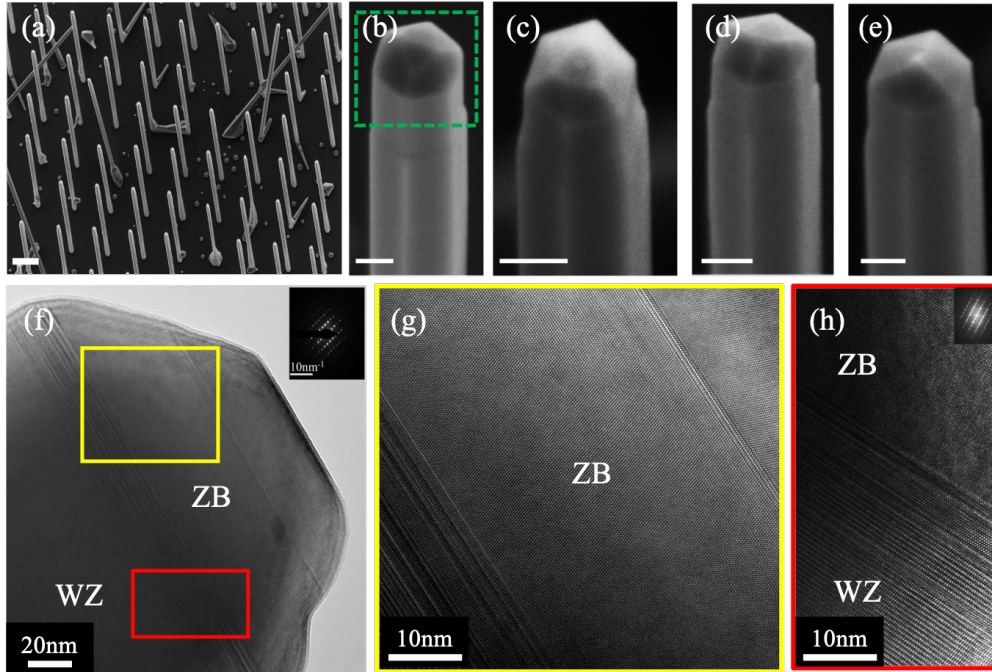


Figure 4.3 – SEM and TEM image showing morphology of the nanowire sample with droplet consumption at 630°C. (a) An overview of the NW array with 55 nm nanohole diameter and 2 μm pitch (inter-wire distance) (scale bar: 1 μm). (b)-(e) Magnified images of the resultant NW tip after the droplet consumption step (scale bars: 50 nm). (f)-(h) HR-TEM image of the NW tip taken along $\langle 1-10 \rangle$ zone axis. Insets in (f) and (h) show SAED patterns taken from the respective sections of the NW.

reveals the crystal structure of these sections of the NW. All the NWs showed a predominantly zincblende (ZB) phase at the bottom (figure 1(b)), followed by a transition region composed of a dense region of stacking faults (figure 4.2 (c)). Following the transition region, the upper segment of the NWs is pure wurtzite (WZ) as shown in figure 4.2 (d). The observed transitions in the crystal phase are due to the variation in the Ga droplet contact angle [73, 137, 140]. Variations in the droplet contact angle modify the capillary forces at the triple phase line (TPL) and control the formation of ZB and WZ phases [141]. Recent in-situ TEM growth experiments, have shown that ZB phase is favoured at small ($<100^\circ$) and large ($>125^\circ$) contact angles while WZ phase is favoured at any intermediate contact angle [4].

In the VLS growth of GaAs NWs, the Ga droplet acts as a non-stationary reservoir of Ga [97, 142]. The relative Ga flux during growth determines the droplet size and the contact angle. An As-rich growth condition shrinks the droplet and reduces the contact angle, whereas, a Ga-rich condition swells the droplet and increases the contact angle. Therefore, a predominantly ZB crystal structure at the bottom of the NW is due to Ga-rich conditions at the beginning of the growth. After reaching the desired length, the Ga flux is terminated, and the droplet is consumed under a constant As_4 flux. As the droplet shrinks, the contact angle also decreases gradually, creating a transition region full of stacking faults. When the contact angle falls below

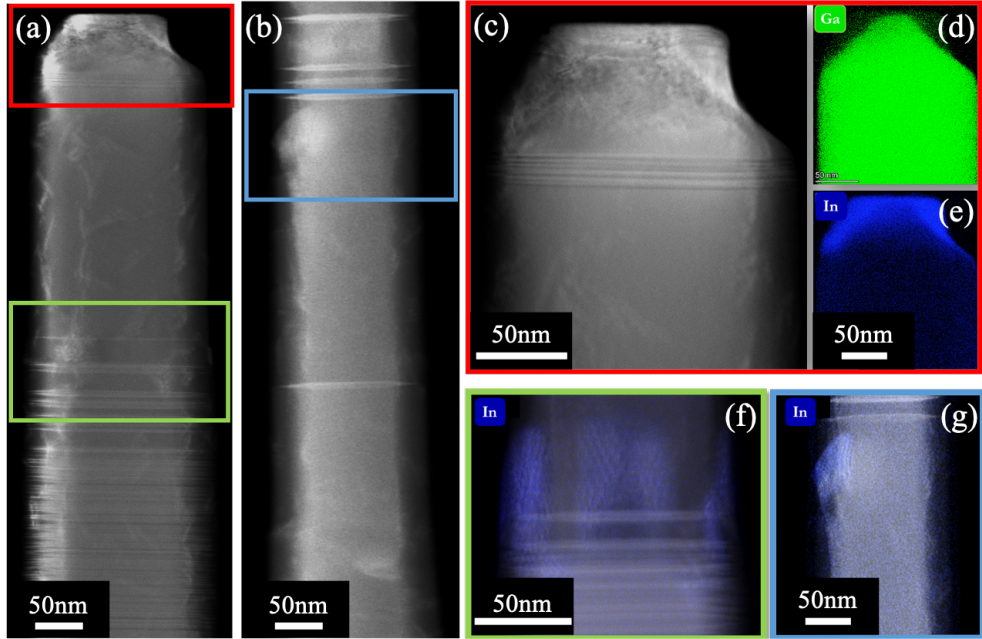


Figure 4.4 – HAADF-STEM image of the GaAs NW tip after 5 s of InAs deposition under a V/III ratio of 45 at 630°C. (a) HAADF image of the (a) upper (wurtzite) and (b) lower (zincblende) sections of the NW. (c) A magnified image of the NW tip and (d) and (e) simultaneous EDX elemental distributions of Ga and In, respectively. (f) and (g) HAADF-STEM images of two selected sections from the NW super imposed with the EDX map of In.

125°, the WZ phase becomes favourable, and the consumption of the remaining Ga droplet results in a pure WZ phase. Finally, at a very small droplet size, the NW tip is again ZB but has a different facet morphology (figure 4.3). For a core-shell NW heterostructure, defects in the NW core template into the shell [143]. Thus, GaAs NW core with a defect-free tip is essential for the growth of axial heterostructures. The SEM images of the NW tip after Ga droplet consumption at 630°C are shown in figures 4.3 (a)-(e). Figures 4.3 (f)-(h) show high-resolution TEM images of the NW tip taken along the $\langle 1-10 \rangle$ zone axis. The tilted facets are indexed by measuring the angles made with the $\langle -1-1-1 \rangle$ NW growth plane. The tip of the NW showed a pure ZB phase and is free of stacking faults (figure 4.3 (g) and (h)). However, non-uniformities in the NW tip morphology are observed. A major fraction of the NW tips observed in SEM showed a truncated pyramidal morphology with a flat triangular 111B facet at the tip as evident in figure 4.3 (b)-(d). The remaining fraction of NWs showed a completely pinched-off NW tip as shown in figure 4.3 (e). In crystal growth, facet formation is governed by the slowest growing plane. Any variation in the growth conditions (like V/III ratio or temperature) affects the growth rate of different planes and dictates the final facet morphology. Under the conditions studied here, we believe the group-III and group-V re-evaporation rates to be substantial and varying from one NW to another. Therefore, the observed non-uniformities in the tip morphology can be attributed to the local variation in growth conditions.

Formation of axial In(Ga)As clusters

Having obtained a good understanding of the GaAs NW tip morphology and crystal structure, the effect of InAs deposition on GaAs NWs was investigated. STEM measurements were performed to study the preferential accumulation of InAs on the NWs. Figure 3(a) shows the HAADF-STEM image of the upper region of the NW after InAs deposition. Due to the higher atomic number (Z) of In with respect to Ga, we attribute the regions with a brighter intensity to the presence of In(Ga)As clusters. These clusters are observed on the top facet (axial clusters) as well as along the NW side facets (radial clusters).

Figure 4.4 (c) shows a magnified HAADF image of the GaAs NW tip after InAs deposition as indicated by a red rectangular region in figure 4.4 (a). The corresponding In and Ga EDX maps are shown in figures 4.4 (d) and (e). In(Ga)As clusters accumulate at the tip of the NW whereas, pure InAs accumulation is observed on both the inclined top facets. When the amount of InAs deposited is reduced, the InAs clusters become even smaller and are observed only on one of the inclined facets at the NW tip (supplementary information A.1). We believe these smaller clusters on one of the inclined facets to be pure InAs based on the EDX maps of figures 4.4 (d) and (e). However, we note that it is unclear at this point if the InAs clusters on the inclined top facets accumulate on one of the NW top facets or at the corner facet formed by the intersection of two crystal planes. This NW tip faceting is clearly evident from SEM images in figures 4.3 (b)-(e). The InAs clusters accumulating on the corner facets at the tip are similar to the clusters nucleating at the corner facets on the NW sidewalls, as discussed in the next section. Further investigation is needed to determine the exact location of these clusters. This, however, shows that engineering of the NW top facet could help in obtaining axial InAs clusters.

Formation of radial In(Ga)As clusters

Self-catalysed GaAs NWs commonly exhibit a hexagonal cross-section consisting of $\{1-10\}$ type side facets connected by short $\{11-2\}$ corner facets [144]. Three-dimensional growth of InAs nanostructures on GaAs (110) surfaces is found to be energetically unfavourable [145–148].

The Stranski-Krastonov growth of three-dimensional InAs islands on these surfaces has been realized only after covering the facets with a thin layer of surfactant material [146, 149]. In our case, we observe the formation of three-dimensional In-rich clusters on GaAs NW side facets by depositing InAs layer at a higher substrate temperature. In HAADF images of figures 4.4 (a) and (b), which are taken along top and bottom parts of the NW, we observe regions with brighter contrast all along the NW sidewalls. This indicates the presence of radial In(Ga)As clusters along with axial clusters on GaAs NWs. This is also evident from the EDX elemental map of In overlapped with HAADF images of NW sidewalls in figures 4.4 (f) and (g). The location of the observed In-rich radial clusters in figure 4.4 (f) clearly suggests that they are nucleating on the edges separating the two $\{110\}$ NW side facets.

In the following discussion, we propose a material transport model to explain the temperature-

4.1. Facet-driven formation of axial and radial In(Ga)As clusters in GaAs nanowires

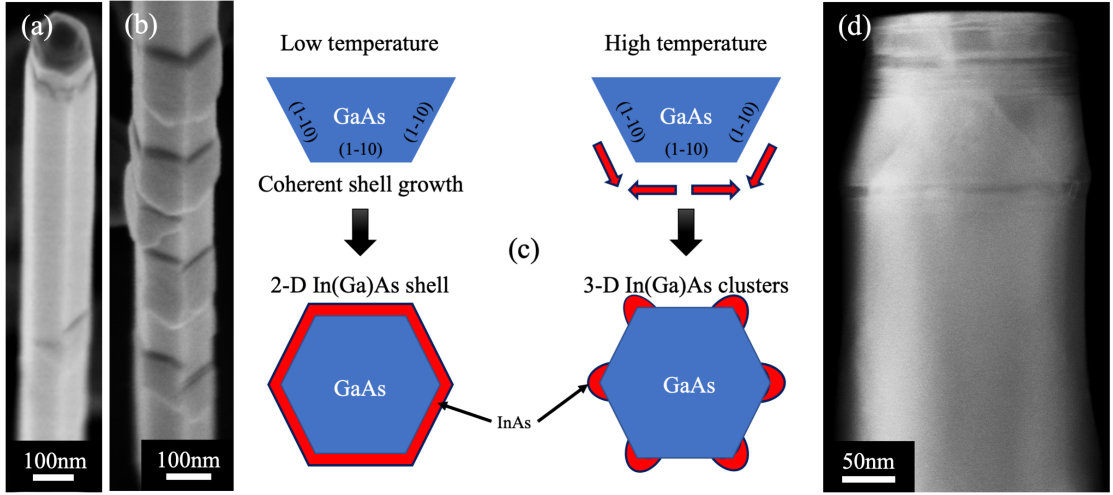


Figure 4.5 – (a) and (b) SEM images of a NW sample after InAs deposition at low temperature (440°C) for 5 mins. (c) Illustration of the proposed material transport mechanisms. The red arrow indicates the adatom diffusion driven by strain relaxation. (d) HAADF-STEM image of the tip of a NW taken from the sample after GaAs shell capping.

dependent formation of 3-D In(Ga)As clusters. We base our proposition on strain energy minimization. Strain energy minimization [150] and gradient in chemical potential [144] are the two known driving forces for adatom diffusion between different NW facets. The convex nature of the {11-2} corner facets makes them favourable sites for strain relaxation and the nucleation of 3-D structures [151]. At a higher substrate temperature, adatoms have enough kinetic energy to overcome the chemical potential barrier. Thus, material transport due to strain relaxation becomes dominant. This, in turn, promotes preferential accumulation of the impinging adatoms at the corner facets. This results in the formation of In-rich clusters along the {11-2} corner facets of the NW. A schematic of the proposed mechanism is shown in figure 4.5 (c). At higher temperatures, In(Ga)As clusters preferentially accumulate at the corner facets indicated by red arrows, as observed in figure 4.4 (f). In contrast, growth at a lower substrate temperature in the absence of a surfactant leads to the formation of a thin 2-D In(Ga)As shell [127]. Figure 4.5 (a) and (b) show SEM images of upper and lower regions, respectively, of a NW sample grown at a lower substrate temperature (440°C). The InAs deposition was carried out for 5 mins under an As_4 BEP of 5.6×10^{-6} Torr and a V/III ratio of 45. The formation of a thin discontinuous 2-D shell is observed. The lower diffusivity of In adatoms at this growth temperature leads to a high density of such clusters at the bottom of the NW (figure 4.5 (b)) whereas a lower density is seen in the upper part of the NW (figure 4.5 (a)).

Optical Characterization of the In(Ga)As clusters

To investigate the optical properties, CL and PL measurements were carried out on NW structures similar to the ones studied by STEM-EDX. However, to reduce the size of In(Ga)As clusters, InAs was deposited for 3 s under an In BEP of 2.2×10^{-8} Torr. The NWs were subsequently

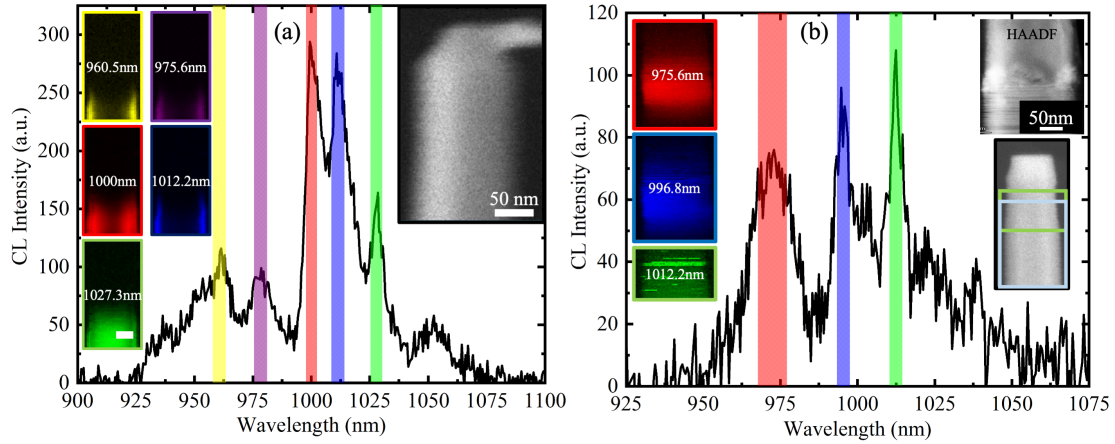


Figure 4.6 – Spatially-averaged CL spectra of two representative NWs from the sample after shell capping. The spectra correspond to the emission averaged over the region close to the NW tips. The left and right insets indicate energy-filtered CL emission maps and CL-SEM images of the NWs respectively. The inset on the top right in (b) corresponds to a HAADF image of the region indicated by the green box.

capped with a GaAs shell for confinement. The GaAs shell growth was carried out at a substrate temperature of 440°C and under a high V/III ratio of 70 to ensure growth of a conformal 2-D GaAs shell. Ga and As₄ BEPs were maintained at 1.4×10^{-7} and 1.0×10^{-5} Torr, respectively. Figure 4.5 (d) shows the HAADF image of a NW after shell capping. The tip of the NW showed a high density of defects upon capping with a GaAs shell. We also note that the HAADF contrast as seen in figure 4.4 from the In-rich clusters is not visible upon shell capping.

Figure 4.6 shows the CL spectra of two representative NWs from the sample after shell capping. The CL spectra correspond to the emission of a region close to the NW tip and are averaged through the region indicated in the SEM images in the insets. The insets on the left and the right show the energy-filtered CL maps and the SEM image of the NWs, respectively. The colour coding is mentioned on the respective energy-filtered CL maps in the insets. The spectra in figures 4.6 (a) and (b) both show multiple peaks originating from different emission zones. Some emission zones appear as a strip across the whole NW diameter (1.207 eV) while others extend over very few pixels (1.225 eV, 1.24 eV, 1.271 eV, 1.291 eV). In agreement with the structural characterization results (figure 4.4), all the emission zones observed in the CL maps are in close proximity to each other. The emission zones in the CL maps of figure 4.6 (a) are in agreement with the location of In(Ga)As clusters seen in figures 4.4 (f) and (g). Due to the high density of defects at the tip, no emission is observed from this region of the NWs. In figure 4.6 (b), the emission zones are near the stacking faults. This is evident from the emission map corresponding to 1.225 eV which indicates accumulation of In-rich clusters in the region with a high density of stacking faults. This is in agreement with the HAADF image in the inset of figure 4.6 (b) where regions with brighter contrast are seen in the region full of stacking faults.

Due to the carrier diffusion length and excitation volume, the exact location of each localized

4.1. Facet-driven formation of axial and radial In(Ga)As clusters in GaAs nanowires

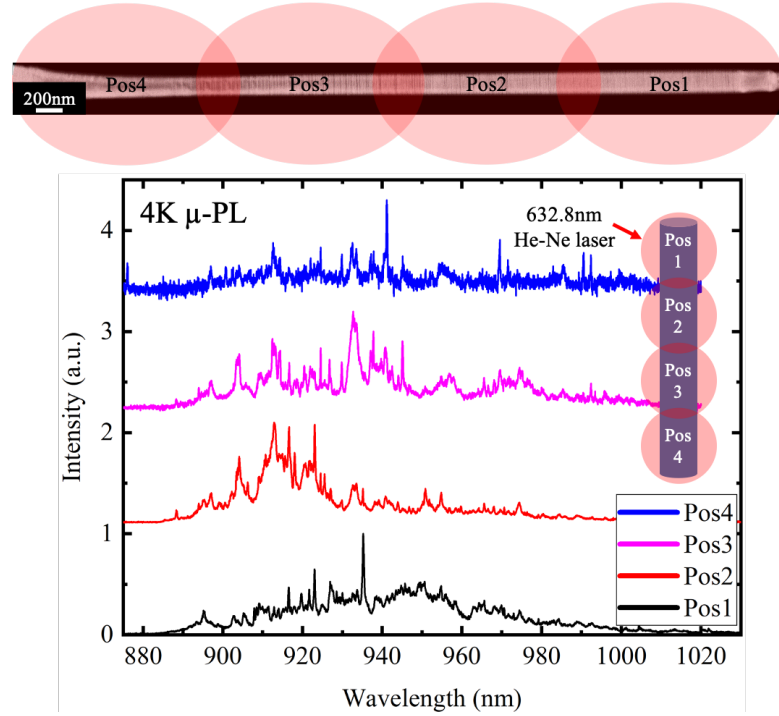


Figure 4.7 – Micro-PL spectra acquired at 4 K from a NW lying horizontally on the as-grown substrate. The spectra are acquired at four different illumination positions on the NW as shown in the inset. The sharp peaks are a clear indication of quantized energy levels in the In(Ga)As clusters on the NW sidewalls.

cluster is challenging to resolve. However, the occurrence of multiple emission peaks suggests the presence of In-rich clusters all along the NW sidewalls. To confirm the presence of very thin In-rich clusters along the NW sidewalls, position-dependent PL measurements were carried out as shown in figure 4.7. The PL spectra were acquired from a single NW lying horizontally on the as-grown substrate. The background emission from the underlying substrate was absent and ensures that the spectra shown here indeed originate purely from the NW heterostructure. The spectra acquired at very low excitation powers reveal sharp QD-like emission lines. The narrow peaks with linewidths in the sub-meV range indicate that the emission originates from the In(Ga)As clusters confined on the NW sidewalls.

4.1.5 Conclusion

In summary, we have studied the effect of NW growth termination on the morphology of the GaAs NW tips obtained in ordered arrays. Depending on the NW morphology and growth temperature we have demonstrated the formation of axial and radial In(Ga)As clusters. GaAs NW tips showed a truncated pyramidal morphology with a flat triangular {111}B facet at the top. Moreover, the tips are found to be free of stacking faults and have a pure ZB crystal structure. In addition, In(Ga)As clusters were obtained all along the corner facets of the NW

Chapter 4. Results and Discussion

sidewalls. The occurrence of radial In(Ga)As clusters was confirmed by scanning TEM and low-temperature CL and PL measurements. We believe that the In(Ga)As cluster formation is driven by the convex nature of the {11-2} corner facets. This approach of facet-driven nanostructure self-assembly can be engineered to grow axial and radial QDs in lattice-mismatched NW heterostructures. In addition, they could also be exploited to make novel quantum structures ranging from 3-D islands to zig-zag shaped nano-rings on NWs [148]. The QD-in-nanowires could potentially contribute to single photon emitter devices with large repetition rates owing to small radiative decay lifetimes [152]. Considering the shortest excitonic lifetime measured in QD-in-nanowire systems (0.42 ns) [153], repetition rates could in principle be as high as 2 GHz. However, this high emission rate is only achievable by optical excitation. Challenges currently reside in the electrical excitation of QD-in-nanowires. Nonetheless, with the availability of sophisticated manipulation and processing techniques, the integration of nanowire QD emitters into silicon photonics operating at telecom wavelengths approaches the possible [154].

Acknowledgements

This work is part of a project that has received funding from the European Union's Horizon 2020 research and innovation programme under the Marie Skłodowska-Curie grant agreement no. 765075, LIMQUET project. Authors thank also INDEED project from the H2020 program. The authors also acknowledge funding received from SNF through grants no. 40B2-0_176680, 200021_169908 as well as through the NCCR QSIT. A. B. and S. P. R. thank Simon Escobar for help with electron microscopy. M. N. and C. C. would like to thank Robert Taylor and Régis Deturche for their help on the μ -PL setup.

Supplementary Information

The supplementary information is provided in Appendix A.

4.2 On the origin of Raman peak splitting in monolayer 2-D materials-metal interfaces: MoS₂/Au

Mirjana Dimitrievska*, A. Balgarkashi*, Jin Jiang, Elias Z. Stutz, Mitali Banerjee, Anna Fontcuberta i Morral

*equal contribution

in review

This work is related to the second half of my PhD work. It resulted from an experiment to obtain larger sized monolayer MoS₂ flakes by exfoliation on gold substrates. We usually exfoliated TMD flakes on 285 nm SiO₂/Si substrates and the monolayer flakes obtained were typically <20 μm in size. Recent studies have demonstrated that monolayer flakes with sizes of hundreds of micrometers can be obtained by exfoliation on gold substrates [155]. Therefore, we started to exfoliate on 7nm gold films which were deposited on SiO₂/Si substrates to obtain larger MoS₂ monolayers.

Raman spectroscopy is routinely used to identify monolayer flakes. The Raman spectrum of MoS₂ consists of two dominant Raman modes which are assigned to the in-plane vibration of Mo and S atoms (E_{2g}^1) and out-of-plane vibrations of the S atoms (A_{1g}). A frequency difference of 19 cm⁻¹ between the E_{2g}^1 and A_{1g} Raman modes in MoS₂ constitutes the signature of a monolayer. While verifying MoS₂ monolayers on gold substrates, we observed a peak splitting in the Raman spectra for both the E_{2g}^1 and A_{1g} peaks. The following work is the result of our attempt at understanding the microscopic origins behind the Raman peak splitting.

To investigate further, we decided to exfoliate MoS₂ monolayers also on gold films with different thicknesses of 2 nm and 4 nm. Monolayer exfoliated on standard SiO₂/Si substrate was used as a reference. We could observe a peak splitting in all three MoS₂ on gold samples. Comparing our results with similar studies found in the literature, we realized that the splitting remains identical irrespective of the thickness of gold film beneath or the sample configuration. Here, sample configuration refers to:

- (a) the monolayer exfoliated on top of the gold substrate, or
- (b) a thin gold film deposited on top of the monolayer, or
- (c) the monolayer being sandwiched between thin films of gold.

An identical peak splitting in all the cases led us to believe that the peak splitting phenomenon is universal to the MoS₂-gold interface. The commonly suggested notions to explain peak splitting are strain and or a change in carrier concentration (doping). Although one can explain the peak splitting for the E_{2g}^1 (strain) and A_{1g} (doping) individually, an explanation for simultaneous splitting of both the peaks based on either strain or doping is unsatisfactory. We also estimated the values of strain and carrier concentration based on the positions of

additional peaks observed in the Raman spectra. These were found to be relatively high for the MoS₂/Au system under consideration. Therefore, we considered a third notion based on the breaking of Raman selection rules to explain our experimental observations.

In a first-order Raman scattering process, only phonons modes around the Γ -point ($q \simeq 0$) can be observed owing to conservation of momentum. In the presence of defects, an additional momentum can be provided by scattering from the defects and the momentum conservation rule is relaxed. In our samples, we attribute this to the interaction between Au and S which might structural perturbations in the MoS₂. This can then relax the Raman selection rules. This leads to the activation of phonon modes away from the Brillouin zone edge ($q \neq 0$). We compared the positions of the split peaks observed in the Raman spectrum of MoS₂ on gold samples with the phonon dispersions in monolayer MoS₂. The positions of new peaks match well with the phonon frequencies around K-point of the Brillouin zone.

Another interesting observation was that the intensity of the split peaks is comparable to the main E_{2g}¹ and A_{1g} peaks. Considering only intrinsic defects in our samples, this is unlikely. This pointed us towards an additional contribution in our samples based on gold plasmon-MoS₂ phonon interaction. We used PL spectroscopy to verify this. The gold substrates exhibited a plasmonic broadband in PL around 570 nm, which are highly likely to be excited by the 532 nm laser used for excitation. We argue how this can give rise to peak splitting as well as an enhancement in the intensity. The plasmonic effect of gold substrates was further justified by transferring an MoS₂ monolayer on an Al substrate, which did not show any Raman peak splitting.

My contribution to this work involved preparation of all the samples and performing all the optical measurements. I also took part in the discussion and analysis of the results, preparation of the figures and writing of the manuscript.

4.2.1 Abstract

Semiconductor-metal junctions are at the base of any electronic or optoelectronic device. Microscopic understanding is essential to engineer their functionality. Raman scattering is sensitive to strain, defects, carrier concentration and plasmon interactions. We provide an exhaustive analysis of the MoS₂/Au junction by Raman and photoluminescence spectroscopy. We observe that two main phonon modes split and slightly shift when in contact with Au, while they remain unperturbed when Al is used. This change is amplified when the MoS₂ is sandwiched between two Au layers. Our study elucidates the role of Au atoms interactions with MoS₂, leading to local structural perturbations as well as the contribution of plasmons in breaking Raman selection rules. This work provides a path for understanding of the junction between two-dimensional materials and metal electrodes.

4.2.2 Introduction

Two-dimensional (2-D) van der Waals materials have attracted major interest in the past decade due to their exceptional high degree of functionality combined with relatively facile fabrication techniques. Their wide range of capabilities is illustrated by the ample spectrum of material types ranging from insulators, semimetals, semiconductors to superconductors [156]. Monolayer (ML) transition-metal dichalcogenides (TMDs) exhibit a direct bandgap and a relatively high carrier mobility. They are thus excellent building blocks for applications in optoelectronics [157–159], photovoltaics and catalysis [160].

Electronic and optoelectronic applications with TMDs rely on the good functioning of the junction with metals. While the van der Waals nature of TMDs should in principle imply absence of states in the middle of the TMD bandgap, vacancies and point defects in the material may result in atom exchange and thus doping of the TMD by the metal. Chemical interaction at the interface, such as creation of metal-chalcogenide bonds, could lead to a configurational change in the TMD [161]. In addition, ML TMDs can be easily perturbed by strain or charge transfer from the underlying layers due to their ultra-thin nature [126]. Similar to classical low-dimensional structures, the physics of the metal-semiconductor junction shall dictate the behaviour of the device [162–164]. A fundamental understanding of the metal-TMD junction is thus extremely relevant for the reliability of TMD-based electronics and/or optoelectronics.

Raman spectroscopy is an optical non-destructive technique commonly used to characterize the structure and polarizability of materials [165]. In the context of 2-D materials, Raman spectroscopy is most commonly used to quantify the number of layers [166–168], effects of strain [169], doping [170] and defects [171]. In the case of monolayer TMDs, Raman spectra consist of in-plane (E_{2g}^1) and out-of-plane (A_{1g}) Raman active modes [172]. Among the recent Raman studies on TMD-metal interfaces, many have reported peak splitting of the A_{1g} and E_{2g} modes [11–15, 173, 174]. A variety of attempts have been made to explain the peak splitting, usually in terms of strain and charge transfer effects. However, information on the detailed nature of the ML TMD-metal interaction that leads to this splitting is still missing. To better understand the interaction at ML TMD-metal interfaces, extremely important for device performance, it is necessary to provide a full explanation of the mechanism causing the Raman peak splitting that occurs in this case.

In this work, we look into the origin of A_{1g} and E_{2g} peak splitting through a systematic measurement and analysis of Raman spectra, along with relevant literature review. We focus on MoS₂/Au as a representative system. We investigate in which cases strain and charge transfer could lead to the simultaneous splitting of both A_{1g} and E_{2g} Raman peaks. We explore a mechanism based on plasmon-phonon interaction and presence of structural perturbations at the TMD-metal interface as the main driver leading to peak splitting. We attribute the new peaks to non- Γ phonon modes originating from in-plane (E_{2g}) and out-of-plane (A_{1g}) phonon branches at certain non-zero wave vector. We test the validity of our hypothesis by

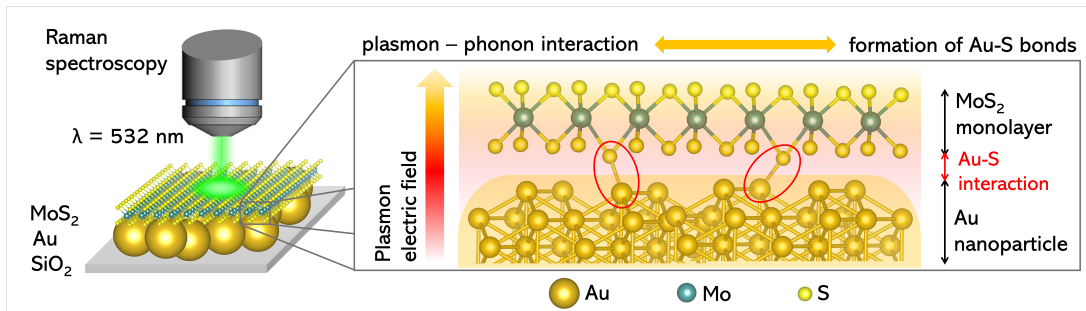


Figure 4.8 – **Raman setup configuration.** Schematic illustration (left) of the configuration used for Raman spectroscopy in back-scattering mode showing a monolayer of MoS₂ on gold nanoparticles. The inset on the right shows the chemical interaction between S atoms of MoS₂ and Au responsible for the plasmon-phonon interaction.

investigating samples with different interface configurations, including the exchange of Au with Al.

4.2.3 Experimental Results

Two sets of samples have been prepared: reference ML MoS₂ and ML MoS₂/Au with varying thickness of Au. Raman spectroscopy characterization of the samples is performed in reflection mode; more details can be found in the methods section. Figure 4.8 shows the configuration used for this study.

Reference samples were made by transferring MoS₂ flakes on the oxidized silicon substrates. Figure 4.9(a) shows an optical micrograph of one of these flakes. The change in contrast is associated to a varying number of monolayers. We indicate the region with one monolayer, ML. Other flakes were deposited on an oxidized substrate, which had been previously coated with gold with thicknesses of 2, 4 and 7 nm and average lateral particle size of 10-15 nm (figure B.3 in the Supplementary Information). Figures 4.9(b)-(d) show optical microscopy images of ML MoS₂ on a 2, 4 and 7 nm thick Au, respectively. The ML thickness of the reference MoS₂ sample was verified using the optical contrast as well as the characteristics of the Raman spectrum. The modes of ML MoS₂ are observed around 385 cm⁻¹ and 403 cm⁻¹ and are labeled as E_{2g} and A_{1g}, respectively. A frequency difference of 19 cm⁻¹ between the in-plane E_{2g} and out-of-plane A_{1g} Raman peaks constitutes the signature of a single ML [6]. On the gold substrates, the MoS₂ thickness was verified using optical contrast and atomic force microscopy profiling (for details see Supplementary Information figure B.2). Throughout the manuscript, we compare the properties of the ML MoS₂ transferred on the oxidized silicon substrate (reference) with respect to those transferred on Au. Figures 4.9(e) and (f) show respectively the Raman and photoluminescence (PL) spectra of the ML region of the samples shown in figures 4.9(a)-(d).

We start by comparing the Raman spectra of the ML MoS₂ on gold with respect to the reference. The notable feature from ML MoS₂ on gold is that both the E_{2g} and the A_{1g} modes split into

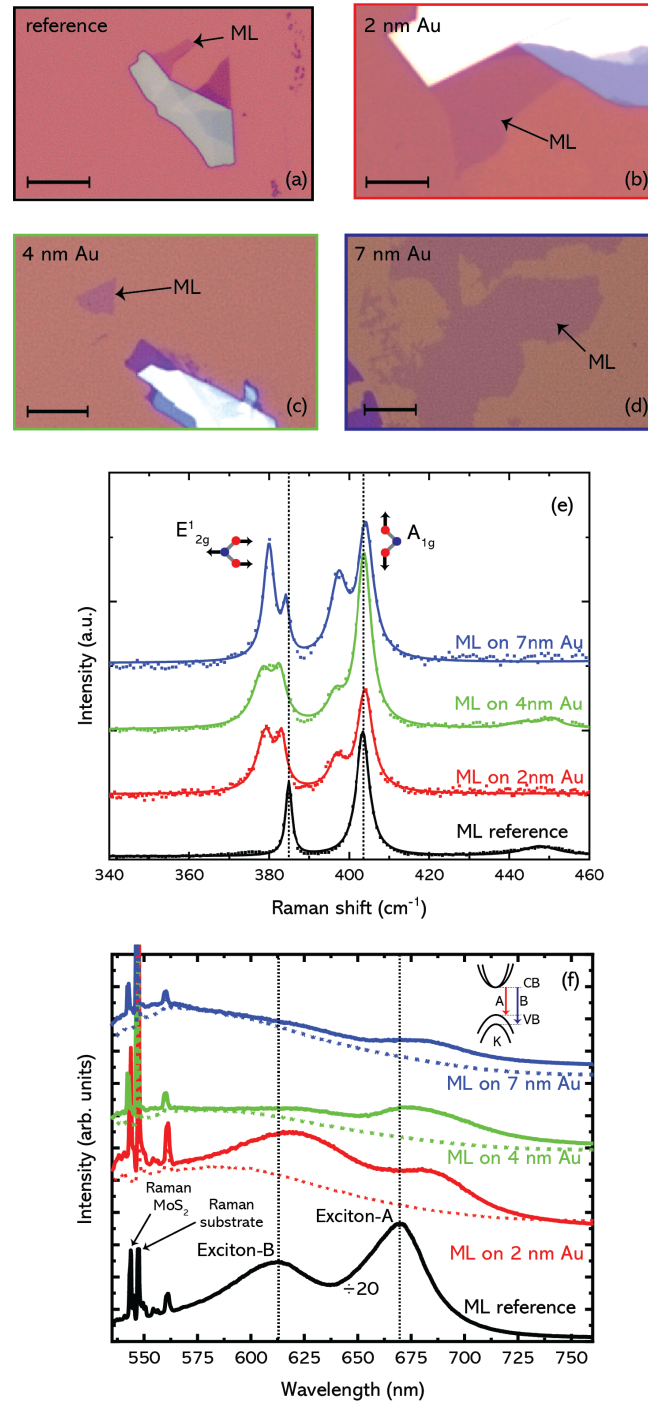


Figure 4.9 – **Characterization of MoS₂ monolayers on Au.** Optical micrographs of ML MoS₂ on (a) 285 nm SiO₂/Si substrate (reference sample) and (b)-(d) on 2, 4 and 7 nm gold deposited on the identical oxidized silicon substrate. Scale bars: 5 μm (e) Raman and (f) photoluminescence (PL) spectra from the MoS₂ reference, and the MoS₂ on 2, 4 and 7 nm gold respectively. The intensity of the Raman spectra has been normalized to the E'_{2g} peak. The dashed curves in (f) show the PL spectra from bare gold substrates.

two clearly distinct peaks. For the E_{2g} peak, this corresponds to a redshift of $\sim 1\text{-}2\text{ cm}^{-1}$ with respect to the reference. The position of the A_{1g} peak coincides with the reference. In addition, each mode splits into an additional peak E_{2g}' and A_{1g}' , down-shifted by a few cm^{-1} from the fundamental modes E_{2g} and A_{1g} . In all prepared samples of MoS_2 on gold, the peak splitting was observed solely in the single ML MoS_2 regions. We deduce this could be used for the fast identification of ML MoS_2 on gold (Supplementary figure B.2).

Figure 4.9(f) compares the PL response. The spectrum of the reference sample exhibits two broad bands centered around 610 and 662 nm, that can be attributed to the so-called A and B excitons [168]. Around 550 nm we observe very sharp peaks, that correspond to the Raman response of the MoS_2 and the substrate. The PL response of the MoS_2 on gold is reduced by the interaction with the underlying metal. For reference, we plot in discontinuous lines the separate PL response of Au, which dominates the PL background of the MoS_2 . In addition, we note that the intensity of the A and B excitons decreases progressively with the increase in the Au thickness. This quenching of PL intensity is unexpected as Au nanoparticles are known for their ability to enhance materials' response due to plasmonic characteristics [175, 176]. Currently, there is no consensus on how Au nanoparticles affect the PL response of MoS_2 , as some studies have reported enhancement of the PL intensity [176–178], while others have reported quenching [179–182]. In our case, we attribute the quenching to the Förster resonance energy transfer process (FRET) from the TMD to the metal [183]. This assumption is based on the fact that the emission energies of MoS_2 and the surface plasmon of Au nanoparticles are very close (Figure 2(f)).

We now focus on a more detailed analysis of the peak splitting in the Raman spectra. We define the Raman peak splitting as a difference in frequency of the fundamental and the newly appeared modes, i.e., $\Delta E_{2g} = E_{2g} - E_{2g}'$ and $\Delta A_{1g} = A_{1g} - A_{1g}'$. Figure 4.10 collects the ΔE_{2g} and ΔA_{1g} Raman peak splitting as a function of the gold thickness both from this work and literature. This graph clearly illustrates that, within the measurement error bar, the splitting is independent of thickness of the underlying Au [13–15]. The splitting is also independent whether the Au is above or below the ML MoS_2 [11–15, 174]. A similar behavior, although a different size of splitting, was observed for MoS_2 on Ag [184]. This suggests that the splitting constitutes a general feature, characteristic of the metal- MoS_2 interaction.

4.2.4 Discussion

We now turn to the discussion on the various interpretations that have been proposed to account for the appearance of the two new Raman peaks (E_{2g}' and A_{1g}'). We shall evaluate these hypotheses on a case-by-case basis here below.

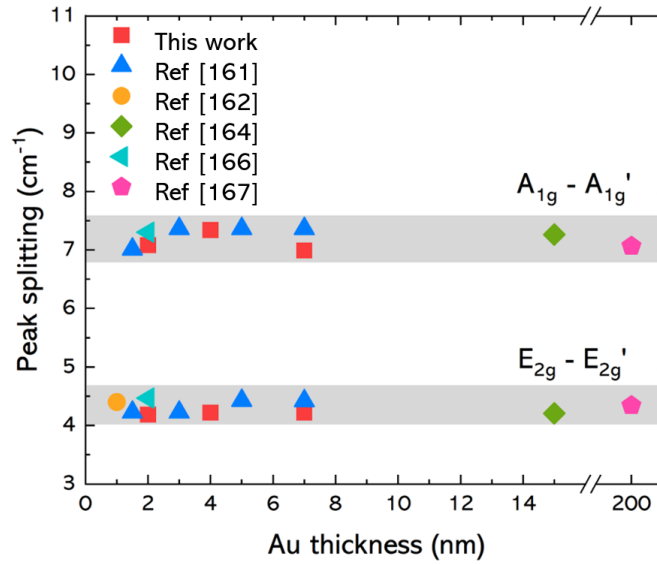


Figure 4.10 – **Peak splitting: literature vs. current work.** Comparison of peak splitting for A_{1g} and E_{2g} modes caused by the interaction of MoS₂ monolayers with Au nanoparticles from various studies and current work. The peak splitting for both the Raman modes remains nearly constant for gold thicknesses up to 200 nm [11–15].

Hypothesis I: Strain

Mechanical strain is often translated into peak shifts in the Raman spectra. When the deformation is anisotropic (e.g. shear strain), peak splitting can also occur [185, 186]. The effects of strain in TMDs like MoS₂ have been intensively studied in refs. [7, 16, 108, 186, 187]. The correlation between the shift and the strain has been clearly established. Figure 4.11(a) presents the evolution of A_{1g} and E_{2g} peak splitting with applied uniaxial and biaxial mechanical strain from two representative studies refs. [7] and [16], respectively. In case of ref. [7] uniaxial strain is applied by controllable bending of the exfoliated MoS₂ film in a four-point bending apparatus. The strain is then calculated as ratio of the thickness of the substrate (which is a constant value) and the radius of curvature. The authors have observed peak splitting of the E_{2g} mode into two distinct peaks (E_{2g} and E_{2g}'). They found that E_{2g} and E_{2g}' peaks shift by $1.0 \pm 1 \text{ cm}^{-1}/\%$ and $4.5 \pm 0.3 \text{ cm}^{-1}/\%$ strain for monolayer devices, which is consistent with their first-principle calculations. No changes in peak position of A_{1g} mode was observed, which is expected due to the nature of the applied strain along only the a-crystal axis. On the other hand, for applied biaxial strain on MoS₂ monolayers as reported in ref. [16], changes in both A_{1g} and E_{2g} peak positions have been observed, but with no peak splitting. In this case, the biaxial strain is induced by applying a pressure difference across an MoS₂ membrane suspended over a cylindrical cavity. Authors found that the modes shifted linearly at a rate of $-1.7 \text{ cm}^{-1}/\%$ for the A_{1g} and $-5.2 \text{ cm}^{-1}/\%$ for the E_{2g}, which agreed well with their theoretical predictions. We have used these two representative studies to calculate the difference in peak positions for A_{1g} and E_{2g} modes and estimate the induced strain in the case of our ML MoS₂/Au systems (Figure 4.11(a). From ref. [7], the peak splitting was calculated as (E_{2g}' -

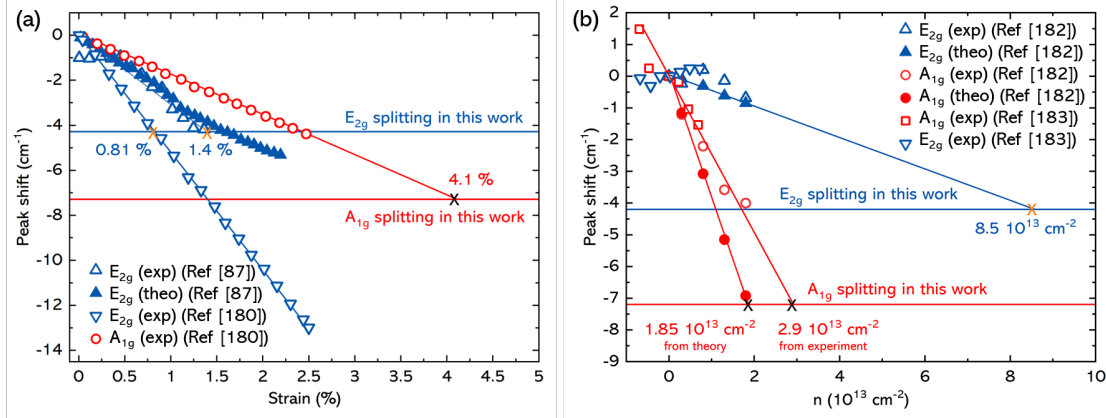


Figure 4.11 – **Raman peak shift and splitting.** A_{1g} and E_{2g} peak shift and splitting predicted and observed as a function of (a) strain (uniaxial [7] and biaxial [16]) and (b) electron density [17], [18].

E_{2g}), while from ref. [16], the peak splitting was calculated as (405 cm⁻¹ - A_{1g}) and (385 cm⁻¹ - E_{2g}), where the values of 405 and 385 cm⁻¹ correspond to A_{1g} and E_{2g} peak positions of the unstrained MoS₂ monolayer. This has led to estimation of the induced strain of 1.4 % from ref. [7], and 0.8 and 4.1 % from ref. [16]. These estimations correspond to relatively high values of strain that is induced only by Au nanoparticles, signaling that this might not be the true origin of the peak splitting.

Next, we can consider spatially heterogeneous deformation. It has been shown that TMDs undergo deformation when transferred on a non-planar substrate. As an example, WSe₂ and WS₂ suspended on a Si nanopillar array exhibit strong deformation at the nanopillar tips, resulting in localized single photon emission [34, 116]. In this sense, it has been argued that ML MoS₂ on gold nanoparticles should be mechanically deformed at the nanoscale [188]. The deformation in MoS₂ due to the gold nanoparticles in this work and SiO₂ nanopillars in ref. [20] was calculated from the AFM and TEM scans, respectively and is shown in Supplementary figure B.5. The deformation in MoS₂ on gold was found to be negligible when compared to SiO₂ nanopillars. Furthermore, the shift of Raman peaks observed in the case of nanopillars is found to be smaller than in the case of MoS₂ on gold. Thus, it is unlikely that the mechanical deformation at the nanoscale leads to the observed peak splitting in monolayer MoS₂ on gold, as seen in this work.

Recent work by Pető et al. [189] showed the appearance of MoS₂ nanobubbles on gold. They use nanoscale-resolved Raman spectroscopy to study two types of regions on their MoS₂ monolayers: flat regions, which they consider as reference, and nanobubbles. Raman spectra on flat regions of MoS₂ on gold shows typical peak splitting as observed in this work. On the other hand, Raman spectra on nanobubbles showed significant shifts (>10 cm⁻¹) and shape change of the E_{2g} mode. This shift in the E_{2g} mode has been attributed to a substantial amount of tensile strain that occurs on nanobubbles. Considering that Raman peak splitting

is observed on flat regions of MoS₂ on gold, where no significant strain is expected, can be taken as a further proof that this kind of splitting is probably not strain related.

This interpretation is further consistent with the study of Schauble et. al. [14] where a more clear-cut strain characterization using grazing incidence X-ray diffraction (GIXRD) was carried out. This technique reports directly on the lattice spacing in the material. In difference, while Raman spectroscopy does report on material strain, its identification is not univocal as shifts may arise by multiple factors. GIXRD measurements on ML MoS₂ on a variety of metal nanoparticles including Ni, Al, Au and Ag were performed [14]. These results demonstrated that Metal-MoS₂ pairs which exhibit Raman shift did not show any measurable strain in the GIXRD patterns. They attributed the Raman shift to exciton-plasmon coupling.

Hypothesis 2: Change in the carrier concentration

Raman spectroscopy is also sensitive to carrier density in the material via electron (hole)-phonon coupling [165]. Charge carrier exchange may occur when two materials with different Fermi energy levels are put in contact. Reported work function values in MoS₂ vary between 4.5 and 5.2 - 5.4 eV [190]. Given the values for Au (5.1 - 5.5 eV, nominal) [191], a charge carrier transfer might be expected upon their junction [163]. DFT calculations and optoelectronic characterization of monolayer MoS₂/Au systems show a reduction of the gap size, the presence of low-density in-gap states, and a shift of the conduction band minimum to lower energy [192–196].

The presence of free carriers affects lattice vibrations in TMDs by electrostatic screening and/or Fröhlich interaction [197, 198]. We start by considering the effect of electrostatic screening on the phonon modes. According to the Born-Oppenheimer approximation [199–201], phonons can be considered as static perturbations acting on the electrons. In ML TMDs, the out-of-plane ionic displacements involved in the A_{1g} mode imply a charge imbalance and in turn, an electrostatic potential. Free carriers react by partially screening this potential, resulting in the softening of the phonon modes. In general, the screening of the electron-phonon interaction results in the softening (downshift) of the vibrational modes. This occurs prominently for phonons strongly coupled to the electronic states at the Fermi surface, which is the case of the A_{1g} Raman mode. It has been shown in ML-TMDs that electrons are efficient in screening the interaction, while holes are ineffective in softening the modes [198].

Figure 4.11(b) shows the dependence of A_{1g} and E_{2g} mode frequencies on carrier concentration (n) obtained by two representative studies [17, 18]. Both works show a very similar trend. For an electron concentration of $1.8 \times 10^{13} \text{ cm}^{-2}$, the A_{1g} mode frequency softens by 4 cm^{-1} (from experiments) or 7 cm^{-1} (from first principle calculations), as compared to only $\sim 0.6 \text{ cm}^{-1}$ for the E_{2g} mode (from both experiments and calculations). This points out that the E_{2g} mode is much less sensitive to the electron density, in contrast to the A_{1g} mode [17, 198, 201].

One can estimate carrier concentrations for MoS₂/Au systems based on the studies cited

above. The observed peak splitting of the A_{1g} and E_{2g} modes in MoS_2/Au system leads to the extrapolated values of charge carrier concentrations of 2.9 and $8.5 \times 10^{13} \text{ cm}^{-2}$, respectively. In contrast, the theoretical results estimate slightly lower charge carrier concentrations of $1.85 \times 10^{13} \text{ cm}^{-2}$ based on the same value of peak splitting for the A_{1g} mode. These estimated electron densities are extremely high for MoS_2/Au systems. We conclude that while the shift of the A_{1g} mode may be due to a change in electron density, neither its splitting, nor the shift of the E_{2g} mode should be attributed solely to this effect.

Still, in case of the in-plane E_{2g} mode, the interaction with carriers occurs through the long range Fröhlich potential with the longitudinal component of the E_{2g} optical phonon. It has been shown that in MoS_2 , the electron-phonon Fröhlich interaction can be enhanced by the presence of impurities that break the momentum conservation rule [197]. There is a range of electron concentrations in which the Fröhlich interaction becomes relevant in TMDs. Eventually, the excitation of plasmons right below the MoS_2 could excite the Fröhlich interaction. More details on the effect of plasmonic interaction are further elaborated below.

Hypothesis 3: Simultaneous effect of strain and charge transfer in ML MoS_2/Au system

While it is clear that single effect of strain or charge transfer is not likely the cause of peak splitting, we should also consider the possibility of a simultaneous effect of both strain and charge transfer. Using this assumption, Velicky et al. [15] have reported a detailed study on the nature of the MoS_2/Au interaction and its evolution with the MoS_2 thickness. Using tip-enhanced Raman spectroscopy and X-ray photoelectron spectroscopy, they have proposed heterogeneous MoS_2/Au interaction at the nanoscale, which consists of strongly interacting regions of MoS_2 with Au, and suspended MoS_2 . They have assigned the downshift and broadening of the E_{2g} mode to the heterogeneous biaxial tensile strains of up to 1.9%. Furthermore, the splitting of the A_{1g} mode is explained by a portion of MoS_2 being in close contact with the Au, which experiences n-type charge doping with electron concentrations up to $2.6 \times 10^{13} \text{ cm}^{-2}$, while another portion is suspended and undoped. This is very similar to the estimated value of charge doping based on our experiments, as stated in the previous section. One problem about these assumptions arises from the fact that recent DFT calculations on MoS_2/Au systems [202] do not agree with such high values of charge transfer, even locally at the nanoscale, and suggest much smaller values (-15.6 millielectrons per MoS_2 formula unit).

Hypothesis 4: Symmetry breaking in ML MoS_2 due to interaction with Au

We now explore the hypothesis of breaking of Raman selection rules as a path to activation of modes outside the Γ -point of the phonon dispersion and possible explanation of the peak splitting. There are several factors leading to activation of the non- Γ phonons: (i) intrinsic defects and disorder [203]; (ii) extrinsic defects formed by the impurities in the material, or at the interface between two materials [204–208]; and (iii) photonic and plasmonic interactions with nanoscale materials [209, 210]. All these factors create local perturbations in the material,

either in the form of structural changes which break the translational symmetry ((i) and (ii)), or strong enhancement of the electrical field (iii). These perturbations allow absorption of the additional phonon momentum, which breaks the phonon momentum conservation rule, leading to activation of the phonon modes away from the Brillouin zone center.

In our MoS₂/Au systems, intrinsic defects and disorder are not expected to be the main cause of the peak splitting. All MoS₂ monolayers were prepared identically. All samples should exhibit a similar number of intrinsic defects. Still, extrinsic defects resulting from the interaction of Au and S atoms at the MoS₂/Au interface, as well as the phonon-plasmon interaction are not present in reference MoS₂ monolayers. We argue that these processes might cause the observed Raman peak splitting of A_{1g} and E_{2g} modes.

The Au-S covalent bond is regularly used as an anchor to order self-assembled organic molecules due to the strong Au-S electronic interaction [211, 212]. Recently though, it has been suggested that the Au-S interaction at the Au/MoS₂ interface exhibits a non-covalent character [202]. This is manifested by a S(MoS₂)-Au interfacial distance of 2.53 Å, which largely exceeds the covalent S-Au bonds, spanning from 2.16 Å in the AuS molecule [213] to 2.2 - 2.3 Å for thiols covalently bound to Au [214].

Still, the strong interaction between Au and S atoms modifies the Mo-S bond at the interface with Au, compared to the Mo-S bond facing the air. Experiments and DFT calculations performed on MoS₂/Au systems indicate band structure changes induced by the Au-S interaction [195, 215–217]. Furthermore, cross-sectional transmission electron microscopy studies of ML MoS₂ on gold thin films have shown that the distance between the bottom S and Mo layer extends due to interaction with gold while the distance between top S layer and Mo remains mostly unchanged [194, 196]. These changes in the bond lengths, necessarily imply a modification of the phonons.

Extension of the Mo-S bond due to the interaction with Au, creates a local structural perturbation in MoS₂ lattice, which acts similar to a defect. These perturbations cause phonon confinement. Based on the phonon dispersions of the E_{2g} and A_{1g} modes [203, 218, 219] this should cause a downward and a very slight upward shift of E_{2g} and A_{1g} peaks, respectively. Broadening of peaks is expected due to the reduction in the phonon lifetime. This is consistent with the measured Raman spectra of MoS₂/Au structures (Figure 4.9), where a downshift of the E_{2g} (~2 cm⁻¹) and a very small upshift of the A_{1g} (<0.5 cm⁻¹) is present when compared to reference MoS₂. Broadening of both peaks is also observed. This observed behavior is also in good agreement with the results of previous experimental and computational studies [203–208].

Besides the shift and broadening of the main E_{2g} and A_{1g} peaks, structural perturbations can also lead to activation of forbidden modes. Considering that the newly emerged A_{1g}' and E_{2g}' peaks in figure 4.9 have the same polarization dependence as the main E_{2g} and A_{1g} peaks (experimentally confirmed by polarization Raman measurements shown in Supplementary Information figures B.7 and B.8), it is most likely that they originate from in-plane (E_{2g}) and

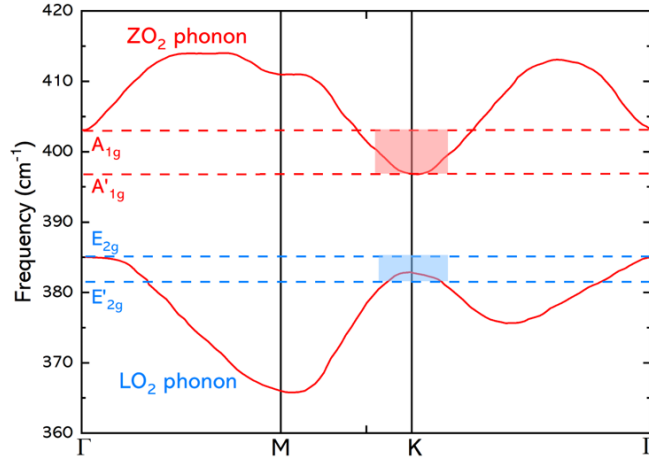


Figure 4.12 – **Phonon dispersions of MoS₂ monolayers.** Phonon dispersions of the in-plane (LO₂) and out-of-plane (ZO₂) phonons in monolayer MoS₂ obtained from ref. [19], and corresponding to E_{2g} and A_{1g} modes at the Γ -point, respectively. The lines show the positions of A_{1g} and A_{1g}' peaks (red); and E_{2g} and E_{2g}' peak (blue), observed from Raman spectra of MoS₂ on gold thin films in this work. The red and blue rectangles indicate the positions in the Brillouin zone from where the A_{1g}' and E_{2g}' peaks probably originate, which is around the K-point.

out-of-plane (A_{1g}) phonon branches at certain non-zero wave vector q .

Looking closely at the phonon dispersion of MoS₂ monolayers reported in ref [19], it is evident that the new peaks probably originate from phonons around the K-point in the Brillouin zone (figure 4.12). Further confirmation of these claims also comes from literature, where similar peak splitting of the E_{2g} mode has been observed in MoS₂ upon ion-irradiation [204, 206–208]. In this case, the inclusion of local disorder induces the symmetry breaking and appearance of additional E_{2g} modes coinciding with the branch at the K-point [219].

While appearance of A_{1g}' and E_{2g}' modes in the Raman spectra of MoS₂/Au could be explained by the activation of the non- Γ phonons due to interaction between Au and S atoms, one would expect their intensities to be an order of magnitude lower than intensities of the A_{1g} and E_{2g} modes. This is not consistent with the experimental Raman results, where both A_{1g}' and E_{2g}' modes show very prominent intensities. This points to an additional process occurring between MoS₂ and Au, primarily focused on the enhancement of Raman intensities.

Here, we evaluate the interaction between the MoS₂ phonons with the surface plasmons of Au. Our Au nanoparticles exhibit a plasmonic broadband around 570 nm, as shown in Fig. 4.9(f). Upon the light excitation of Au, surface plasmons are excited, creating strong local electric fields. These field enhancements are greatest when the plasmon energy is close to the energy of light excitation, which is the case in our Raman measurements with 532 nm laser. Strong local electric fields could result in the relaxation of the momentum conservation rule in the

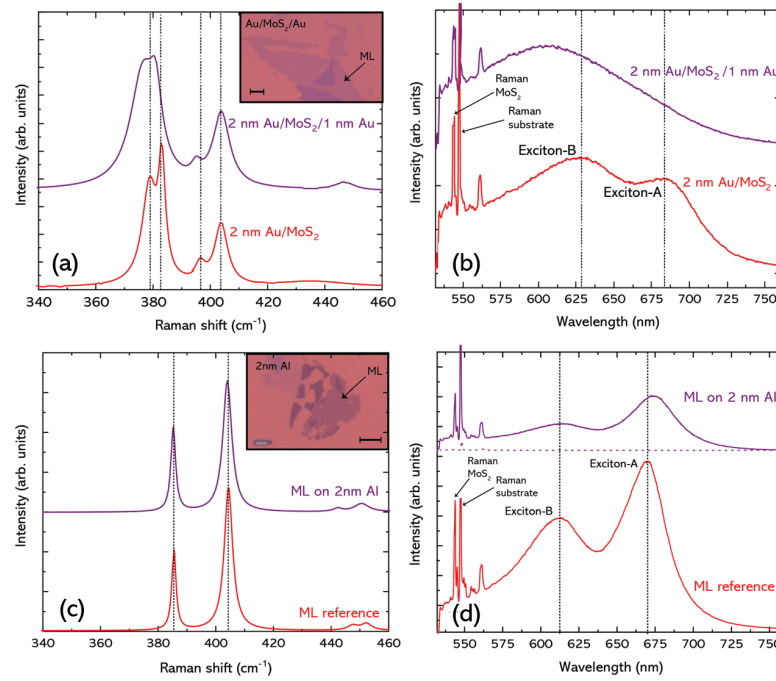


Figure 4.13 – **Au-sandwiched MoS₂ structure and MoS₂ on Al.** (a) Raman and (b) PL spectra before and after 1nm Au deposition on top of monolayer MoS₂ on a 2 nm Au. Inset in (a) shows an optical image of the MoS₂ flake (Scale bar: 10 μ m). The excitonic peaks in the sandwiched structure are fully quenched due to the charge transfer between Au nanoparticles on both sides of MoS₂. (c) Raman and (d) PL spectra from reference and monolayer MoS₂ on 2 nm Al deposited on 285 nm SiO₂/Si. The PL intensity from reference sample is divided by 2.5 for better comparison.

overlying MoS₂, and thus into the excitation of the non-Raman active modes in the spectra, such as modes outside the Γ -point.

The plasmon-phonon interaction could lead both to the removal of degeneracy of the E_{2g} mode- mode splitting- and/or to the access of modes at other symmetry points of the reciprocal space for both the E_{2g} and A_{1g} modes. Both effects would lead to peak splitting. Such peak splitting has been reported in graphene-metal nanoparticle heterostructures, where splitting of G and 2-D bands into LO and TO components has been observed [220, 221].

These new Raman modes, otherwise silent, are excited due to the additional momentum provided by the plasmons [222]. The plasmon-phonon interaction activates a double-resonant Raman process without requiring a defect for momentum conservation. In this case, a non-vertical interband excitation occurs between the direct and indirect conduction bands, and the electron is scattered by a phonon with non-zero momentum q . As a consequence, the intensity ratio between the split Raman peaks will be dependent on the gold thickness, which is evident in figure 4.9(e), and the excitation wavelength of the laser (Supplementary Information figure B.9). This would explain the universal peak splitting, independent of the size/thickness of

Au nanoparticles. Zhao et al. [223] have used this effect to explain the Raman peak splitting observed in monolayer WS_2 deposited with gold and silver nanoparticles.

To further verify this, an additional sample with 1 nm Au on top of the ML MoS_2 on 2 nm Au was investigated. Hereon, this sample is also referred to as the "Au-sandwiched MoS_2 structure." Figure 4.13(a) shows the comparison of Raman spectra of monolayer MoS_2 on 2 nm Au and the Au-sandwiched MoS_2 structure. A more detailed comparison and explanation is provided in Supplementary Information figure B.6. The PL spectra from monolayer MoS_2 on 2 nm Au and the sandwiched MoS_2 structure are shown in figure 4.13(b). Both the A- and B-exciton peaks are fully quenched in case of the sandwiched structure. This is not surprising since the Au nanoparticles are present on top and below the MoS_2 monolayer, which additionally enhances the FRET effect [183].

Finally, to verify that the plasmonic interaction between Au nanoparticles affects the vibrational and luminescence properties of MoS_2 , a monolayer flake of MoS_2 was prepared on a 2 nm Al deposited on a SiO_2/Si substrate. The surface plasmon resonance of Al nanoparticles covered by their native oxide is around 200 nm. This surface plasmon cannot be excited with our excitation sources [224, 225]. Thus, the coupling between Al plasmons and MoS_2 excitons should be inexistent. In addition, the native oxide present at the surface of Al nanoparticles could suppress charge equilibration [226]. This should both suppress any peak shift or splitting due to charge transfer or plasmon interaction. The Al layer still being rough at the nanoscale, one should detect any shift related to strain.

Figures 4.13(c) and (d) compare the Raman and PL spectra from reference and on Al. The Raman peak positions in figure 4.13(c) for monolayer MoS_2 on Al are exactly identical to the reference monolayer sample. No Raman peak splitting is seen for the E_{2g} and A_{1g} peaks. This is consistent with the hypothesis that strain related to the topography of the sample does not play a role in the splitting or shift of the E_{2g} and A_{1g} peaks. In addition, in the absence of charge transfer or plasmon interaction, the ML MoS_2 conserves its Raman features. The PL spectra for the reference monolayer and monolayer MoS_2 on Al are also identical except a small redshift of the A- and B-excitonic peaks of monolayer MoS_2 on Al. This would be in agreement with DFT calculations [227] showing that the MoS_2/Al heterostructure exhibits a slightly lower bandgap compared to a pristine ML MoS_2 . In general, the observed redshift of excitons in MoS_2 /metal heterostructures is explained by screening effects from the metal substrate [228].

It should be noted that previously, Velicky et al. [15] have considered that MoS_2 -Au interaction could also lead to the activation of silent phonons. However, their tip-enhanced Raman experiments showed disappearance of the main A_{1g} peak in some cases, which led them to rule out this possibility. This is in contrast with our Raman mapping experiments on the MoS_2 -Au system (Supplementary Information figure B.10), which have always shown the presence of both the main and split Raman peaks, thus confirming the possibility of the activation of the non- Γ phonons.

While it is difficult to determine the more dominant effect between the Au-S interaction and plasmon-phonon interaction on the activation of the non- Γ phonons, it is clear that both these phenomena could lead to universal Raman peak splitting of the A_{1g} and E_{2g} mode in MoS₂/Au structures.

4.2.5 Conclusion

In conclusion, we have provided a thorough analysis of the Raman and photoluminescence of metal-MoS₂ junctions with Au and Al as metals. We have observed a split in the two main Raman modes and a quenching of the luminescence when MoS₂ is in contact with gold. While the luminescence quenching is due to a FRET effect, the split in the Raman modes is a convolution of Au-S interaction and breaking of symmetry rules by the metallic plasmons. This work provides a procedure for the understanding of junctions in 2-D materials.

Methods

Sample preparation

Au deposition: Wafers from Nova semiconductors with 285 nm SiO₂ coated on Si were rinsed in acetone and IPA and exposed to oxygen plasma in Oxford Instruments PlasmaLab 80 RIE system. Gold was deposited on these substrates using a homemade e-beam evaporation system to corresponding thicknesses of 2, 4 and 7 nm. A 2 nm Ti film was used as an adhesion layer before the deposition of gold in the same evaporation run. Due to the non-wetting properties of Au on SiO₂, the material is corrugated at the nanoscale. Morphological characterization of the bare gold substrates is presented in Supplementary Information figure B.3. SEM micrographs of gold samples confirm nanoparticle morphology with average lateral particle size of 10 to 15 nm independent of the gold thickness. The average roughness was estimated to be around 0.3 nm based on the AFM measurements, and again independent of the gold thickness. Photoluminescence characterization of the gold samples showed a broad band centered around 570 nm which is typical Au plasmonic response of particles with a size distribution around 10 - 15 nm [229]. Furthermore, slight blue shift of the PL maximum is observed with the increasing gold thickness. This might be related to the change in the shape of nanoparticles with increasing thickness, as suggested in ref. [230]. For thinner gold layers, nanoparticles resemble more to nanodisks, with a diameter of 10-15 nm and thickness of around 2 nm. While in the case of thicker gold layers, nanoparticles are closer to a spherical shape.

Al deposition: The 2 nm Al layer was deposited using the same e-beam evaporation system on a 285 nm SiO₂/Si substrate.

MoS₂ monolayers: The MoS₂ on gold samples were prepared by mechanical exfoliation using scotch tape method. Few-layer MoS₂ flakes were exfoliated onto a scotch tape from a natural MoS₂ bulk crystal procured from HQ Graphene. Freshly deposited gold film on a quarter of a

Chapter 4. Results and Discussion

4" SiO₂/Si wafer was immediately used for exfoliation of MoS₂ on gold. Before exfoliation, the chips were rinsed in acetone and IPA and heated to 120°C for 2 mins. The scotch tape was then pressed onto the Au-coated chips and the chip was heated to 120°C for 1 min and followed by a rapid peeling-off of the tape. The thin MoS₂ flakes thus obtained on gold nanoparticle films were then visually identified using an optical microscope. Monolayer MoS₂ was transferred on Al using the polymer transfer method as illustrated in Supplementary Information figure B.1.

Characterization

The atomic force microscopy images were acquired using a Bruker Dimension AFM system using ScanAsyst Fluid+ AFM probes.

The Raman measurements were carried out in a Renishaw inVia confocal Raman microscope. A 532 nm laser was used to illuminate the sample and the beam was focused using a 100x long working distance objective. The focused laser spot was $\sim 1\ \mu\text{m}$ diameter. The Raman signal was collected by the same objective and dispersed onto a Renishaw CCD by a 3000 l/mm grating. The spectral resolution of the microscope is $0.8\ \text{cm}^{-1}$. The sample exposure to the laser was kept minimal and the laser power was kept below 0.3 mW to avoid heating effects. All the spectra are acquired for 30s over 10 accumulations to have a good signal-to-noise ratio. The Raman spectra were fit using Lorentzian functions. The photoluminescence (PL) spectra were collected using the same Raman system. The PL signal was dispersed onto a Renishaw CCD by a 300 l/mm grating. The spectra were acquired for 30s over 5 accumulations.

Data Availability

Data presented in this study are available on request from the authors

Acknowledgements

Authors thank funding from SNSF via projects 196948, BSCG10-502, PCEGP2_194528, BSCG10_157705 as well as H2020 project LIMQUET (project number 765075). M.D. thanks H2020 through the Marie Curie Project SMARTCELL (project number: 101022257). The authors thank Dr. Hannu-Pekka Komsa for the fruitful discussions. The authors also thank Didem Dede and Shreyas Joglekar for punctual technical support.

Author Contributions

M.D. and A.B. contributed equally to this work. M.D., A.B., and A. F i M. conceived the research and designed the experiments. A.B. prepared the samples with inputs from J.J. and M.B. and performed the Raman and PL measurements and analysis. M.D. and A. F i M. proposed the hypotheses. M.D. analyzed the data. A.B. and E.S. performed the polarization-dependent Raman measurements. M.D., A.B. and A. F i M. wrote the paper with inputs from all the

authors.

Competing Interests

The authors declare that there are no competing interests.

Additional Information

Supplementary information is provided in Appendix B.

Correspondence and requests for materials should be addressed to M.D. and A. F i M (email: mirjana.dimitrievska@epfl.ch; anna.fontcuberta-morral@epfl.ch).

4.3 Spatial modulation of vibrational and luminescence properties of monolayer MoS₂ using a GaAs nanowire array

A. Balgarkashi, Valerio Piazza, Jakub Jasinski, Riccardo Frisenda, Alessandro Surrente, Michał Baranowski, Mirjana Dimitrievska, Didem Dede, Wonjong Kim, Lucas Güniat, Jean-Baptiste Leran, Andres Castellanos-Gomez, Paulina Plochocka and Anna Fontcuberta i Morral

in review

This work is under review at the time of submission. The above list includes a likely list of authors.

My contributions to this work include sample preparation, structural characterization and room-temperature optical measurements along with writing of the manuscript. The MoS₂ flake transfer was done in collaboration with Dr. Riccardo Frisenda at CSIC-ICMM in Madrid and the low temperature optical measurements were done by Mr. Jakub Jasinski at LNCMI in Toulouse.

4.3.1 Abstract

The integration of transition-metal dichalcogenides (TMDs) with non-planar substrates such as nanopillars provides a way to spatially modify the optical properties mainly through the localized strain. Similar studies to date have utilized insulating SiO₂ nanopillars. Here, we combine monolayer MoS₂ with free standing GaAs nanowires (NWs), in views of coupling their semiconducting properties. We find that monolayer MoS₂ exhibits three different configurations: pierced, wrapped and tent-like. We demonstrate how to identify the configurations by optical microscopy and elucidate the impact on the vibrational and luminescence characteristics by confocal spectroscopy mapping. In particular, we highlight the increase of intensity and shift due to the photonic properties of nanowires and increase in dielectric screening associated with the GaAs NW. This work signifies the first step towards the use of vertical III-V NW arrays as a versatile platform for spatially engineering the optical properties of TMDs.

4.3.2 Introduction

Two-dimensional materials have emerged as a promising new platform for optoelectronic applications such as transistors [231], solar cells [157], detectors [232] and single photon emitters [29, 34, 120]. Monolayer transition-metal dichalcogenides (TMDs), in particular, show interesting optical, electronic and mechanical properties, including direct bandgap [5], large exciton binding energies [233] and spin and valley-selective optical transitions [234]. The ease of various transfer methods [235] has enabled integration with a high variety substrates, including non-planar surfaces [34, 35, 236–239].

4.3. Spatial modulation of vibrational and luminescence properties of monolayer MoS₂ using a GaAs nanowire array

The attributes of interface with the substrate exert a direct influence on the ML-TMD characteristics, due to the monolayer character. For example, non-planar substrates spatially modulate the strain. This modulation can be exercised using nanoparticles and nanopillar/NWs [237–239]. In addition, Fermi level alignment with the substrate alters the carrier concentration in TMDs through charge exchange [176]. This provides the ability to modulate the carrier concentration in TMDs by changing the substrate characteristics.

The integration of ML-TMDs with patterned non-planar substrates constitutes an appealing platform to engineer ML-TMDs. In particular, it has been shown that nanopillars induce a localized strain, resulting into a local change of the band structure. This can either induce exciton funneling at low temperatures [112] or efficient exciton to trion conversion at room temperature [240] in the direction of the nanopillar tip, where the strain is maximum. This enables efficient charge collection desirable for bright single photon emission. Following this strategy, nanopillars were used to controllably create single photon emitters in ML-TMDs such as WSe₂ [34, 35]. To the best of our knowledge, most works have used insulating SiO₂ nanopillars. The SiO₂ is not ideal in this application since it contains trapped charges, which creates a fluctuating dielectric environment. This causes spectral and intensity fluctuations in the optical emission of the localized emitters. This causes spectral and intensity fluctuations in the optical emission of the localized emitters [122]. Epitaxially grown III-V substrates, on the other hand, can provide a cleaner charge environment at the interface with ML-TMDs due to the absence of trapped charges [122]. In the form of nanowire (NW) arrays, III-V substrates can be used to create localized strain in TMDs. Additionally, the aspect ratio and pitch of the NW arrays can be modulated to systematically vary the strain. In addition, doping of III-V NWs provides an additional path towards the modification of the potential landscape in the ML-TMD [241, 242].

In this work, we combine ML-MoS₂ with GaAs NWs on silicon. Performing optical and atomic force microscopy maps on the same regions we identify the three different configurations that the ML-MoS₂ adopts. We then acquire Raman and photoluminescence (PL) spectroscopy maps to elucidate the effect of NWs on the properties of the ML-MoS₂.

4.3.3 Results and Discussion

We start by providing an overview of the studied system. Figure 4.14 shows a schematic drawing and the corresponding scanning electron microscope (SEM) image of a GaAs NW array at each stage of the sample preparation. GaAs NW arrays were grown by molecular beam epitaxy (MBE) on Si substrates, following [243, 244]. Figure 4.14(a) corresponds to the NW array after growth. The NWs are arranged in a square lattice of 1.6 μm side. The measured diameter and height of the NWs are ~ 55 nm and 300 nm respectively. The inset highlights a representative GaAs NW with Ga droplet on top. Prior to flake transfer, the Ga droplets were etched away in 37% HCl solution (figure 4.14(b)). We feature a representative single NW in the inset of figure 4.14(b) where the Ga droplet is clearly absent. Monolayer (ML) MoS₂

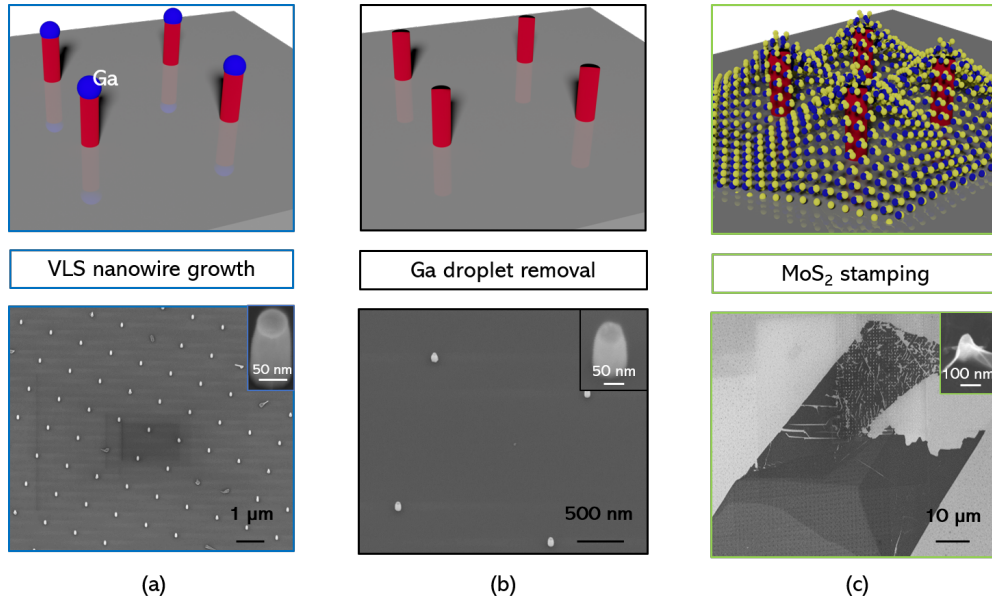


Figure 4.14 – Schematic and corresponding SEM image of a GaAs NW array (a) after growth, (b) after Ga droplet removal and (c) after MoS₂ flake stamping.

flake was then transferred on the GaAs NW array. Figure 4.14(c) depicts the SEM image of the NW array after transfer of a ML MoS₂. The inset shows a single NW with a flake on top. In this particular case, the flake is suspended on the NW tip forming a tent-like structure. More details on NW growth and flake transfer can be found in the Methods section. Monolayers were identified from the optical contrast and confirmed by Raman spectroscopy. The frequency difference between the in-plane and out-of-plane Raman peaks for a ML was found to be 20 cm⁻¹ (Supplementary information figure C.1) in agreement with previous studies [6].

Configuration identification

We turn now to the identification of the configurations adopted by the ML-MoS₂ on the NWs. Figure 4.15(a) shows an overview bright-field optical image of the monolayer MoS₂ flake on NWs. A magnified optical image from the bottom left corner of the array is shown in figure 4.15(b), which is marked by a black dashed square in (a). The dotted lines in figure 4.15(b) mark the edge of the NW array. Three different optical contrasts were identified. We have highlighted the three representative examples with colored dashed lines and further magnified them in the inset of figure 4.15(b). We label them type-I, II and III. They are respectively characterized by a half dark/bright, full bright and full dark spot.

In order to understand the topology of the flake on the NW array, the sample was studied by atomic force microscopy (AFM) and SEM. Figure 4.15(c) shows a three-dimensional view of the AFM image taken from the bottom left corner of the NW array identified with a yellow box. The AFM measurement shown in figure 4.15(c) clearly reveals that the flake does not lie identically

4.3. Spatial modulation of vibrational and luminescence properties of monolayer MoS₂ using a GaAs nanowire array

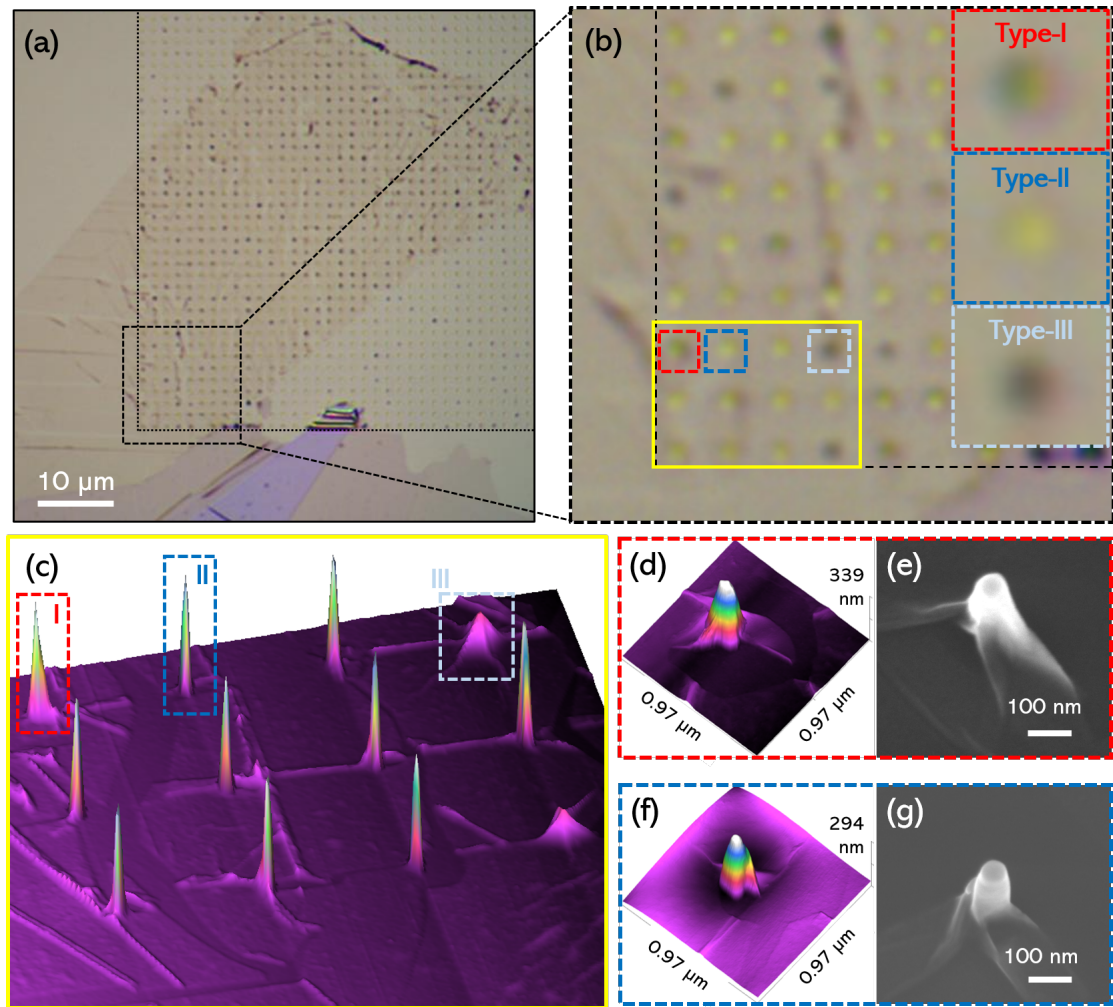


Figure 4.15 – (a) Bright-field optical image of the MoS₂ flake after transfer to GaAs NW array. (b) Magnified optical image from the bottom left corner of the NW array as indicated in (a). The insets show magnified views of NWs with three different types of optical contrast labeled as type-I, II and III. (c) A 3-D AFM image from the area denoted by yellow box in (b). The dotted rectangles denote the three different configurations of the flake on NWs. 3-D AFM and SEM images, respectively, of (d)-(e) type-I and (f)-(g) type-II configurations as indicated by red and blue dotted rectangles in (c).

on all NWs. Type-I and II configurations appear spiky, while configuration III exhibits a shorter tent-like shape. The latter corresponds to shorter NW structures that might have been broken during the transfer process. More details of type-III NWs can be found in Supplementary information figure C.2. A closer look on the type-I and type-II configurations is shown in figures 4.15(d)-(g), represented by 3-D AFM and SEM images. For the type-I configuration, the flake is conformal to the NWs as evident in figures 4.15(d) and (e). Moreover, the flake is disconnected from rest of the flake around the NW on most sides. The flake tends to wrap around the NW.

3-D AFM and SEM images of type I and II configurations are shown for direct comparison in figures 4.15(d),(f) and (e),(g), respectively. The flake appears to be pierced by the NWs in the case of type-II configuration. This is evident in the SEM image of figure 4.15(g). The pierced flake mostly lies close to the bottom of the NW. We observe a clear correlation between the optical contrast and the flake topology on a NW. The optical contrast found in the optical microscopy can be used to reliably identify the flake configuration on the NWs. Statistics on a small region of the array is provided in Supplementary Information figure C.3. Most of the NWs exhibit type-II (pierced) configuration while type-I and III constitute a small proportion of the NWs in the array. Out of 124 NWs, on average type-I and III constitute 10% each, while the rest are found to be type-II.

In the areas between the NWs, the flake lies in contact with the substrate. We think this is because of the large NW pitch, in contrast to the reduced NW diameter. In some regions, the flake exhibits ripple-like lines which may have been produced during the transfer process [236]. We also identify some regions of the flake in between the NWs which appear to be folded. Borders of folded regions may appear as faint black lines in the optical image in figure 4.15(b). We think folding may have occurred during the transfer process. For further confirmation, a representative SEM image of a folded region is provided in figure C.4.

Optical Spectroscopy

We now address the effect of the monolayer MoS₂ configuration on the vibrational and luminescence properties. Several aspects may be of an influence, such as strain and charge transfer/inference with the substrate [237] [245]. Raman spectroscopy is a powerful non-destructive tool to study strain and electronic charge effects in 2-D materials [167, 205]. In particular, it is well-known that the in-plane Raman mode (E_{2g}) of MoS₂ is sensitive to strain [16] while the out-of-plane Raman mode (A_{1g}) is more responsive to variations in the carrier concentration [102].

Figure 4.16 presents the confocal Raman mapping results of the sample shown in Figure 2. Figure 4.16(a) corresponds to the optical image of the region investigated. The numbers correspond to representative points where the spectra were extracted. Figure 4.16(b) displays these selected Raman spectra, which have been grouped according to their configuration. These were identified from the optical contrast as discussed in the previous section. The

4.3. Spatial modulation of vibrational and luminescence properties of monolayer MoS₂ using a GaAs nanowire array

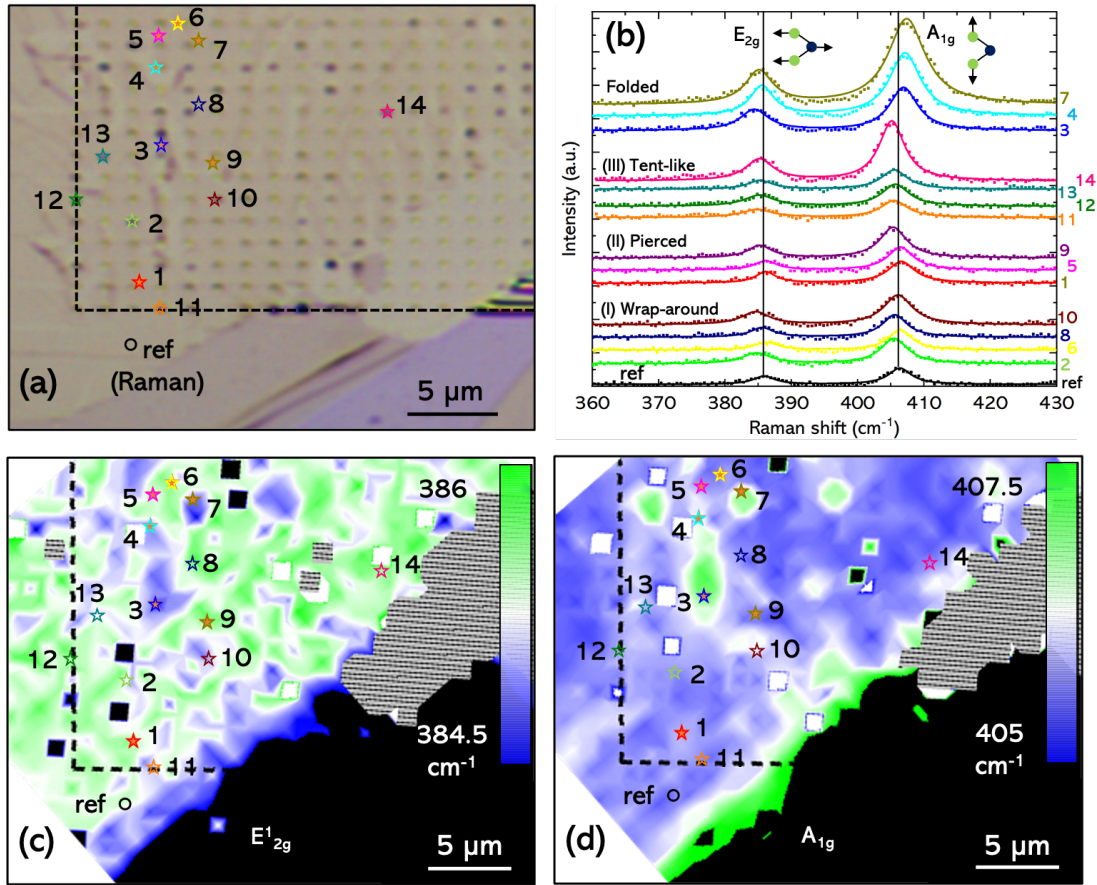


Figure 4.16 – (a) Optical image of region of the flake on NWs mapped in Raman measurements. (b) Raman spectra corresponding to the points indicated in the optical image in (a). The spectra are grouped according to the flake configuration labeled as “folded” (points 3, 4 and 7), “tent-like” (points 11, 12, 13 and 14), “pierced” (points 1, 5, 9) and wrap-around (points 2, 6, 8 and 10). “ref” indicates a reference point on the ML outside the array. (c) and (d) show the Raman maps representing E_{12g}¹ and A_{1g} peak positions acquired from the area depicted in the optical image. The black dashed lines in (a), (c) and (d) indicate edges of the NW array.

Chapter 4. Results and Discussion

groups are labeled as “folded” (points 3, 4 and 7), type III “tent-like” (points 11, 12, 13 and 14), type II “pierced” (points 1, 5, 9) and type I wrap-around (points 2, 6, 8 and 10), respectively. As a reference, the Raman spectrum acquired from a point on the ML outside the NW array is also provided. This point is denoted as “ref” in figure 4.16. Figures 3(c) and (d) correspond to the maps of E_{2g}^1 and A_{1g} Raman peak positions acquired from the same area as the optical image. The black dashed lines indicate the edges of the NW array.

We now compare each group of spectra with the reference. The symbols in each spectrum indicate the raw data and solid lines are the corresponding Lorentzian fits. Results of the fits have been listed in the Supplementary information Table-1. For the reference spectrum, the E_{2g}^1 and A_{1g} peak positions are located at 385.9 and 406.4 cm^{-1} respectively with a frequency difference, $\Delta f \sim 20.5 \text{ cm}^{-1}$ compatible with a monolayer MoS_2 [6]. Spectra from points 3, 4 and 7 corresponds to regions where the MoS_2 has been folded. The spectra exhibit a redshift of the E_{2g}^1 mode ($\sim 1.5 \text{ cm}^{-1}$) and a blueshift of the A_{1g} mode ($\sim 1 \text{ cm}^{-1}$). The frequency difference between the two modes at these points was found to be 22.5 cm^{-1} . Additionally, enhanced intensity of the Raman peaks is observed for this configuration, when compared to the reference. Both of these factors are consistent with a multilayer behavior [6, 222]. Such regions can also be identified in the Raman maps of figure 4.16(c) and (d) with a blue and green texture which indicates an increase in Δf .

The second group of spectra represents a “tent-like” configuration. The Raman spectra at these points (11, 12, 13 and 14) are characterized by a downshift in both the E_{2g}^1 and A_{1g} modes. The E_{2g}^1 mode redshifts by 0.7 cm^{-1} . This is attributed to a tensile strain induced by the NW in the ML flake. In this configuration, the flake is supported by the NW and forms a tent. Such tent-like structures on SiO_2 nanopillars have been shown to induce a tensile strain in the monolayer [237]. In addition, the A_{1g} mode also redshifts by 0.9 cm^{-1} . We attribute this to either an unintentional doping or charge transfer in the flake from the underlying substrate [246].

In the third group of spectra (1, and 9), the flake has been “pierced” by the NWs. The Raman peak positions in spectra from points 1 and 5 are similar to the reference and do not show any considerable shift. Only in the case of point 9, a small redshift in both the Raman modes is observed. Similarly, for the fourth group of spectra (points 2, 6, 8 and 10) labels as “wrap-around,” the shift at each point is slightly different. For instance, points 2 and 10 are characterized by a redshift of the E_{2g}^1 ($\sim 1 \text{ cm}^{-1}$) mode compared to the reference. Whereas for points 6 and 8, the E_{2g}^1 peak position is similar to the reference. In case of the A_{1g} mode, points 2 and 8 show a redshift ($\sim 0.8 \text{ cm}^{-1}$) in comparison to the reference peak, while for points 6 and 10, no considerable shift in the A_{1g} peak position is observed. From the peak shifts observed above, the Raman spectra for “pierced” and “wrap-around” configurations do not show a clear trend. There is a point-to-point variation even within these two groups. This is in contrast to the “folded” and “tent-like” configurations which showed a clear multilayer behaviour and redshift in both the Raman peaks, respectively. This is an interesting observation which we attribute to the fact that the “pierced” and “wrap-around” configurations are more disordered compared

4.3. Spatial modulation of vibrational and luminescence properties of monolayer MoS₂ using a GaAs nanowire array

to the other two configurations. For example, when a flake is pierced by the NW, it can either be fully or partially pierced. A fully pierced flake will then lie flat on the substrate around the NW. For a partially pierced flake, the topography will be different from NW to NW depending on how the flake gets pierced.

We thus note that the strain profile in each case will be complex and can either be partially or fully relaxed implying non-uniform shifts in the E_{2g}^1 peak. A similar reasoning can be made in case of the wrap-around configuration with variations in how the flake wraps around the NW. Likewise, the shifts in A_{1g} peak will also depend on how the flake interacts with the substrate. The flake is either in contact with the SiO₂ substrate or GaAs NWs or both. This again implies non-uniform shifts in the A_{1g} peak. At this point, individual effects for these two configurations cannot be distinguished. Although variations in the Raman peaks, in general, provide a proof of strain and charge transfer induced due to coupling between the ML MoS₂ and GaAs NWs.

We now turn to correlate the flake configuration with the luminescence properties using confocal PL spectroscopy. Figure 4.17 presents the confocal PL mapping of the ML MoS₂ on GaAs NWs. Figure 4.17(a) shows an optical image of the region mapped in the PL measurements. Figure 4.17(b) and (c) show the PL energy and intensity maps, respectively, corresponding to the area shown in (a). The dashed black lines indicate edges of the NW array. Figure 4.17(d) shows the PL spectra extracted from the points indicated in figures 4.17(a) and (b) and correspond to the points studied in the Raman measurements except for the reference. The reference point on the ML used for Raman spectral comparison (denoted as "ref (Raman)") is close to the edge of the NW array. The PL emission peak from the ML shows a blueshift as we approach the edges of the NW array. An additional reference point is taken far away from the array, denoted as "ref (PL)."

We now compare the PL spectra from MoS₂ on NWs with the reference. As shown in figure 4.17(d), the PL spectra are characterized by two main features: a dominant peak centered around 1.9 eV and a broad band in the range of 1.6-1.85 eV. The peak at 1.9 eV is attributed to excitonic emission in ML MoS₂ [247]. The PL emission shows a consistent blueshift of 10- 15 meV in comparison to the reference. The origin of this blueshift will be discussed in detail below. The broad emission band in the range of 1.6-1.85 eV is attributed to the L-band emission caused by the existence of passivated S-vacancies [248]. S-vacancies in exfoliated single layers of MoS₂ are usually passivated by oxygen atoms which are present either as part of adsorbates or as substitutional atoms [247]. In our case, this band is observed in all PL spectra, without any changes between the ML MoS₂ on NWs or reference.

The luminescence properties of monolayer 2-D materials can be affected due to (i) strain [7], (ii) charge transfer [176], (iii) defect passivation [249] and (iv) dielectric screening [250]. Below we make a systematic discussion on how these effects might contribute to the origin of the blue shift of 1.9 eV PL peak observed in our case.

Strain and charge transfer: We observe only a small shift of the E_{2g}^1 and A_{1g} Raman modes in

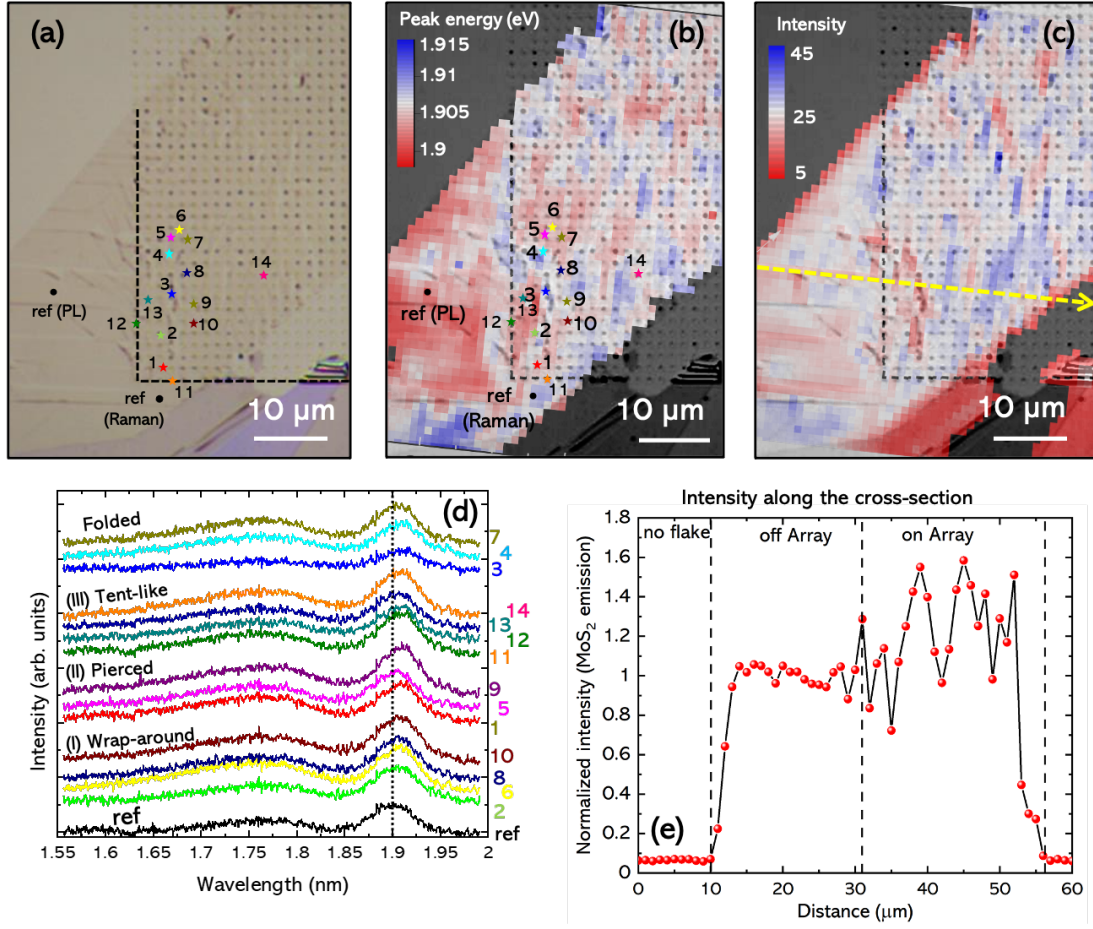


Figure 4.17 – (a) An optical image of the region mapped in the PL measurements. (b) and (c) show the PL energy and intensity maps, respectively, corresponding to the area shown in (a). The dashed black lines indicate edges of the NW array. (d) PL spectra extracted from the points indicated in (a) and (b), corresponding to the points used in the Raman measurements except the reference. A new reference point is taken for PL spectral comparison, denoted as “ref (PL).” (e) An intensity linescan across the cross-section indicated by a dashed yellow line in (c).

4.3. Spatial modulation of vibrational and luminescence properties of monolayer MoS₂ using a GaAs nanowire array

the ML MoS₂ on NWs. This indicates a marginal effect of strain and doping on the PL spectra of ML MoS₂ on NWs. However, considering that there is no systematic trend in the shift of the Raman peaks in the ML MoS₂ on NWs (figure 4.16), it is unlikely that this is the main cause of the consistent blue shift of the 1.9 eV peak that is observed in ML MoS₂ on NWs.

Defect passivation: The physical adsorption of water and oxygen molecules at S-vacancies on MoS₂ may lead to passivation of defects and introduce p-type doping compared to ideal MoS₂ surface [251]. This leads to a trion to exciton conversion and could result in a blueshift of the PL peak. A blueshift of 40 meV is observed even for a thin layer of adsorbates and is typically followed by an enhancement in the PL intensity [252]. Considering that S-vacancies have already been passivated in our sample, based on the appearance of L-band [247] in PL spectra, and there is no change in the shape, intensity or position of the L-band between the reference and the ML MoS₂ on NWs, we can exclude this effect as a reason for the blueshift of the PL emission peak.

Dielectric screening: Engineering the surrounding dielectric environment can also modify the PL emission in ML-TMDs [250]. For example, the dielectric constant of the environment has a strong effect on the exciton binding energy [249]. PL blueshifts up to 40 meV were observed for the excitonic peaks by varying the effective dielectric constant from 2 to 33 by Lin et. al. [249]. Additionally, the trion/exciton intensity ratio can also be tuned by an order of magnitude. Figure C.6 (a) and (b) present the results of a Lorentzian peak fitting to the PL spectra of monolayer MoS₂ on SiO₂ (reference) and GaAs, respectively. The two Lorentzians account for the neutral A-exciton peak and the trion peak. The trion to A-exciton intensity ratio extracted from the fitting is 1.27 and 0.45 for SiO₂ and GaAs, respectively. This induces an overall blueshift in the PL emission peak of 15 meV from 1.896 eV to 1.911 eV from SiO₂ to GaAs. Based on these observations, one could attribute the blueshift observed here to an enhanced dielectric screening of the Coulomb potential due to the high dielectric constant of GaAs ($\epsilon = 12.9$) [253], which is almost four times that of SiO₂ ($\epsilon = 3.9$) [254]. This is consistent with the prior work of Lin et. al. [249]. A further confirmation of this is provided by PL measurements on ML WSe₂ on SiO₂, planar GaAs and GaAs NW substrates (Supplementary information figure C.6) where we also see a blueshift in the excitonic emission peak of ML WSe₂. Considering that Lin et. al. [249] have used non-ionic liquids as the dielectric environment to avoid the effects of strain and doping, in our case, we need to take in account the effect of substrate in terms of strain and doping on the PL spectra. As discussed previously, observation of no systematic trend in shift of Raman peaks in ML MoS₂ on NWs indicates only a marginal effect of strain and doping, respectively. Thus, we believe the dielectric screening effect should be dominant in blueshift of the PL emission.

The PL intensity map in figure 4.17(c) shows an overall increase in the emission intensity on the NWs compared to the planar region. To further illustrate this in a quantitative manner, figure 4.17(e) provides an intensity linescan across the cross-section indicated by a dashed yellow line in (c). The three regions are denoted as no flake, off array and on array. The emission intensity is normalized to the off-array part of the ML. No emission is observed in

the absence of a ML. As we approach the ML flake, the emission intensity on the NW array is almost twice the emission intensity off array. We attribute this to the photonic effect of NWs which enhances the brightness around the NWs [25, 39, 131]. This photonic enhancement effect can be tuned further by optimizing the aspect ratio of the NWs [27].

4.3.4 Conclusion

In conclusion, we have successfully demonstrated the combination of a monolayer MoS₂ with a GaAs NW array. Detailed structural studies reveal different configurations of the flake on NWs. We evidence variations in the vibrational properties of the monolayer as an effect of strain and charge transfer due to the NWs. The luminescence shows a blueshift of the PL emission peak as a result of enhanced dielectric screening due to GaAs NWs. This provides a proof-of-concept to combine monolayer TMDs with III-V NWs and opens up possibilities to engineer the strain and enhance light extraction from monolayer TMDs.

Methods

Growth

Thermally oxidized Si substrates (15 nm SiO₂) were patterned using e-beam lithography. The substrates were etched in a 1% HF solution to remove the native oxide within the nanoholes prior to loading into the MBE growth chamber. Ga droplets were selectively deposited into the nanoholes for 10 minutes. These droplets serve as catalysts for the growth of GaAs NWs. Nanowires are then grown by the vapor-liquid-solid (VLS) mechanism for 10 minutes under Ga and As₄ fluxes of 1.4×10^{-7} Torr and 2×10^{-6} Torr, respectively. This corresponds to a GaAs planar growth rate of 1 Å/s. The morphology of nanowires is studied using a Zeiss Merlin scanning electron microscope (SEM) and a Bruker FastScan atomic force microscope (AFM) in non-contact mode.

Flake transfer

MoS₂ flakes were obtained by mechanical exfoliation from a natural molybdenite crystal from Moly Hill mine (Quebec, Canada) on a Gel-Film (WF x4 6.0 mil) supplied by Gel-Pak®. A monolayer MoS₂ flake was deterministically transferred to a NW array substrate using an all-dry viscoelastic stamping process [255]. The flake exfoliated on a Gel-Film film is attached to a glass slide and the glass slide is used as a stamp. The stamp is first aligned with the NW array and then brought in contact using a Z-axis manipulation stage. Following this, a cotton bud is used to gently press the Gel-Film stamp onto the array.

4.3. Spatial modulation of vibrational and luminescence properties of monolayer MoS₂ using a GaAs nanowire array

Characterization

For optical spectroscopy, the samples are mounted on the cold finger of a helium flow cryostat. The cryostat is bolted to computer controlled, motorized X-Y translation stages, which allow two-dimensional in-plane motion. The position of the stages is controlled with micrometer screws, either manually or by automatized stepper motors. Programmable automatic motors allow for mapping measurements, by scanning the sample surface step by step. The PL and Raman measurements were performed using either a CW solid state laser emitting at 405 nm or 532 nm. The excitation beam was focused on the sample by a 50x microscope objective with a numerical aperture of 0.55, giving a spot size of approximately 1 μm . The excitation laser power was kept below 100 μW to avoid heating effects. For PL mapping, the signal was detected in a confocal configuration to improve the spatial resolution. The emitted PL or Raman signal was collected through the same objective and redirected to a spectrometer equipped with a liquid nitrogen-cooled charge-coupled device camera.

Acknowledgements

Authors thank funding from SNSF via projects 196948. This work is part of a project that has received funding from the European Union's Horizon 2020 research and innovation programme under the Marie Skłodowska-Curie grant agreement no. 765075, project LIMQUET. ACG acknowledges funding from the European Research Council (ERC) under the European Union's Horizon 2020 research and innovation program (grant agreement no. 755655, ERC-StG 2017 project 2D-TOPSENSE).

Additional Information

Supplementary information is provided in Appendix C.

Correspondence and requests for materials should be addressed to A. F i M (email: anna.fontcuberta-morrall@epfl.ch).

5 Conclusions and Outlook

In this thesis, we have explored approaches to obtain bottom-up axial heterostructures in GaAs nanowire (NW) arrays and NW/2-D material hybrid system. While this approach offers the ability to deterministically position quantum dots (QDs) on the axis of GaAs NWs, it also takes advantage of the efficient light collection mechanism due to waveguiding-like properties of NWs. Our results contribute to the efforts towards obtaining single photon emitters which are an important component for applications in quantum technologies.

In the first part, the growth of axial and radial In(Ga)As segments on GaAs NWs on Si substrates was demonstrated. The consumption of Ga droplet before the deposition of InAs resulted in different tip morphologies at the NW tip. Most of the NWs were found to have a truncated tip with a flat triangular $\{111\}$ B facet on top. By varying the growth temperature and deposition time, we demonstrated the formation of axial In(Ga)As clusters. By reducing the deposition time, pure InAs segments were found to accumulate on the inclined facets at the NW tip. In addition, In(Ga)As clusters were also observed at the edges separating the $\{110\}$ NW side facets. The convex nature of the $\{11-2\}$ corner facets is proposed to be responsible for strain relaxation and nucleation of the 3D In-rich clusters. We showed how facet-driven nanostructure self-assembly can be used to grow axial and radial QDs in lattice-mismatched NW heterostructures.

The following part was focused on studying the interaction of monolayer MoS₂ with gold using Raman and PL spectroscopy. A simultaneous peak splitting was observed in the two main Raman modes of monolayer MoS₂ in contact with Au. Firstly, the peak splitting observed in our experiments was compared with the literature. It was found to be a universal feature of the MoS₂/Au system independent of Au thickness and sample configuration. Secondly, analysis of simultaneous peak splitting based on the common notions of strain and doping was found to overestimate the values of strain and carrier concentration in the MoS₂/Au system. We proposed a mechanism based on structural perturbations and plasmon-phonon interaction at the MoS₂-Au interface to be responsible for the peak splitting which leads to the activation of non- Γ phonon modes away from the Brillouin zone center. The positions of split peaks were found to coincide with frequencies at the M-point of the Brillouin zone in the phonon dispersion of MoS₂. The effect of plasmonic interaction was further elucidated by studying a

Chapter 5. Conclusions and Outlook

sample with monolayer MoS₂ on Al. This sample showed no peak splitting. Our work can be further applied to understand TMD-metal junctions.

In the last part, the integration of MoS₂ monolayer on an ordered array of GaAs NWs was demonstrated. Depending on the aspect ratio of the underlying NWs, the flake was found to exhibit three different configurations: pierced, wrap-around and tent-like. Changes in vibrational properties were evidenced by Local fluctuations in peak positions of the E_{2g} and A_{1g} modes in Raman mapping measurements. These were attributed to variations in strain and charge accumulation in the monolayer on and off the NWs. The optical properties of the monolayer were studied using confocal micro-PL mapping. Furthermore, we also combined monolayer TMDs with an ordered nanomembrane (NM) array. This sample is currently being studied and preliminary results indicate a polarization-dependent emission from the MoS₂ monolayer. Combining monolayer TMDs with NWs provides a versatile platform to spatially engineer the optical properties of TMDs.

To look further, the outlook of this thesis can be divided into two categories: first is focused on the future improvements on axial NWs heterostructures and the second is on the prospects of III-V nanowire/monolayer TMD hybrid systems.

Outlook: NW heterostructures

For the InAs/GaAs NW heterostructures, axial InAs clusters were achieved. Although the sidewall clusters were emitting, significant improvement in the shell capping quality is needed for obtaining optically active axial InAs clusters. For this, the the shell growth conditions can be optimized to reduce the defect density. Secondly, by reducing the NW diameter during the growth process, thin nanoneedles (NNs) can be obtained. Initial experiments were performed to deposit InAs on top of NNs. The results are presented in Appendix D, where figure D.1 shows the deposition of InAs on top of 20 nm thin GaAs NNs. This could offer the potential to realize fully 3-D confined NWQDs.

Lastly, we had aimed to grow GaAs/AlGaAs NW heterostructure. However, due to issues with the Al cell in the MBE, we were unable to attempt the growth of these NW heterostructures. One could think of obtaining structures similar to InAs/GaAs but without the constraints of lattice mismatch for this system. Priante *et. al.* have shown that abrupt GaAs-AlGaAs interfaces [92] in self-catalyzed NWs are generally sharper than those obtained by gold-catalyzed method. Furthermore, their simulation results have shown that small droplet volumes should allow the fabrication of ultra-sharp interfaces, which would be made possible by growing GaAs/AlGaAs NNs with less than 20 nm diameter.

The integration of vertical NWQDs into SiN waveguides offers the prospect of integrating photon emitters with existing quantum technologies [154]. In addition to vertical NW arrays, horizontal nanomembranes (NMs) are interesting since they can be grown in the form of networks. An example of NMs grown in the form of nanocrosses is shown in figure 2.13. The

waveguiding effect in horizontal NWs can be used to laterally couple the photon emission from QDs. Realization of such structures will allow the bottom-up growth and on-chip integration of quantum emitters.

Outlook: 1-D/2-D heterostructures

Our initial studies on 2-D materials was focused on understanding ML MoS₂-gold interface. Since the understanding of TMD-metal junctions is crucial for devices, it will be useful to study other TMD-metal interfaces and explore the interactions using Raman and PL spectroscopy. In the second part of the work on 2-D materials, we combined ML MoS₂ with a GaAs NW array. Here, a high dielectric constant of the substrate was shown to have an impact on the optical emission of the monolayer. Therefore, a study on the effect of different III-V planar substrates on ML TMDs will be essential.

For the integration of ML MoS₂ with NWs, the spatial resolution in Raman and PL mapping in our current work of section 4.3 is limited by the laser spot size ($\sim 1 \mu\text{m}$). The next step will be to transfer a monolayer MoS₂ on NW array with a pitch higher than $2 \mu\text{m}$ to elucidate the effect of individual NWs. By further varying the NW aspect ratio and pitch further, strain can be modulated in the monolayer. The transfer technique should be extended to other TMDs such as WS₂ and WSe₂, for example. By inducing local strain using vertical NWs, quantum emitters with sharp excitonic linewidths [34] can be positioned deterministically in these materials. The extraction efficiency of these QDs will be enhanced by the underlying NWs acting as waveguides. To understand this effect, finite-element time-domain (FDTD) simulations of the near-field and far-field emission coupling will be useful to understand the waveguiding effect due to NWs.

One of the main motivation to combine monolayer TMDs with III-V NWs is to improve the spectral stability of emitters generated in the TMDs [122]. In comparison to SiO₂ nanopillars, which are commonly used, the absence of surface charges in III-V NWs is supposed to provide this stability. In the NWs we have studied, the surface of GaAs NWs is oxidized when exposed to air. The GaAs native oxide will contain surface charges [256]. This native oxide can be etched away in ammonium sulfide before combining them with the TMD monolayers.

In conclusion, this work opens up many new directions to integrate arrays of single photon emitters on Si substrates. As we saw above, many aspects in both NWQD heterostructures and 1-D/2-D hybrid systems still need to be understood. The research community is progressing at a rapid pace to understand the many fundamental aspects of these systems. The technological implications upon successful realization of these systems outweigh the current significant challenges and I am enthused to see the deployment of these systems in quantum information processing.

A Supplementary: Facet-driven formation of axial and radial In(Ga)As clusters in GaAs nanowires

In order to investigate the formation mechanism and the evolution of the observed In(Ga)As axial clusters, two sets of NW samples (samples 2 and 3) with different InAs deposition times and In BEPs were fabricated. The detailed growth parameters are presented in Table A.1. Figures A.1 (a) and (b) show the HAADF images of NWs from sample 2 and sample 3, respectively. We find that the In(Ga)As clusters are always observed on the (100) inclined top facet. This is likely a result of the S-K growth of In(Ga)As on the inclined top facet or corner facet formed at the intersection of two facets at the tip. S-K growth of 3-D InAs islands on GaAs (100) substrates is a widely reported phenomenon [257, 258]. However, on capping with a GaAs shell, the tip of the NW looks defective as is evident from the HAADF image in figure A.1 (d).

| | In BEP (Torr) | Deposition time (sec) | Post-treatment |
|-----------------|----------------------|-----------------------|--------------------------------------|
| Sample 1 | 8.4×10^{-8} | 5 | - - - |
| Sample 2 | 4.0×10^{-8} | 5 | In-situ annealing for 5 min at 650°C |
| Sample 3 | 2.2×10^{-8} | 5 | In-situ annealing for 5 min at 650°C |

Table A.1 – Growth parameters for InAs deposition.

Appendix A. Supplementary: Facet-driven formation of axial and radial In(Ga)As clusters in GaAs nanowires

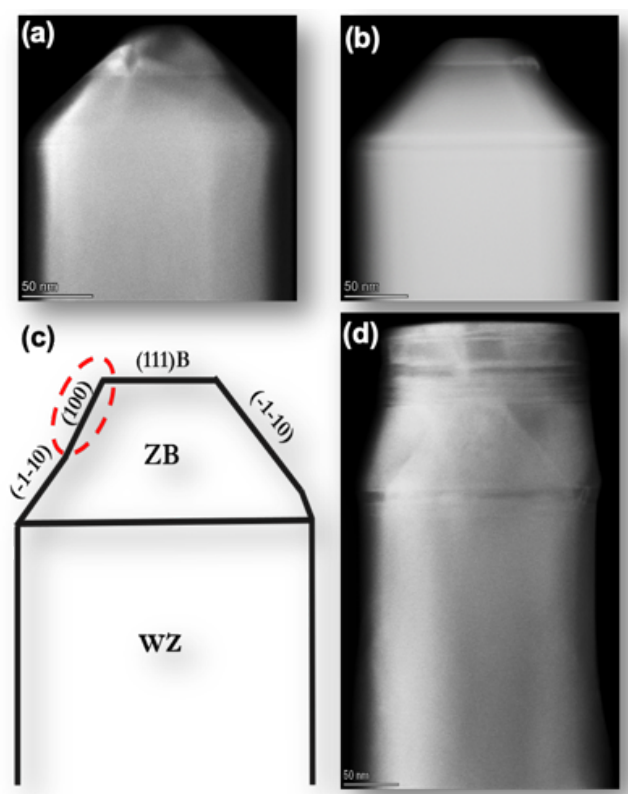


Figure A.1 – HAADF-STEM images from tip of NWs in samples 2 and 3 as indicted in table A.1

B Supplementary: On the origin of Raman peak splitting in monolayer 2D materials-metal interfaces: MoS₂Au

Sample Preparation

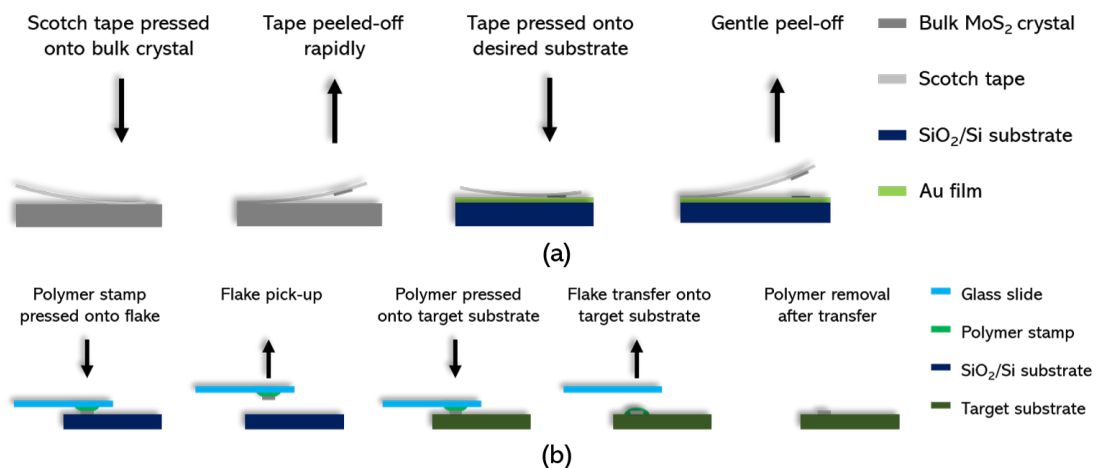


Figure B.1 – **Illustration of sample preparation methods.** (a) exfoliation of MoS₂ on SiO₂/Si and Au substrates using the scotch tape method. (b) Polymer transfer method used for transfer of exfoliated MoS₂ flake on Al deposited on SiO₂/Si substrate.

Determination of monolayer MoS₂

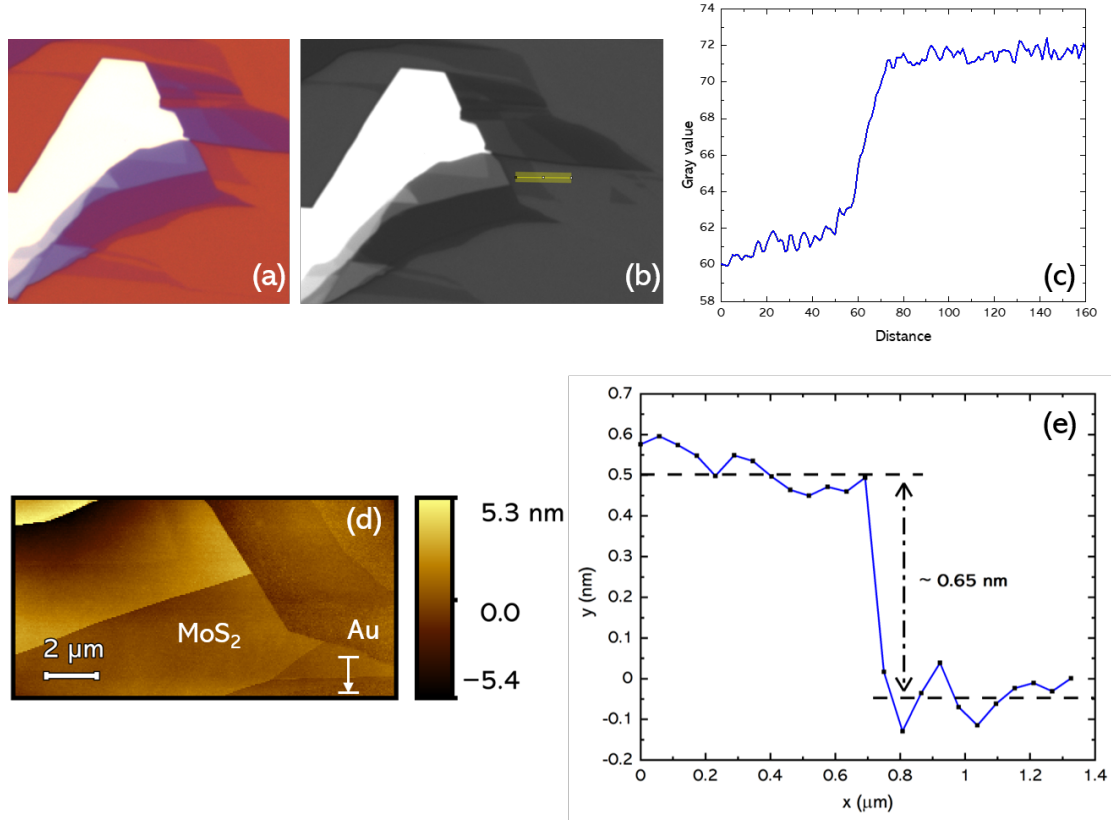


Figure B.2 – **Determination of monolayer MoS₂ on gold.** (a) Optical micrograph of an MoS₂ flake (b) Green channel image of the MoS₂ flake obtained by splitting the RGB channels of image in (a) using analysis software ImageJ. (c) Optical contrast linescan profile, as indicated in (b) used in determination of a monolayer MoS₂ on Au: $(GV_{\text{substrate}} - GV_{\text{flake}}) / GV_{\text{substrate}}$, where GV = Gray value. In case of monolayers, the optical contrast difference was found to be ~15%. (d) AFM image and (e) linescan profile of the MoS₂ flake shown in (a). A thickness of 0.65 nm confirms the thickness to be a monolayer.

SEM and AFM analysis of Au films

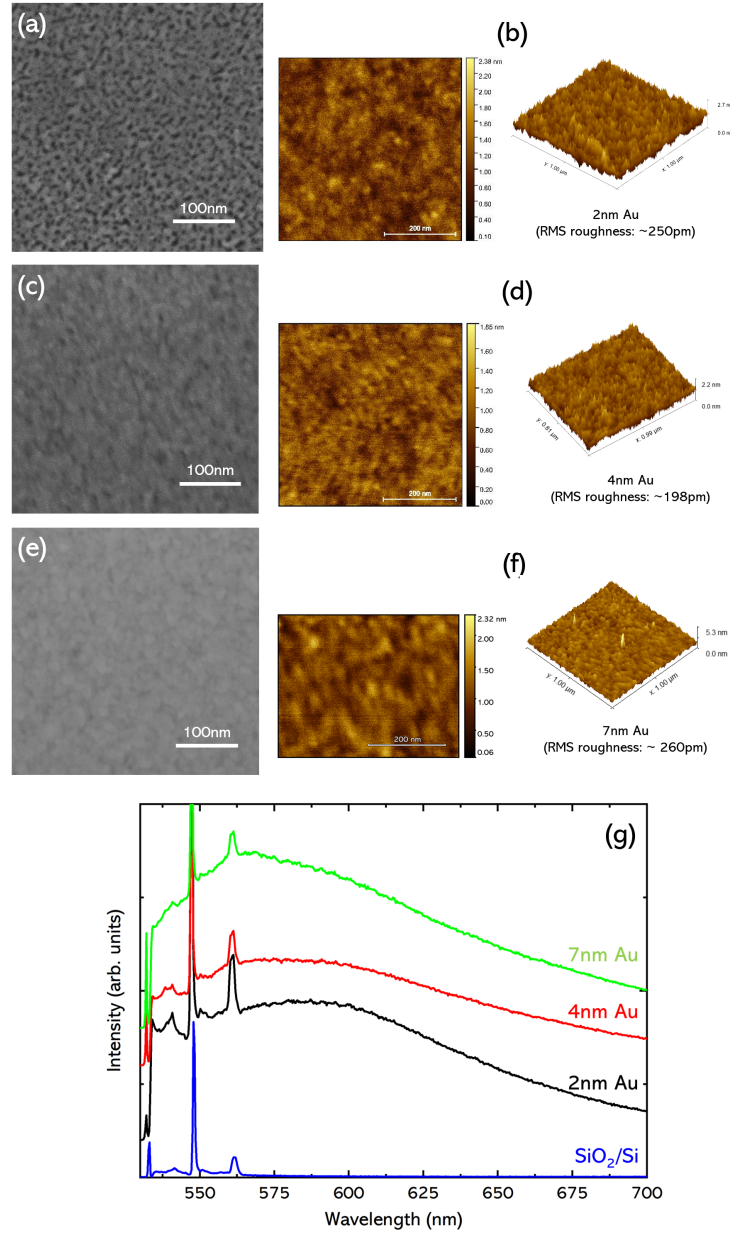


Figure B.3 – (a), (b) and (c) SEM and (d), (e) and (f) AFM images for (a) 2 nm, (b) 4 nm and (c) 7 nm Au, respectively. The roughness of the Au substrates was obtained from the AFM image analysis and varies between 0.2-0.25 nm. The grain sizes obtained from SEM image of the 7nm Au were found to be in the range of 10-15 nm.

Raman peak splitting in monolayer MoS₂

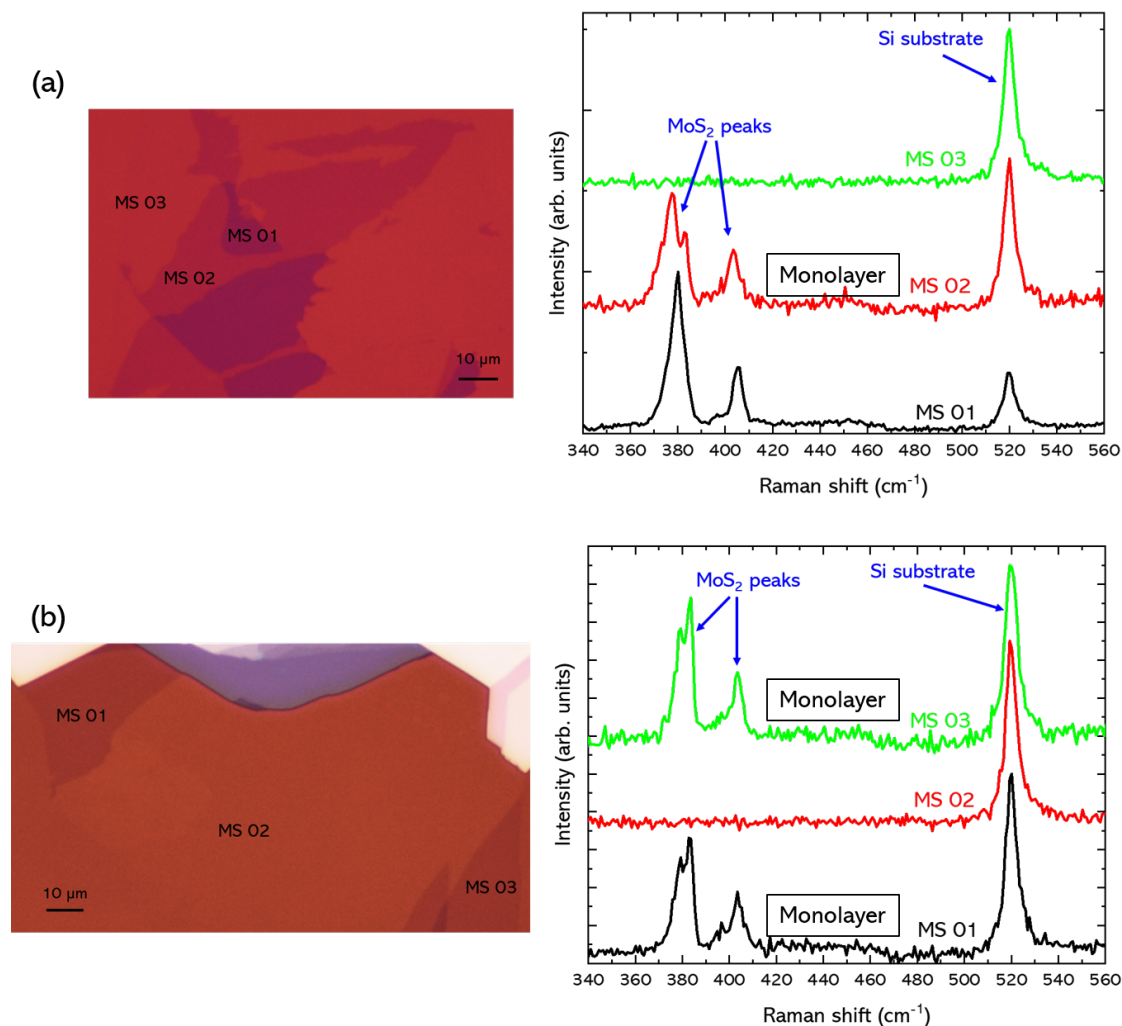


Figure B.4 – **Optical micrographs (left) and Raman spectra (right) acquired from different regions of MoS₂ exfoliated on 2nm Au.** (a) Raman spectra acquired from a thicker MoS₂ flake (MS01), monolayer MoS₂ flake (MS02) and Au substrate (MS03). The Raman peak splitting is observed only in case of monolayer MoS₂. (b) Raman spectra taken from two different MoS₂ monolayers (MS01 and MS03) and Au substrate (MS02). Both the monolayers exhibit peak splitting in the Raman spectra.

Comparison of MoS₂ deformation on a nanopillar vs Au

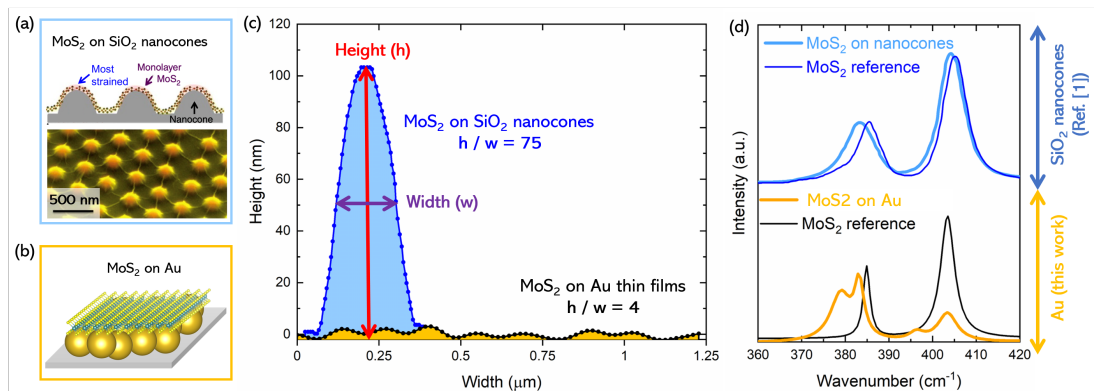


Figure B.5 – **Deformation of MoS₂ monolayer on nanocones vs Au.** (a) MoS₂ monolayers on SiO₂ nanocones from ref [20]. (b) MoS₂ monolayers on Au substrates in this work. (c) Deformation of MoS₂ monolayers on top of SiO₂ nanocones and Au, calculated from TEM and AFM measurements, respectively. The much higher aspect ratio in the case of nanocones (75) when compared to Au substrate (4) shows that the mechanical deformation induced by Au can be considered negligible. (d) Comparison of Raman spectra of MoS₂ monolayers on SiO₂ nanocones (obtained from reference [20]) and Au (this work). Shift in Raman peaks in case of nanocones is smaller than in the case of Au, clearly showing the origin of peak splitting is not induced by the mechanical strain due to MoS₂ deformation.

The E_{2g} Raman peaks in the sandwiched structure show a red shift compared to monolayer on 2 nm Au (Supplementary figure S-5). Additional deposition of Au in the Au-sandwiched MoS₂ structure increases the number of extrinsic defects when compared to monolayer MoS₂ on 2 nm Au. This is further confirmed by increased broadening of the peaks in the Au-sandwiched MoS₂ structure. Higher concentration of defects will cause further downshift of the E_{2g} and E_{2g}' modes, as expected by the phonon confinement discussed previously. We note the peak splitting in the sandwiched structure is nearly identical to the monolayer on 2 nm Au (Supplementary figure S-5). This again shows that the E_{2g} Raman peak splitting is independent of the nanoparticle size/thickness, but arises due to fundamental nature of the interaction between monolayer MoS₂ and Au nanoparticles rather than strain. Increase in number of defects will also cause upshift of the A_{1g} mode (Supplementary figure S-5), based on the positive phonon dispersion curvature around the Γ -point. However, for the non- Γ A_{1g}' mode, the phonon dispersion curvature could actually be negative around a certain non-zero wave vector q [203, 218, 219]. This will cause a downshift of the A_{1g}' mode, in difference to A_{1g} mode. This explains the slightly larger peak splitting of 8.5 cm⁻¹ for the A_{1g} mode in the Au-sandwiched MoS₂ structure (Supplementary figure S-5) when compared to other cases.

Peak Statistics for MoS₂ on 2 nm Au and Au-sandwiched MoS₂ structure

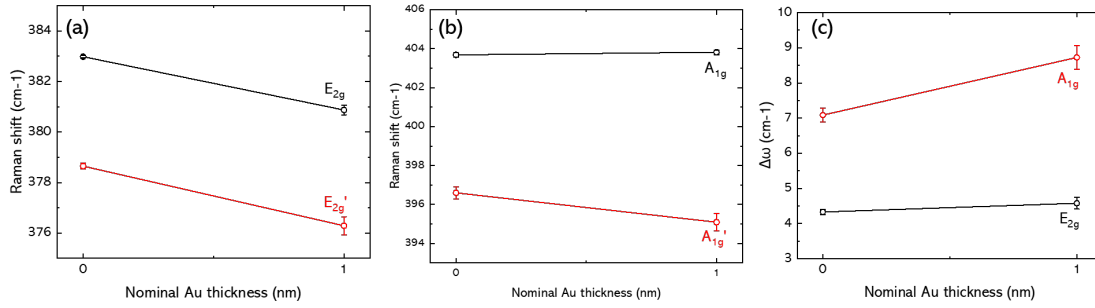


Figure B.6 – (a)-(b) Raman peak positions and (c) peak splitting of the E_{2g} and A_{1g} Raman modes in monolayer MoS₂ on 2 nm Au without and with 1 nm Au deposited on top.

Polarization-resolved Raman spectra

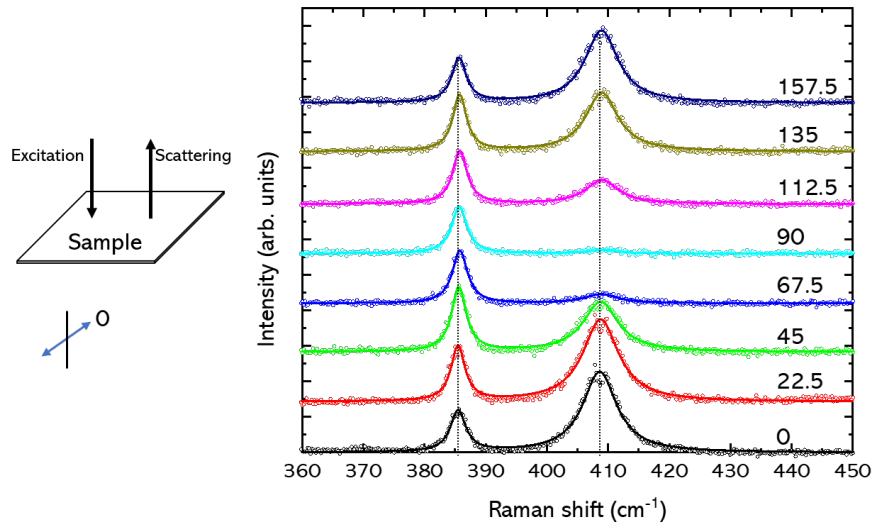


Figure B.7 – Polarization-resolved Raman spectra for monolayer MoS₂ reference on SiO₂/Si.

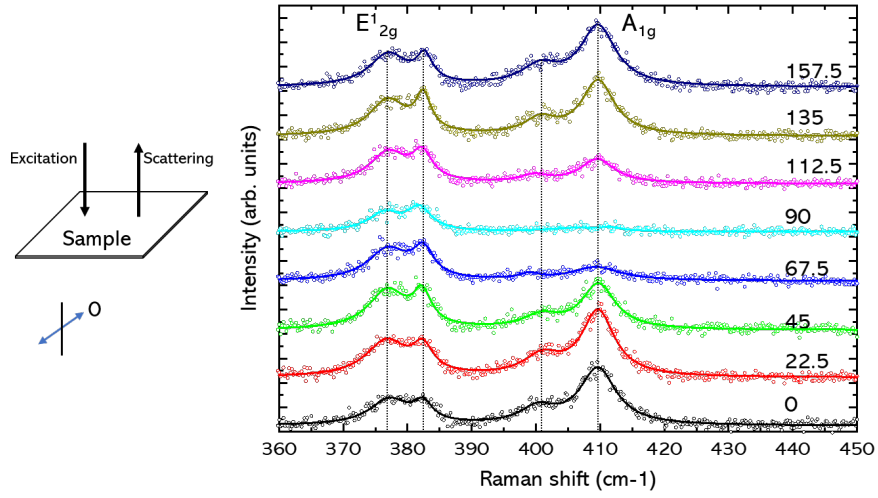


Figure B.8 – Polarization-resolved Raman spectra of monolayer MoS₂ on 2 nm Au.

Excitation wavelength-dependent Raman spectra

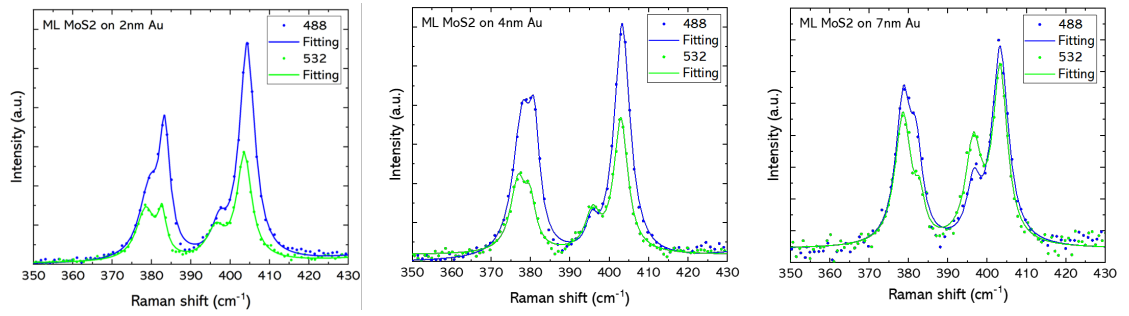


Figure B.9 – **Excitation wavelength-dependent Raman spectra** for MoS₂ on (a) 2 nm, (b) 4 nm and (c) 7 nm Au respectively, using 488 nm and 532 nm excitation laser sources. The second-order Raman bands are observed around 450 cm⁻¹ [21]. However, the relative intensities compared to the first-order Raman modes is low to comment on the behavior of these modes.

Raman linescans in ML MoS₂ on Au

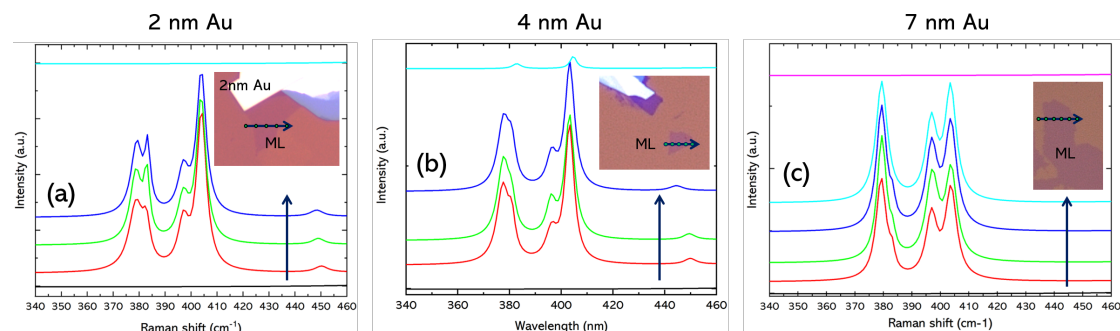


Figure B.10 – Raman linescans along the ML MoS₂ on (a) 2 nm, (b) 4 nm and (c) 7 nm Au respectively, using 532 nm excitation. The spectra show presence of both the main and split Raman peaks in all cases where MoS₂ ML is on top of Au.

C Supplementary: Spatial modulation of vibrational and luminescence properties of monolayer MoS₂ using a GaAs nanowire array

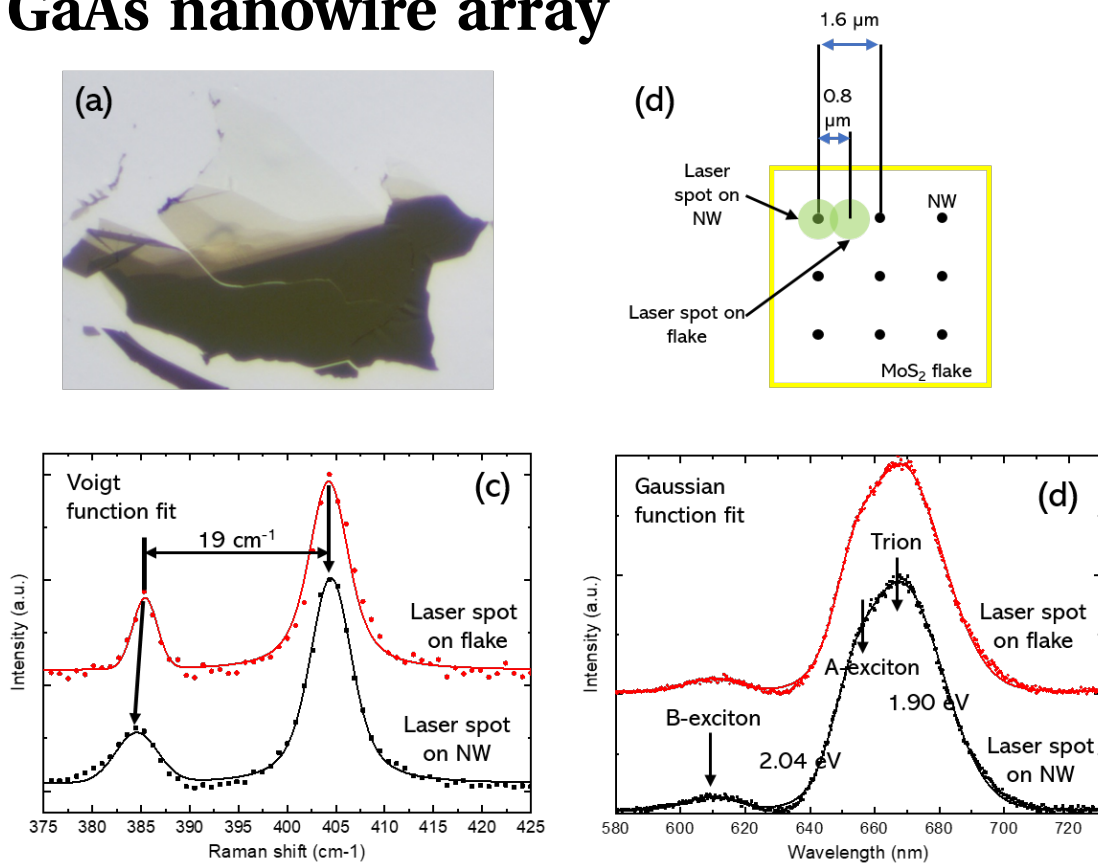


Figure C.1 – (a) Optical image of a representative MoS₂ flake exfoliated on a PDMS film. The monolayer can be identified from the optical contrast. (b) Schematic showing the laser spot location for Raman and PL point measurements. (c) and (d) Room-temperature Raman and PL spectra measured from the flake on array. The monolayer thickness is also confirmed from the frequency difference between the E₁_{2g} and A_{1g} modes (19 cm⁻¹) and the A- and B-exciton energies around 1.91 and 2.04 eV, respectively.

Appendix C. Supplementary: Spatial modulation of vibrational and luminescence properties of monolayer MoS₂ using a GaAs nanowire array

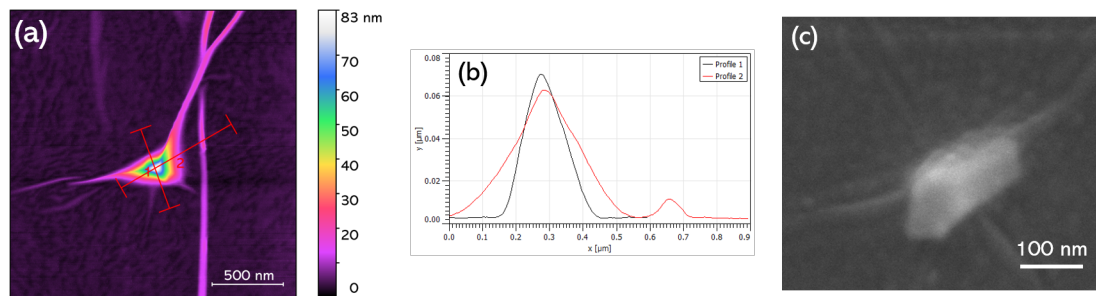


Figure C.2 – (a) AFM image and (b) linescan profiles from type-III (tent-like) NWs (c) SEM image of a tent-like NW.

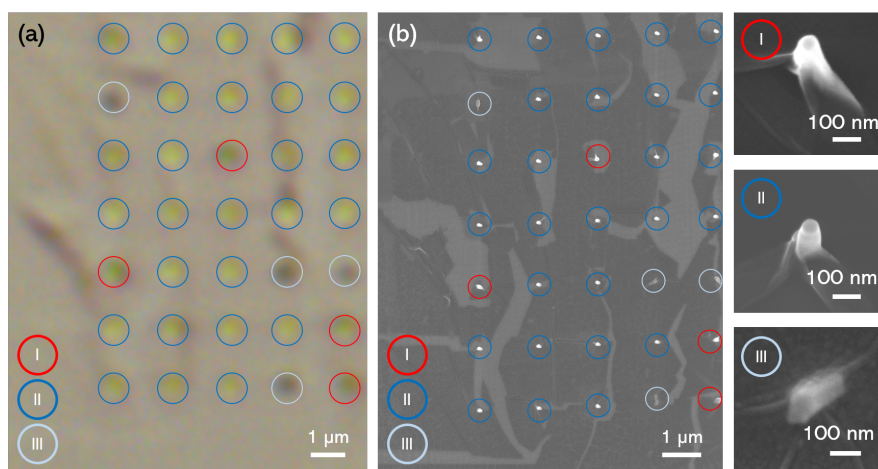


Figure C.3 – Identification of the three different types of configurations the flake adopts on top of NWs from the optical and SEM images.

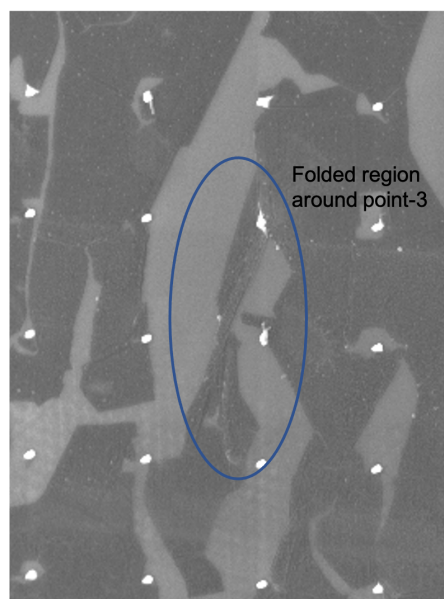


Figure C.4 – SEM image of a folded region of the flake in the vicinity of point-3.

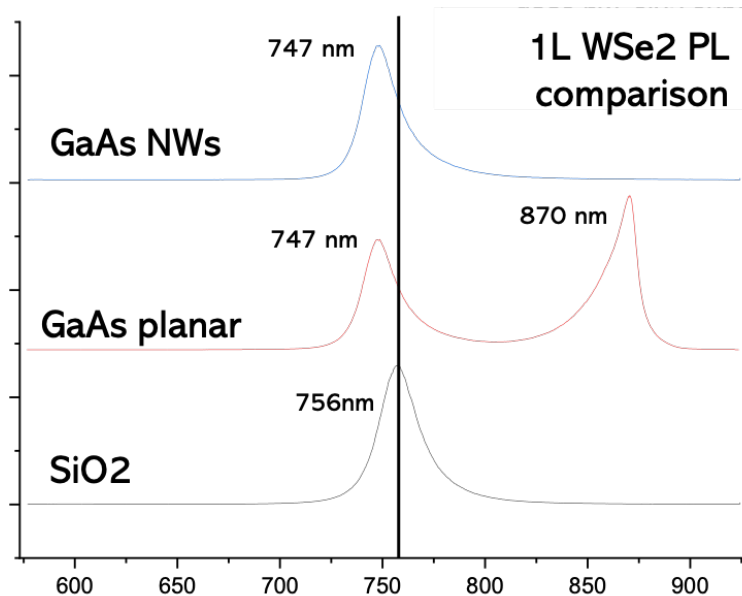


Figure C.5 – Photoluminescence spectra from a monolayer WSe₂ flake on SiO₂, planar GaAs and GaAs NW substrates. The spectra on GaAs substrates hwo a blueshift in the PL emission peak in comparison to the ML on SiO₂ substrate.

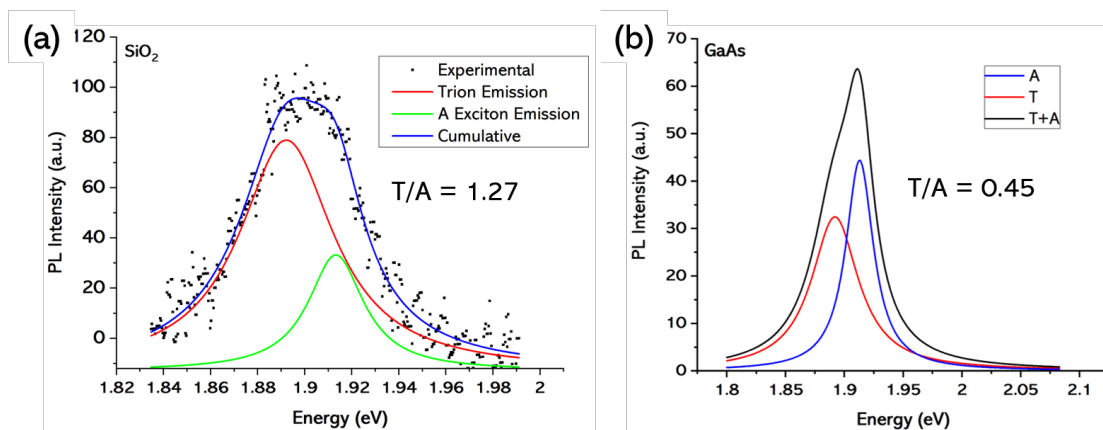


Figure C.6 – Results of Lorentzian peak fitting to the PL spectra from monolayer MoS₂ on (a) SiO₂ and (b) GaAs.

Appendix C. Supplementary: Spatial modulation of vibrational and luminescence properties of monolayer MoS₂ using a GaAs nanowire array

Table C.1 – Results of the Lorentzian fitting to the Raman spectra in figure 3(b) of the main text.

| Point | E_{2g} (cm ⁻¹) | ΔE_{2g} (cm ⁻¹) | A_{1g} (cm ⁻¹) | ΔA_{1g} (cm ⁻¹) | Δf (cm ⁻¹) | Configuration |
|---------|---------------------------------|--|---------------------------------|--|-----------------------------------|---------------|
| Ref | 385.9 | -- | 406.4 | -- | 20.5 | |
| 2 (11) | 384.8 | -1.1 | 405.5 | -0.9 | 20.7 | Wrap-around |
| 6 (3) | 386.2 | 0.3 | 406.4 | 0 | 20.2 | Wrap-around |
| 8 (8) | 385.6 | -0.3 | 405.6 | -0.8 | 20 | Wrap-around |
| 10 (10) | 384.6 | -1.3 | 406.1 | -0.3 | 21.5 | Wrap-around |
| 1 (4) | 386.2 | 0.3 | 406.6 | 0.2 | 20.4 | Pierced |
| 5 (7) | 386.1 | 0.2 | 407.4 | 1 | 21.3 | Pierced |
| 9 (9) | 385.2 | -0.7 | 405.4 | -1 | 20.2 | Pierced |
| 11 | 384.8 | -1.1 | 405.5 | -0.9 | 20.7 | Tent-like |
| 12 | 385.2 | -0.7 | 405.7 | -0.7 | 20.5 | Tent-like |
| 13 | 385.3 | -0.6 | 405.5 | -0.9 | 20.2 | Tent-like |
| 14 | 385.2 | -0.7 | 405.2 | -1.2 | 20 | Tent-like |
| 3 (5) | 384.4 | -1.5 | 406.9 | 0.5 | 22.5 | Multilayer |
| 4 (6) | 385.6 | -0.3 | 407.2 | 0.8 | 21.6 | Multilayer |
| 7 (2) | 385.1 | -0.8 | 407.4 | 1 | 22.3 | Multilayer |

D InAs growth on GaAs nanoneedles

Here we present the initial experiments on the deposition of InAs on top of thin GaAs nanoneedles (NNs). The InAs clusters, with a high In content, accumulated on top of the NNs. The size of these InAs clusters is ~ 20 nm. By embedding these InAs clusters on NNs into a shell, fully quantum-confined axial QDs could be obtained.

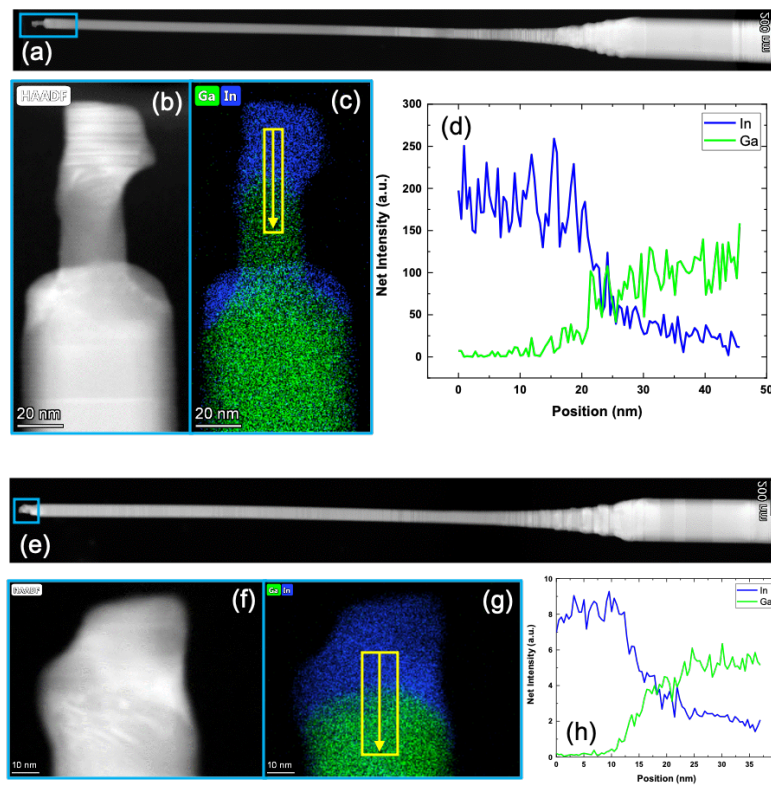


Figure D.1 – STEM-EDX of two NN structures with InAs clusters on top. (a),(e) Overview HAADF image of two GaAs NNs; (b),(f) Magnified HAADF image of the tip of the NNs; (c),(g) STEM-EDX image of the tips shown in (b) and (f) showing the In and Ga composition of the NNs and (d),(h) Line scans along the direction indicated in (c) and (g), respectively.

Bibliography

- [1] Pascale Senellart, Glenn Solomon, and Andrew White. High-performance semiconductor quantum-dot single-photon sources. *Nat. Nanotechnol.*, 12(11):1026–1039, 2017.
- [2] Kamyar Parto, Shaimaa I. Azzam, Kaustav Banerjee, and Galan Moody. Defect and strain engineering of monolayer WSe₂ enables site-controlled single-photon emission up to 150 K. *Nature Communications*, 12(1):1–8, 2021.
- [3] P. E. Faria Junior and G. M. Sipahi. Band structure calculations of InP wurtzite/zinc-blende quantum wells. *Journal of Applied Physics*, 112(10):103716, nov 2012.
- [4] Federico Panciera, Zhaslan Baraissov, Gilles Patriarche, Vladimir G Dubrovskii, Frank Glas, Laurent Travers, Utkur Mirsaidov, and Jean-christophe Harmand. Phase Selection in Self-catalyzed GaAs Nanowires. *Nano Letters*, page acs.nanolett.9b04808, feb 2020.
- [5] Andrea Splendiani, Liang Sun, Yuanbo Zhang, Tianshu Li, Jonghwan Kim, Chi Yung Chim, Giulia Galli, and Feng Wang. Emerging photoluminescence in monolayer MoS₂. *Nano Lett.*, 10(4):1271–1275, 2010.
- [6] Changgu Lee, Huguen Yan, Louis E. Brus, Tony F. Heinz, James Hone, and Sunmin Ryu. Anomalous Lattice Vibrations of Single- and Few-Layer MoS₂. *ACS Nano*, 4(5):2695–2700, may 2010.
- [7] Hiram J. Conley, Bin Wang, Jed I. Ziegler, Richard F Haglund, Sokrates T. Pantelides, and Kirill I. Bolotin. Bandgap engineering of strained monolayer and bilayer MoS₂. *Nano Letters*, 13(8):3626–3630, aug 2013.
- [8] Yanlong Wang, Chunxiao Cong, Weihuang Yang, Jingzhi Shang, Namphung Peimyoo, Yu Chen, Junyong Kang, Jianpu Wang, Wei Huang, and Ting Yu. Strain-induced direct–indirect bandgap transition and phonon modulation in monolayer WS₂. *Nano Research*, 8(8):2562–2572, aug 2015.
- [9] Yeung Yu Hui, Xiaofei Liu, Wenjing Jie, Ngai Yui Chan, Jianhua Hao, Yu-Te Hsu, Lain-Jong Li, Wanlin Guo, and Shu Ping Lau. Exceptional Tunability of Band Energy in a Compressively Strained Trilayer MoS₂ Sheet. *ACS Nano*, 7(8):7126–7131, aug 2013.

Bibliography

- [10] V. Ongun Özçelik, Javad G. Azadani, Ce Yang, Steven J. Koester, and Tony Low. Band alignment of two-dimensional semiconductors for designing heterostructures with momentum space matching. *Phys. Rev. B*, 94(3), 2016.
- [11] Yinghui Sun, Kai Liu, Xiaoping Hong, Michelle Chen, Jonghwan Kim, Sufei Shi, Junqiao Wu, Alex Zettl, and Feng Wang. Probing Local Strain at MX₂–Metal Boundaries with Surface Plasmon-Enhanced Raman Scattering. *Nano Lett.*, 14(9):5329–5334, sep 2014.
- [12] Haiqing Zhou, Fang Yu, Chuan Fei Guo, Zongpeng Wang, Yucheng Lan, Gang Wang, Zheyu Fang, Yuan Liu, Shuo Chen, Lianfeng Sun, and Zhifeng Ren. Well-oriented epitaxial gold nanotriangles and bowties on MoS₂ for surface-enhanced Raman scattering. *Nanoscale*, 7(20):9153–9157, 2015.
- [13] Wen Chen, Shunping Zhang, Meng Kang, Weikang Liu, Zhenwei Ou, Yang Li, Yexin Zhang, Zhiqiang Guan, and Hongxing Xu. Probing the limits of plasmonic enhancement using a two-dimensional atomic crystal probe. *Light Sci. Appl.*, 7(1), 2018.
- [14] Kirstin Schauble, Dante Zakhidov, Eilam Yalon, Sanchit Deshmukh, Ryan W. Grady, Kayla A. Cooley, Connor J. McClellan, Sam Vaziri, Donata Passarello, Suzanne E. Mohny, Michael F. Toney, A. K. Sood, Alberto Salleo, and Eric Pop. Uncovering the effects of metal contacts on monolayer MoS₂. *ACS Nano*, 14(11):14798–14808, 2020.
- [15] Matěj Velický, Alvaro Rodriguez, Milan Bouša, Andrey V. Krayev, Martin Vondráček, Jan Honolka, Mahdi Ahmadi, Gavin E. Donnelly, Fumin Huang, Héctor D. Abrunã, Kostya S. Novoselov, and Otakar Frank. Strain and Charge Doping Fingerprints of the Strong Interaction between Monolayer MoS₂ and Gold. *J. Phys. Chem. Lett.*, 11(15):6112–6118, 2020.
- [16] David Lloyd, Xinghui Liu, Jason W. Christopher, Lauren Cantley, Anubhav Wadehra, Brian L. Kim, Bennett B. Goldberg, Anna K. Swan, and J. Scott Bunch. Band Gap Engineering with Ultralarge Biaxial Strains in Suspended Monolayer MoS₂. *Nano Lett.*, 16(9):5836–5841, 2016.
- [17] Biswanath Chakraborty, Achintya Bera, D. V. S. Muthu, Somnath Bhowmick, U. V. Waghmare, and A. K. Sood. Symmetry-dependent phonon renormalization in monolayer MoS₂ transistor. *Phys. Rev. B*, 85(16):161403, apr 2012.
- [18] Bastian Miller, Eric Parzinger, Anna Vernickel, Alexander W. Holleitner, and Ursula Wurstbauer. Photogating of mono- and few-layer MoS₂. *Appl. Phys. Lett.*, 106(12):122103, mar 2015.
- [19] Hsiang-Lin Liu, Huaihong Guo, Teng Yang, Zhidong Zhang, Yasuaki Kumamoto, Chih-Chiang Shen, Yu-Te Hsu, Lain-Jong Li, Riichiro Saito, and Satoshi Kawata. Anomalous lattice vibrations of monolayer MoS₂ probed by ultraviolet Raman scattering. *Phys. Chem. Chem. Phys.*, 17(22):14561–14568, 2015.

-
- [20] Hong Li, Alex W. Contryman, Xiaofeng Qian, Sina Moeini Ardakani, Yongji Gong, Xingli Wang, Jeffrey M. Weisse, Chi Hwan Lee, Jiheng Zhao, Pulickel M. Ajayan, Ju Li, Hari C. Manoharan, and Xiaolin Zheng. Optoelectronic crystal of artificial atoms in strain-textured molybdenum disulphide. *Nat. Commun.*, 6(1):7381, nov 2015.
- [21] Bruno R. Carvalho, Yuanxi Wang, Sandro Mignuzzi, Debdulal Roy, Mauricio Terrones, Cristiano Fantini, Vincent H. Crespi, Leandro M. Malard, and Marcos A. Pimenta. Intervalley scattering by acoustic phonons in two-dimensional MoS₂ revealed by double-resonance Raman spectroscopy. *Nature Communications*, 8(1):14670, apr 2017.
- [22] Zhores I. Alferov. The double heterostructure: Concept and its applications in physics, electronics and technology. *International Journal of Modern Physics B*, 16(5):647–675, 2002.
- [23] Stefan Strauf, Nick G. Stoltz, Matthew T. Rakher, Larry A. Coldren, Pierre M. Petroff, and Dirk Bouwmeester. High-frequency single-photon source with polarization control. *Nature Photonics*, 1(12):704–708, 2007.
- [24] Julien Claudon, Joël Bleuse, Nitin Singh Malik, Maela Bazin, Périne Jaffrennou, Niels Gregersen, Christophe Sauvan, Philippe Lalanne, and Jean Michel Gérard. A highly efficient single-photon source based on a quantum dot in a photonic nanowire. *Nature Photonics*, 4(3):174–177, 2010.
- [25] Michael E. Reimer, Gabriele Bulgarini, Nika Akopian, Moïra Hocevar, Maaïke Bouwes Bavinck, Marcel A. Verheijen, Erik P A M Bakkers, Leo P. Kouwenhoven, and Val Zwiller. Bright single-photon sources in bottom-up tailored nanowires. *Nature Communications*, 3, 2012.
- [26] Natasha Tamm, Alisa Javadi, Nadia Olympia Antoniadis, Daniel Najer, Matthias Christian Löbl, Alexander Rolf Korsch, Rüdiger Schott, Sascha René Valentin, Andreas Dirk Wieck, Arne Ludwig, and Richard John Warburton. A bright and fast source of coherent single photons. *Nature Nanotechnology*, 16(4):399–403, apr 2021.
- [27] I. Friedler, C. Sauvan, J. P. Hugonin, P. Lalanne, J. Claudon, and J. M. Gérard. Solid-state single photon sources: the nanowire antenna. *Optics Express*, 17(4):2095, 2009.
- [28] J. Klein, M. Lorke, M. Florian, F. Sigger, L. Sigl, S. Rey, J. Wierzbowski, J. Cerne, K. Müller, E. Mitterreiter, P. Zimmermann, T. Taniguchi, K. Watanabe, U. Wurstbauer, M. Kaniber, M. Knap, R. Schmidt, J. J. Finley, and A. W. Holleitner. Site-selectively generated photon emitters in monolayer MoS₂ via local helium ion irradiation. *Nat. Commun.*, 10(1), jan 2019.
- [29] Ajit Srivastava, Meinrad Sidler, Adrien V. Allain, Dominik S. Lembke, Andras Kis, and A. Imamoglu. Optically active quantum dots in monolayer WSe₂. *Nature Nanotechnology*, 10(6):491–496, 2015.

Bibliography

- [30] Yu-Ming He, Genevieve Clark, John R. Schaibley, Yu He, Ming-Cheng Chen, Yu-Jia Wei, Xing Ding, Qiang Zhang, Wang Yao, Xiaodong Xu, Chao-Yang Lu, and Jian-Wei Pan. Single quantum emitters in monolayer semiconductors. *Nature Nanotechnology*, 10(6):497–502, jun 2015.
- [31] M. Koperski, K. Nogajewski, A. Arora, V. Cherkez, P. Mallet, J.-Y. Veuillen, J. Marcus, P. Kossacki, and M. Potemski. Single photon emitters in exfoliated WSe₂ structures. *Nature Nanotechnology*, 10(6):503–506, jun 2015.
- [32] Chitraleema Chakraborty, Laura Kinnischtzke, Kenneth M. Goodfellow, Ryan Beams, and A. Nick Vamivakas. Voltage-controlled quantum light from an atomically thin semiconductor. *Nature Nanotechnology*, 10(6):507–511, jun 2015.
- [33] Toan Trong Tran, Kerem Bray, Michael J. Ford, Milos Toth, and Igor Aharonovich. Quantum emission from hexagonal boron nitride monolayers. *Nature Nanotechnology*, 11(1):37–41, 2016.
- [34] Carmen Palacios-Berraquero, Dhiren M. Kara, Alejandro R.P. Montblanch, Matteo Barbone, Pawel Latawiec, Duhee Yoon, Anna K. Ott, Marko Loncar, Andrea C. Ferrari, and Mete Atatüre. Large-scale quantum-emitter arrays in atomically thin semiconductors. *Nature Communications*, 8(May):1–6, aug 2017.
- [35] Artur Branny, Santosh Kumar, Raphaël Proux, and Brian D. Gerardot. Deterministic strain-induced arrays of quantum emitters in a two-dimensional semiconductor. *Nature Communications*, 8(May):1–7, 2017.
- [36] Shaimaa I. Azzam, Kamyar Parto, and Galan Moody. Prospects and challenges of quantum emitters in 2D materials. *Applied Physics Letters*, 118(24), 2021.
- [37] Riccardo Frisenda, Efrén Navarro-Moratalla, Patricia Gant, David Pérez De Lara, Pablo Jarillo-Herrero, Roman V. Gorbachev, and Andres Castellanos-Gomez. Recent progress in the assembly of nanodevices and van der Waals heterostructures by deterministic placement of 2D materials. *Chemical Society Reviews*, 47(1):53–68, 2018.
- [38] Keith R. Paton and Jonathan N. Coleman. Relating the optical absorption coefficient of nanosheet dispersions to the intrinsic monolayer absorption. *Carbon*, 107:733–738, oct 2016.
- [39] Yasir J. Noori, Yameng Cao, Jonathan Roberts, Christopher Woodhead, Ramon Bernardo-Gavito, Peter Tovee, and Robert J. Young. Photonic Crystals for Enhanced Light Extraction from 2D Materials. *ACS Photonics*, 3(12):2515–2520, dec 2016.
- [40] M. Grundmann, J. Christen, N. N. Ledentsov, J. Böhrer, D. Bimberg, S. S. Ruvimov, P. Werner, U. Richter, U. Gösele, J. Heydenreich, V. M. Ustinov, A. Yu Egorov, A. E. Zhukov, P. S. Kop’Ev, and Zh I. Alferov. Ultranarrow luminescence lines from single quantum dots. *Phys. Rev. Lett.*, 74(20):4043–4046, 1995.

-
- [41] K. H. Schmidt, G. Medeiros-Ribeiro, J. Garcia, and P. M. Petroff. Size quantization effects in InAs self-assembled quantum dots. *Applied Physics Letters*, 70(13):1727–1729, mar 1997.
- [42] Daniel Huber, Marcus Reindl, Johannes Aberl, Armando Rastelli, and Rinaldo Trotta. Semiconductor quantum dots as an ideal source of polarization-entangled photon pairs on-demand: A review. *Journal of Optics (United Kingdom)*, 20(7):1–18, jul 2018.
- [43] D C Unitt, A J Bennett, P Atkinson, K Cooper, P See, D Gevaux, M B Ward, R M Stevenson, D A Ritchie, and A J Shields. Quantum dots as single-photon sources for quantum information processing. *J. Opt. B Quantum Semiclassical Opt.*, 7(7):S129–S134, jul 2005.
- [44] Igor Aharonovich, Dirk Englund, and Milos Toth. Solid-state single-photon emitters. *Nature Photonics*, 10(10):631–641, 2016.
- [45] Christof P. Dietrich, Andrea Fiore, Mark G. Thompson, Martin Kamp, and Sven Höfling. GaAs integrated quantum photonics: Towards compact and multi-functional quantum photonic integrated circuits. *Laser Photonics Rev.*, 10(6):870–894, 2016.
- [46] S. Bogdanov, M. Y. Shalaginov, A. Boltasseva, and V. M. Shalaev. Material platforms for integrated quantum photonics. *Opt. Mater. Express*, 7(1):111, jan 2017.
- [47] R. Rossetti, S. Nakahara, and L. E. Brus. Quantum size effects in the redox potentials, resonance Raman spectra, and electronic spectra of CdS crystallites in aqueous solution. *J. Chem. Phys.*, 79(2):1086–1088, 1983.
- [48] Jinwook Lee, Vikram C. Sundar, Jason R. Heine, Mouni G. Bawendi, and Klavs F. Jensen. Full Color Emission from $\text{II} \pm \text{VI}$ Semiconductor. *Adv. Mater.*, 12(15):1102–1105, 2000.
- [49] M. G. C. B. Murray and C. R. Kagan, Bawendi. SYNTHESIS AND CHARACTERIZATION OF MONODISPERSE NANOCRYSTALS AND CLOSE-PACKED NANOCRYSTAL ASSEMBLIES. *Annu. Rev. Mater. Sci.*, 30(June):545–610, 2006.
- [50] D. Leonard, M. Krishnamurthy, C. M. Reaves, S. P. Denbaars, and P. M. Petroff. Direct formation of quantum-sized dots from uniform coherent islands of InGaAs on GaAs surfaces. *Appl. Phys. Lett.*, 63(23):3203–3205, 1993.
- [51] Peter Y. Yu and Manuel Cardona. *Fundamentals of Semiconductors*. Graduate Texts in Physics. Springer Berlin Heidelberg, Berlin, Heidelberg, 2010.
- [52] Richard J. Warburton. Single spins in self-assembled quantum dots. *Nature Materials*, 12(6):483–493, 2013.
- [53] A. Huggenberger, C. Schneider, C. Drescher, S. Heckelmann, T. Heindel, S. Reitzenstein, M. Kamp, S. Höfling, L. Worschech, and A. Forchel. Site-controlled In(Ga)As/GaAs quantum dots for integration into optically and electrically operated devices. *Journal of Crystal Growth*, 323(1):194–197, may 2011.

Bibliography

- [54] Stephane Faure, Masao Nishioka, Satomi Ishida, Denis Guimard, and Yasuhiko Arakawa. Metal Organic Chemical Vapor Deposition Growth of High Spectral Quality Site-Controlled InAs Quantum Dots Using In situ Patterning. *Appl. Phys. Express*, 4(11):112001, nov 2011.
- [55] Michael K. Yakes, Lily Yang, Allan S. Bracker, Timothy M. Sweeney, Peter G. Brereton, Mijin Kim, Chul Soo Kim, Patrick M. Vora, Doewon Park, Samuel G. Carter, and Daniel Gammon. Leveraging Crystal Anisotropy for Deterministic Growth of InAs Quantum Dots with Narrow Optical Linewidths. *Nano Lett.*, 13(10):4870–4875, oct 2013.
- [56] Y. H. Huo, A. Rastelli, and O. G. Schmidt. Ultra-small excitonic fine structure splitting in highly symmetric quantum dots on GaAs (001) substrate. *Appl. Phys. Lett.*, 102(15):152105, apr 2013.
- [57] M. H. Baier, S. Watanabe, E. Pelucchi, and E. Kapon. High uniformity of site-controlled pyramidal quantum dots grown on prepatterned substrates. *Appl. Phys. Lett.*, 84(11):1943–1945, 2004.
- [58] J. Tommila, A. Tukiainen, J. Viheriälä, A. Schramm, T. Hakkarainen, A. Aho, P. Stenberg, M. Dumitrescu, and M. Guina. Nanoimprint lithography patterned GaAs templates for site-controlled InAs quantum dots. *J. Cryst. Growth*, 323(1):183–186, may 2011.
- [59] S. Ishida, Y. Arakawa, and K. Wada. Seeded self-assembled GaAs quantum dots grown in two-dimensional V grooves by selective metal–organic chemical-vapor deposition. *Applied Physics Letters*, 72(7):800–802, feb 1998.
- [60] J. M. Gérard, B. Sermage, B. Gayral, B. Legrand, E. Costard, and V. Thierry-Mieg. Enhanced spontaneous emission by quantum boxes in a monolithic optical microcavity. *Physical Review Letters*, 81(5):1110–1113, 1998.
- [61] N. Somaschi, V. Giesz, L. De Santis, J. C. Loredó, M. P. Almeida, G. Hornecker, S. L. Portalupi, T. Grange, C. Antón, J. Demory, C. Gómez, I. Sagnes, N. D. Lanzillotti-Kimura, A. Lemaître, A. Auffeves, A. G. White, L. Lanco, and P. Senellart. Near-optimal single-photon sources in the solid state. *Nature Photonics*, 10(5):340–345, 2016.
- [62] E. Peter, P. Senellart, D. Martrou, A. Lemaître, J. Hours, J. M. Gérard, and J. Bloch. Exciton-photon strong-coupling regime for a single quantum dot embedded in a microcavity. *Physical Review Letters*, 95(6):1–4, 2005.
- [63] D. G. Gevaux, A. J. Bennett, R. M. Stevenson, A. J. Shields, P. Atkinson, J. Griffiths, D. Anderson, G. A.C. Jones, and D. A. Ritchie. Enhancement and suppression of spontaneous emission by temperature tuning InAs quantum dots to photonic crystal cavities. *Applied Physics Letters*, 88(13):3–6, 2006.
- [64] T. Lund-Hansen, S. Stobbe, B. Julsgaard, H. Thyrrestrup, T. Sünner, M. Kamp, A. Forchel, and P. Lodahl. Experimental realization of highly efficient broadband coupling of single

- quantum dots to a photonic crystal waveguide. *Physical Review Letters*, 101(11):1–4, 2008.
- [65] Niels Gregersen, Torben Roland Nielsen, Jesper Mørk, Julien Claudon, and Jean-Michel Gérard. Designs for high-efficiency electrically pumped photonic nanowire single-photon sources. *Optics Express*, 18(20):21204, 2010.
- [66] R. S. Wagner and W. C. Ellis. Vapor-liquid-solid mechanism of single crystal growth. *Applied Physics Letters*, 4(5):89–90, 1964.
- [67] A. Fontcuberta I Morral, C. Colombo, G. Abstreiter, J. Arbiol, and J. R. Morante. Nucleation mechanism of gallium-assisted molecular beam epitaxy growth of gallium arsenide nanowires. *Applied Physics Letters*, 92(6), 2008.
- [68] Sébastien Plissard, Kimberly A. Dick, Guilhem Larrieu, Sylvie Godey, Ahmed Addad, Xavier Wallart, and Philippe Caroff. Gold-free growth of GaAs nanowires on silicon: Arrays and polytypism. *Nanotechnology*, 21(38), 2010.
- [69] Katsuhiro Tomioka, Keitaro Ikejiri, Tomotaka Tanaka, Junichi Motohisa, Shinjiro Hara, Kenji Hiruma, and Takashi Fukui. Selective-area growth of III-V nanowires and their applications. *J. Mater. Res.*, 26(17):2127–2141, sep 2011.
- [70] C. B. Roxlo, B. Abeles, and T. Tiedje. Evidence for Lattice-Mismatch—Induced Defects in Amorphous Semiconductor Heterojunctions. *Physical Review Letters*, 52(22):1994–1997, may 1984.
- [71] Magnus W. Larsson, Jakob B. Wagner, Mathias Wallin, Paul Håkansson, Linus E. Fröberg, Lars Samuelson, and L. Reine Wallenberg. Strain mapping in free-standing heterostructured wurtzite InAs/InP nanowires. *Nanotechnology*, 18(1), 2007.
- [72] Premila Mohan, Junichi Motohisa, and Takashi Fukui. Controlled growth of highly uniform, axial/radial direction-defined, individually addressable InP nanowire arrays. *Nanotechnology*, 16(12):2903–2907, dec 2005.
- [73] Frank Glas, Jean-Christophe Harmand, and Gilles Patriarche. Why Does Wurtzite Form in Nanowires of III-V Zinc Blende Semiconductors? *Physical Review Letters*, 99(14):146101, oct 2007.
- [74] A. Mishra, L. V. Titova, T. B. Hoang, H. E. Jackson, L. M. Smith, J. M. Yarrison-Rice, Y. Kim, H. J. Joyce, Q. Gao, H. H. Tan, and C. Jagadish. Polarization and temperature dependence of photoluminescence from zincblende and wurtzite InP nanowires. *Appl. Phys. Lett.*, 91(26):263104, dec 2007.
- [75] Jonas Johansson, Lisa S. Karlsson, Kimberly A. Dick, Jessica Bolinsson, Brent A. Wacaser, Knut Deppert, and Lars Samuelson. Effects of supersaturation on the crystal structure of gold seeded III-V nanowires. *Cryst. Growth Des.*, 9(2):766–773, 2009.

Bibliography

- [76] Kimberly A Dick, Philippe Caroff, Jessica Bolinsson, Maria E Messing, Jonas Johansson, Knut Deppert, L Reine Wallenberg, and Lars Samuelson. Control of III–V nanowire crystal structure by growth parameter tuning. *Semiconductor Science and Technology*, 25(2):024009, feb 2010.
- [77] T. Dursap, M. Vettori, A. Danescu, C. Botella, P. Regreny, G. Patriarche, M. Gendry, and J. Penuelas. Crystal phase engineering of self-catalyzed GaAs nanowires using a RHEED diagram. *Nanoscale Adv.*, 2(5):2127–2134, 2020.
- [78] J. Christen, D. Bimberg, A. Steckenborn, and G. Weimann. Localization induced electron-hole transition rate enhancement in GaAs quantum wells. *Appl. Phys. Lett.*, 44(1):84–86, jan 1984.
- [79] G. Strasser, S. Gianordoli, L. Hvozdar, W. Schrenk, K. Unterrainer, and E. Gornik. GaAs/AlGaAs superlattice quantum cascade lasers at $\lambda=13\text{ }\mu\text{m}$. *Appl. Phys. Lett.*, 75(10):1345–1347, sep 1999.
- [80] T. J. Rogers, D. G. Deppe, and B. G. Streetman. Effect of an AlAs/GaAs mirror on the spontaneous emission of an InGaAs-GaAs quantum well. *Applied Physics Letters*, 57(18):1858–1860, oct 1990.
- [81] B. Jonas Ohlsson, M. T. Björk, A. I. Persson, C. Thelander, L. R. Wallenberg, M. H. Magnusson, K. Deppert, and L. Samuelson. Growth and characterization of GaAs and InAs nano-whiskers and InAs/GaAs heterostructures. *Physica E: Low-Dimensional Systems and Nanostructures*, 13(2-4):1126–1130, 2002.
- [82] M. T. Björ, B. J. Ohlsson, T. Sass, A. I. Persson, C. Thelander, M. H. Magnusson, K. Deppert, L. R. Wallenberg, and L. Samuelson. One-dimensional Steeplechase for Electrons Realized. *Nano Letters*, 2(2):87–89, feb 2002.
- [83] C. P.T. Svensson, W. Seifert, M. W. Larsson, L. R. Wallenberg, J. Stangl, G. Bauer, and L. Samuelson. Epitaxially grown GaP/GaAs_{1-x}P_x/GaP double heterostructure nanowires for optical applications. *Nanotechnology*, 16(6):936–939, 2005.
- [84] Philippe Caroff, Maria E. Messing, B. Mattias Borg, Kimberly A. Dick, Knut Deppert, and Lars Erik Wernersson. InSb heterostructure nanowires: MOVPE growth under extreme lattice mismatch. *Nanotechnology*, 20(49), 2009.
- [85] Luca Francaviglia, Yannik Fontana, Anna Fontcuberta i Morral, Anna Fontcuberta i Morral, and Anna Fontcuberta i Morral. *Quantum Dots in Nanowires*, volume 94 of *Semiconductors and Semimetals*. Elsevier Inc., 1 edition, 2016.
- [86] Linus E. Fröberg, Brent A. Wacaser, Jakob B. Wagner, Sören Jeppesen, B. Jonas Ohlsson, Knut Deppert, and Lars Samuelson. Transients in the Formation of Nanowire Heterostructures. *Nano Letters*, 8(11):3815–3818, nov 2008.

-
- [87] Mohanchand Paladugu, Jin Zou, Ya Nan Guo, Graeme J. Auchterlonie, Hannah J. Joyce, Qiang Gao, H. Hoe Tan, Chennupati Jagadish, and Yong Kim. Novel growth phenomena observed in axial InAs/GaAs nanowire heterostructures. *Small*, 3(11):1873–1877, nov 2007.
- [88] Na Li, Teh Y. Tan, and U. Gösele. Transition region width of nanowire hetero- and pn-junctions grown using vapor-liquid-solid processes. *Applied Physics A*, 90(4):591–596, mar 2008.
- [89] Maria E. Messing, Jennifer Wong-Leung, Zeila Zanolli, Hannah J. Joyce, H. Hoe Tan, Qiang Gao, L. Reine Wallenberg, Jonas Johansson, and Chennupati Jagadish. Growth of straight InAs-on-GaAs nanowire heterostructures. *Nano Lett.*, 11(9):3899–3905, 2011.
- [90] Daria V. Beznasyuk, Eric Robin, Martien Den Hertog, Julien Claudon, and Moïra Hocevar. Dislocation-free axial InAs-on-GaAs nanowires on silicon. *Nanotechnology*, 28(36), 2017.
- [91] C. Y. Wen, M. C. Reuter, J. Tersoff, E. A. Stach, and F. M. Ross. Structure, growth kinetics, and ledge flow during vapor-solid-solid growth of copper-catalyzed silicon nanowires. *Nano Letters*, 10(2):514–519, 2010.
- [92] Giacomo Priante, Frank Glas, Gilles Patriarche, Konstantinos Pantzas, Fabrice Oehler, and Jean Christophe Harmand. Sharpening the Interfaces of Axial Heterostructures in Self-Catalyzed AlGaAs Nanowires: Experiment and Theory. *Nano Lett.*, 16(3):1917–1924, 2016.
- [93] Martin Heiß, Anders Gustafsson, Sonia Conesa-Boj, Francesca Peiró, Joan Ramon Morante, G. Abstreiter, Jordi Arbiol, Lars Samuelson, and Anna Fontcuberta I Morral. Catalyst-free nanowires with axial $\text{In}_x\text{Ga}_{1-x}\text{As}/\text{GaAs}$ heterostructures. *Nanotechnology*, 20(7):075603, feb 2009.
- [94] Martin Heiss, Bernt Ketterer, Emanuele Uccelli, Joan Ramon Morante, Jordi Arbiol, and Anna Fontcuberta I. Morral. In(Ga)As quantum dot formation on group-III assisted catalyst-free InGaAs nanowires. *Nanotechnology*, 22(19), 2011.
- [95] David Scarpellini, Claudio Somaschini, Alexey Fedorov, Sergio Bietti, Cesare Frigeri, Vincenzo Grillo, Luca Esposito, Marco Salvalaglio, Anna Marzegalli, Francesco Montalenti, Emiliano Bonera, Pier Gianni Medaglia, and Stefano Sanguinetti. InAs/GaAs Sharply Defined Axial Heterostructures in Self-Assisted Nanowires. *Nano Lett.*, 15(6):3677–3683, jun 2015.
- [96] Takeshi Noda, Takaaki Mano, and Hiroyuki Sakaki. Anisotropic Diffusion of In Atoms from an In Droplet and Formation of Elliptically Shaped InAs Quantum Dot Clusters on (100) GaAs. *Cryst. Growth Des.*, 11(3):726–728, mar 2011.
- [97] G. Priante, S. Ambrosini, V. G. Dubrovskii, A. Franciosi, and S. Rubini. Stopping and Resuming at Will the Growth of GaAs Nanowires. *Crystal Growth & Design*, 13(9):3976–3984, sep 2013.

Bibliography

- [98] K. S. Novoselov. Electric Field Effect in Atomically Thin Carbon Films. *Science* (80, 306(5696):666–669, oct 2004.
- [99] Zhong Lin, Bruno R. Carvalho, Ethan Kahn, Ruitao Lv, Rahul Rao, Humberto Terrones, Marcos A. Pimenta, and Mauricio Terrones. Defect engineering of two-dimensional transition metal dichalcogenides. *2D Mater.*, 3(2), 2016.
- [100] Shanshan Wang, Alex Robertson, and Jamie H. Warner. Atomic structure of defects and dopants in 2D layered transition metal dichalcogenides. *Chem. Soc. Rev.*, 47(17):6764–6794, 2018.
- [101] Ping-Heng Tan, editor. *Raman Spectroscopy of Two-Dimensional Materials*, volume 276 of *Springer Series in Materials Science*. Springer Singapore, Singapore, 2019.
- [102] Biswanath Chakraborty, Achintya Bera, D. V.S. Muthu, Somnath Bhowmick, U. V. Waghmare, and A. K. Sood. Symmetry-dependent phonon renormalization in monolayer MoS₂ transistor. *Physical Review B - Condensed Matter and Materials Physics*, 85(16):2–5, apr 2012.
- [103] Rafael Roldán, Andrés Castellanos-Gomez, Emmanuele Cappelluti, and Francisco Guinea. Strain engineering in semiconducting two-dimensional crystals. *Journal of Physics Condensed Matter*, 27(31), 2015.
- [104] Simone Bertolazzi, Jacopo Brivio, and Andras Kis. Stretching and Breaking of Ultrathin MoS₂. *ACS Nano*, 5(12):9703–9709, dec 2011.
- [105] A. A. Griffith. VI. The phenomena of rupture and flow in solids. *Philos. Trans. R. Soc. London. Ser. A, Contain. Pap. a Math. or Phys. Character*, 221(582-593):163–198, jan 1921.
- [106] Zhiwei Peng, Xiaolin Chen, Yulong Fan, David J. Srolovitz, and Dangyuan Lei. Strain engineering of 2D semiconductors and graphene: from strain fields to band-structure tuning and photonic applications. *Light: Science and Applications*, 9(1), 2020.
- [107] G. Plechinger, F.-X. Schrettenbrunner, J. Eroms, D. Weiss, C. Schüller, and T. Korn. Low-temperature photoluminescence of oxide-covered single-layer MoS₂. *physica status solidi (RRL) - Rapid Research Letters*, 6(3):126–128, mar 2012.
- [108] Andres Castellanos-Gomez, Rafael Roldán, Emmanuele Cappelluti, Michele Buscema, Francisco Guinea, Herre S.J. Van Der Zant, and Gary A. Steele. Local strain engineering in atomically thin MoS₂. *Nano Letters*, 13(11):5361–5366, 2013.
- [109] Sujay B. Desai, Gyungseon Seol, Jeong Seuk Kang, Hui Fang, Corsin Battaglia, Rehan Kapadia, Joel W. Ager, Jing Guo, and Ali Javey. Strain-induced indirect to direct bandgap transition in multilayer WSe₂. *Nano Letters*, 14(8):4592–4597, 2014.

- [110] S. Kumar, A. Kaczmarczyk, and B. D. Gerardot. Strain-Induced Spatial and Spectral Isolation of Quantum Emitters in Mono- and Bilayer WSe₂. *Nano Letters*, 15(11):7567–7573, nov 2015.
- [111] Won Seok Yun, S. W. Han, Soon Cheol Hong, In Gee Kim, and J. D. Lee. Thickness and strain effects on electronic structures of transition metal dichalcogenides: 2H- M_2X semiconductors ($\text{M} = \text{Mo, W}$). *Phys. Rev. B*, 85(3):033305, jan 2012.
- [112] Ji Feng, Xiaofeng Qian, Cheng-Wei Huang, and Ju Li. Strain-engineered artificial atom as a broad-spectrum solar energy funnel. *Nature Photonics*, 6(12):866–872, dec 2012.
- [113] Laxmi Narayan Tripathi, Oliver Iff, Simon Betzold, Łukasz Dusanowski, Monika Emerling, Kihwan Moon, Young Jin Lee, Soon-Hong Kwon, Sven Höfling, and Christian Schneider. Spontaneous Emission Enhancement in Strain-Induced WSe₂ Monolayer-Based Quantum Light Sources on Metallic Surfaces. *ACS Photonics*, 5(5):1919–1926, may 2018.
- [114] Santosh Kumar, Mauro Brotóns-Gisbert, Rima Al-Khuzheyri, Artur Branny, Guillem Ballesteros-Garcia, Juan F. Sánchez-Royo, and Brian D. Gerardot. Resonant laser spectroscopy of localized excitons in monolayer WSe₂. *Optica*, 3(8):882, 2016.
- [115] Chandriker Kavir Dass, Mahtab A. Khan, Genevieve Clark, Jeffrey A. Simon, Ricky Gibson, Shin Mou, Xiaodong Xu, Michael N. Leuenberger, and Joshua R. Hendrickson. Ultra-Long Lifetimes of Single Quantum Emitters in Monolayer WSe₂ /hBN Heterostructures. *Adv. Quantum Technol.*, 2(5-6):1900022, jun 2019.
- [116] Carmen Palacios-Berraquero, Matteo Barbone, Dhiren M. Kara, Xiaolong Chen, Ilya Goykhman, Duhee Yoon, Anna K. Ott, Jan Beitner, Kenji Watanabe, Takashi Taniguchi, Andrea C. Ferrari, and Mete Atatüre. Atomically thin quantum light-emitting diodes. *Nat. Commun.*, 7(1):12978, dec 2016.
- [117] Leo Yu, Minda Deng, Jingyuan Linda Zhang, Sven Borghardt, Beata Kardynal, Jelena Vučković, and Tony F. Heinz. Site-Controlled Quantum Emitters in Monolayer MoSe₂. *Nano Lett.*, 21(6):2376–2381, 2021.
- [118] Chitraleema Chakraborty, Kenneth M. Goodfellow, and A. Nick Vamivakas. Localized emission from defects in MoSe₂ layers. *Opt. Mater. Express*, 6(6):2081, jun 2016.
- [119] Artur Branny, Gang Wang, Santosh Kumar, Cedric Robert, Benjamin Lassagne, Xavier Marie, Brian D. Gerardot, and Bernhard Urbaszek. Discrete quantum dot like emitters in monolayer MoSe₂: Spatial mapping, magneto-optics, and charge tuning. *Appl. Phys. Lett.*, 108(14), 2016.
- [120] K. Barthelmi, J. Klein, A. Hötger, L. Sigl, F. Sigger, E. Mitterreiter, S. Rey, S. Gyger, M. Lorke, M. Florian, F. Jahnke, T. Taniguchi, K. Watanabe, V. Zwiller, K. D. Jöns, U. Wurstbauer,

Bibliography

- C. Kastl, A. Weber-Bargioni, J. J. Finley, K. Müller, and A. W. Holleitner. Atomistic defects as single-photon emitters in atomically thin MoS₂. *Appl. Phys. Lett.*, 117(7):070501, aug 2020.
- [121] Chitrалеema Chakraborty, Nick Vamivakas, and Dirk Englund. Advances in quantum light emission from 2D materials. *Nanophotonics*, 2019.
- [122] Oliver Iff, Yu-Ming He, Nils Lundt, Sebastian Stoll, Vasilij Baumann, Sven Höfling, and Christian Schneider. Substrate engineering for high-quality emission of free and localized excitons from atomic monolayers in hybrid architectures. *Optica*, 4(6):669, jun 2017.
- [123] Kin Fai Mak, Keliang He, Changgu Lee, Gwan Hyoung Lee, James Hone, Tony F. Heinz, and Jie Shan. Tightly bound trions in monolayer MoS₂. *Nat. Mater.*, 12(3):207–211, mar 2013.
- [124] G. Wang, L. Bouet, D. Lagarde, M. Vidal, A. Balocchi, T. Amand, X. Marie, and B. Urbaszek. Valley dynamics probed through charged and neutral exciton emission in monolayer WSe₂. *Phys. Rev. B - Condens. Matter Mater. Phys.*, 90(7):1–6, 2014.
- [125] Xin Lu, Xiaotong Chen, Sudipta Dubey, Qiang Yao, Weijie Li, Xingzhi Wang, Qihua Xiong, and Ajit Srivastava. Optical initialization of a single spin-valley in charged WSe₂ quantum dots. *Nat. Nanotechnol.*, 14(5):426–431, may 2019.
- [126] A. Chaves, J. G. Azadani, Hussain Als Salman, D. R. da Costa, R. Frisenda, A. J. Chaves, Seung Hyun Song, Y. D. Kim, Daowei He, Jiadong Zhou, A. Castellanos-Gomez, F. M. Peeters, Zheng Liu, C. L. Hinkle, Sang Hyun Oh, Peide D. Ye, Steven J. Koester, Young Hee Lee, Ph Avouris, Xinran Wang, and Tony Low. Bandgap engineering of two-dimensional semiconductor materials. *npj 2D Mater. Appl.*, 4(1), 2020.
- [127] Jesús Herranz, Pierre Corfdir, Esperanza Luna, Uwe Jahn, Ryan B. Lewis, Lutz Schrottke, Jonas Lähnemann, Abbas Tahraoui, Achim Trampert, Oliver Brandt, and Lutz Geelhaar. Coaxial GaAs/(In,Ga)As dot-in-a-well nanowire heterostructures for electrically driven infrared light generation on Si in the telecommunication O band. *ACS Applied Nano Materials*, 3(1):1–19, jan 2019.
- [128] A. Y. Cho and W. C. Ballamy. GaAs planar technology by molecular beam epitaxy (MBE). *Journal of Applied Physics*, 46(2):783–785, feb 1975.
- [129] Seongjoon Ahn, Gwangwoo Kim, Pramoda K. Nayak, Seong In Yoon, Hyunseob Lim, Hyun-Joon Shin, and Hyeon Suk Shin. Prevention of Transition Metal Dichalcogenide Photodegradation by Encapsulation with h-BN Layers. *ACS Nano*, 10(9):8973–8979, sep 2016.
- [130] Henrik Mantynen, Nicklas Anttu, Zhipai Sun, and Harri Lipsanen. Single-photon sources with quantum dots in III-V nanowires. *Nanophotonics*, 8(5):747–769, 2019.

- [131] M. Heiss, Y. Fontana, A. Gustafsson, G. Wüst, C. Magen, D. D. O'Regan, J. W. Luo, B. Ketterer, S. Conesa-Boj, A. V. Kuhlmann, J. Houel, E. Russo-Averchi, J. R. Morante, M. Cantoni, N. Marzari, J. Arbiol, A. Zunger, R. J. Warburton, A. Fontcuberta I Morral, G. Wust, C. Magen, D. D. O'Regan, J. W. Luo, B. Ketterer, S. Conesa-Boj, A. V. Kuhlmann, J. Houel, E. Russo-Averchi, J. R. Morante, M. Cantoni, N. Marzari, J. Arbiol, A. Zunger, R. J. Warburton, and A. Fontcuberta I Morral. Self-assembled quantum dots in a nanowire system for quantum photonics. *Nature Materials*, 12(5):439–444, feb 2013.
- [132] Nikolay Panev, Ann I. Persson, Niklas Sköld, and Lars Samuelson. Sharp exciton emission from single InAs quantum dots in GaAs nanowires. *Applied Physics Letters*, 83(11):2238–2240, 2003.
- [133] Sofiane Haffouz, Katharina D. Zeuner, Dan Dalacu, Philip J. Poole, Jean Lapointe, Daniel Poitras, Khaled Mnaymneh, Xiaohua Wu, Martin Couillard, Marek Korkusinski, Eva Schöll, Klaus D. Jöns, Valery Zwiller, and Robin L. Williams. Bright Single InAsP Quantum Dots at Telecom Wavelengths in Position-Controlled InP Nanowires: The Role of the Photonic Waveguide. *Nano Letters*, 18(5):3047–3052, may 2018.
- [134] Dan Dalacu, Khaled Mnaymneh, Xiaohua Wu, Jean Lapointe, Geof C. Aers, Philip J. Poole, and Robin L. Williams. Selective-area vapor-liquid-solid growth of tunable InAsP quantum dots in nanowires. *Applied Physics Letters*, 98(25), 2011.
- [135] Richard Nötzel, J Temmyo, A Kozen, T Tamamura, T Fukui, H Hasegawa, and Semiconductor Science. Self-organized growth of quantum-dot structures. *Solid-State Electronics*, 40(10):1365–1379, jan 1996.
- [136] A Fontcuberta I Morral. Gold-free GaAs nanowire synthesis and optical properties. *IEEE Journal on Selected Topics in Quantum Electronics*, 17(4):819–828, 2011.
- [137] P.C. McIntyre and A. Fontcuberta i Morral. Semiconductor Nanowires: To Grow or Not to Grow? *Materials Today Nano*, 9:100058, mar 2019.
- [138] Z. X. Yan and A. G. Milnes. Deep Level Transient Spectroscopy of Silver and Gold Levels in LEC Grown Gallium Arsenide. *Journal of The Electrochemical Society*, 129(6):1353, 1982.
- [139] Kimberly A. Dick, Suneel Kodambaka, Mark C. Reuter, Knut Deppert, Lars Samuelson, Werner Seifert, L. Reine Wallenberg, and Frances M. Ross. The Morphology of Axial and Branched Nanowire Heterostructures. *Nano Letters*, 7(6):1817–1822, jun 2007.
- [140] Xuezhe Yu, Hailong Wang, Jun Lu, Jianhua Zhao, Jennifer Misuraca, Peng Xiong, and Stephan Von Molnár. Evidence for structural phase transitions induced by the triple phase line shift in self-catalyzed GaAs nanowires. *Nano Letters*, 12(10):5436–5442, 2012.
- [141] J Tersoff. Stable Self-Catalyzed Growth of III-V Nanowires. *Nano Letters*, 15(10):6609–6613, 2015.

Bibliography

- [142] V. G. Dubrovskii, T. Xu, A. Díaz Álvarez, S. R. Plissard, P. Caroff, F. Glas, and B. Grandidier. Self-Equilibration of the Diameter of Ga-Catalyzed GaAs Nanowires. *Nano Letters*, 15(8):5580–5584, aug 2015.
- [143] Daniel Rudolph, Lucas Schweickert, Stefanie Morkötter, Lukas Hanschke, Simon Hertenberger, Max Bichler, Gregor Koblmüller, Gerhard Abstreiter, and Jonathan J. Finley. Probing the trapping and thermal activation dynamics of excitons at single twin defects in GaAs-AlGaAs core-shell nanowires. *New Journal of Physics*, 15, 2013.
- [144] Nari Jeon, Daniel Ruhstorfer, Markus Döblinger, Sonja Matich, Bernhard Loitsch, Gregor Koblmüller, and Lincoln Lauhon. Connecting Composition-Driven Faceting with Facet-Driven Composition Modulation in GaAs-AlGaAs Core-Shell Nanowires. *Nano Letters*, 18(8):5179–5185, aug 2018.
- [145] J G Belk, D W Pashley, C F McConville, J L Sudijono, B A Joyce, and T S Jones. Surface atomic configurations due to dislocation activity in InAs/GaAs(110) heteroepitaxy. *Phys. Rev. B*, 56(16):10289–10296, oct 1997.
- [146] Emmanouil Dimakis, Uwe Jahn, Manfred Ramsteiner, Abbes Tahraoui, Javier Grandal, Xiang Kong, Oliver Marquardt, Achim Trampert, Henning Riechert, and Lutz Geelhaar. Coaxial multishell (In,Ga)As/GaAs nanowires for near-infrared emission on Si substrates. *Nano Letters*, 14(5):2604–2609, 2014.
- [147] Ryan B. Lewis, Pierre Corfdir, Jesús Herranz, Hanno Küpers, Uwe Jahn, Oliver Brandt, and Lutz Geelhaar. Self-Assembly of InAs Nanostructures on the Sidewalls of GaAs Nanowires Directed by a Bi Surfactant. *Nano Letters*, 17(7):4255–4260, 2017.
- [148] Jonas Lähnemann, Megan O. Hill, Jesús Herranz, Oliver Marquardt, Guanhui Gao, Ali Al Hassan, Arman Davtyan, Stephan O. Hruszkewycz, Martin V. Holt, Chunyi Huang, Irene Calvo-Almazán, Uwe Jahn, Ullrich Pietsch, Lincoln J. Lauhon, and Lutz Geelhaar. Correlated nanoscale analysis of the emission from wurtzite versus zincblende (In,Ga)As/GaAs nanowire core-shell quantum wells. *Nano Letters*, 19(7):4448–4457, 2019.
- [149] Emanuele Uccelli, Jordi Arbiol, Joan Ramon Morante, Anna Fontcuberta I Morral, a F I Morral, and Anna Fontcuberta I Morral. InAs quantum dot arrays decorating the facets of GaAs nanowires. *ACS Nano*, 4(10):5985–5993, 2010.
- [150] Ryan B. Lewis, Lars Nicolai, Hanno Küpers, Manfred Ramsteiner, Achim Trampert, and Lutz Geelhaar. Anomalous Strain Relaxation in Core-Shell Nanowire Heterostructures via Simultaneous Coherent and Incoherent Growth. *Nano letters*, 17(1):136–142, 2017.
- [151] Bin Yang, Feng Liu, and M G Lagally. Local Strain-Mediated Chemical Potential Control of Quantum Dot Self-Organization in Heteroepitaxy. *Physical Review Letters*, 92(2):4, 2004.

-
- [152] Saniya Deshpande, Junseok Heo, Ayan Das, and Pallab Bhattacharya. Electrically driven polarized single-photon emission from an InGaN quantum dot in a GaN nanowire. *Nature Communications*, 4, 2013.
- [153] Magnus T. Borgström, Valery Zwiller, Elisabeth Müller, and Atac Imamoglu. Optically bright quantum dots in single nanowires. *Nano Letters*, 5(7):1439–1443, 2005.
- [154] Iman Esmaeil Zadeh, Ali W. Elshaari, Klaus D. Jöns, Andreas Fognini, Dan Dalacu, Philip J. Poole, Michael E. Reimer, and Val Zwiller. Deterministic Integration of Single Photon Sources in Silicon Based Photonic Circuits. *Nano Letters*, 16(4):2289–2294, apr 2016.
- [155] Matěj Velický, Gavin E. Donnelly, William R. Hendren, Stephen McFarland, Declan Scullion, William J.I. Debenedetti, Gabriela Calinao Correa, Yimo Han, Andrew J. Wain, Melissa A. Hines, David A. Muller, Kostya S. Novoselov, Héctor D. Abruna, Robert M. Bowman, Elton J.G. Santos, and Fumin Huang. Mechanism of Gold-Assisted Exfoliation of Centimeter-Sized Transition-Metal Dichalcogenide Monolayers. *ACS Nano*, 2018.
- [156] Pulickel Ajayan, Philip Kim, and Kaustav Banerjee. Two-dimensional van der Waals materials. *Phys. Today*, 69(9):38–44, sep 2016.
- [157] Oriol Lopez-Sanchez, Dominik Lembke, Metin Kayci, Aleksandra Radenovic, and Andras Kis. Ultrasensitive photodetectors based on monolayer MoS₂. *Nat. Nanotechnol.*, 8(7):497–501, jul 2013.
- [158] Jason S. Ross, Philip Klement, Aaron M. Jones, Nirmal J. Ghimire, Jiaqiang Yan, D. G. Mandrus, Takashi Taniguchi, Kenji Watanabe, Kenji Kitamura, Wang Yao, David H. Cobden, and Xiaodong Xu. Electrically tunable excitonic light-emitting diodes based on monolayer WSe₂ p-n junctions. *Nat. Nanotechnol.*, 9(4):268–272, apr 2014.
- [159] F. Withers, O. Del Pozo-Zamudio, A. Mishchenko, A. P. Rooney, A. Gholinia, K. Watanabe, T. Taniguchi, S. J. Haigh, A. K. Geim, A. I. Tartakovskii, and K. S. Novoselov. Light-emitting diodes by band-structure engineering in van der Waals heterostructures. *Nat. Mater.*, 14(3):301–306, 2015.
- [160] Changli Li, Qi Cao, Faze Wang, Yequan Xiao, Yanbo Li, Jean Jacques Delaunay, and Hongwei Zhu. Engineering graphene and TMDs based van der Waals heterostructures for photovoltaic and photoelectrochemical solar energy conversion. *Chem. Soc. Rev.*, 47(13):4981–5037, 2018.
- [161] Hannu Häkkinen. The gold–sulfur interface at the nanoscale. *Nat. Chem.*, 4(6):443–455, jun 2012.
- [162] Wenjie Liang, Marc Bockrath, Dolores Bozovic, Jason H. Hafner, M. Tinkham, and Hongkun Park. Fabry - Perot interference in a nanotube electron waveguide. *Nature*, 411(6838):665–669, jun 2001.

Bibliography

- [163] Adrien Allain, Jiahao Kang, Kaustav Banerjee, and Andras Kis. Electrical contacts to two-dimensional semiconductors. *Nat. Mater.*, 14(12):1195–1205, dec 2015.
- [164] Na Xin, Jianxin Guan, Chenguang Zhou, Xinjian Chen, Chunhui Gu, Yu Li, Mark A. Ratner, Abraham Nitzan, J. Fraser Stoddart, and Xuefeng Guo. Concepts in the design and engineering of single-molecule electronic devices. *Nat. Rev. Phys.*, 1(3):211–230, mar 2019.
- [165] Manuel Cardona and Gernot Güntherodt, editors. *Light Scattering in Solids II*, volume 50 of *Topics in Applied Physics*. Springer Berlin Heidelberg, Berlin, Heidelberg, 1982.
- [166] Hong Li, Qing Zhang, Chin Chong Ray Yap, Beng Kang Tay, Teo Hang Tong Edwin, Aurelien Olivier, and Dominique Baillargeat. From bulk to monolayer MoS₂: Evolution of Raman scattering. *Advanced Functional Materials*, 22(7):1385–1390, 2012.
- [167] Andrea C. Ferrari and Denis M. Basko. Raman spectroscopy as a versatile tool for studying the properties of graphene. *Nat. Nanotechnol.*, 8(4):235–246, 2013.
- [168] Marcel Placidi, Mirjana Dimitrievska, Victor Izquierdo-Roca, Xavier Fontané, Andres Castellanos-Gomez, Amador Pérez-Tomás, Narcis Mestres, Moises Espindola-Rodriguez, Simon López-Marino, Markus Neuschitzer, Veronica Bermudez, Anatoliy Yaremko, and Alejandro Pérez-Rodríguez. Multiwavelength excitation Raman scattering analysis of bulk and two-dimensional MoS₂: Vibrational properties of atomically thin MoS₂ layers. *2D Materials*, 2(3):035006, jul 2015.
- [169] Mingyuan Huang, Huguen Yan, Tony F. Heinz, and James Hone. Probing strain-induced electronic structure change in graphene by Raman spectroscopy. *Nano Lett.*, 10(10):4074–4079, 2010.
- [170] Nedjma Bendiab, Julien Renard, Cornelia Schwarz, Antoine Reserbat-Plantey, Léo Djehvahirdjian, Vincent Bouchiat, Johann Coraux, and Laëtitia Marty. Unravelling external perturbation effects on the optical phonon response of graphene. *J. Raman Spectrosc.*, 49(1):130–145, 2018.
- [171] Ryan Beams, Luiz Gustavo Cançado, and Lukas Novotny. Raman characterization of defects and dopants in graphene. *J. Phys. Condens. Matter*, 27(8), 2015.
- [172] R. Saito, Y. Tatsumi, S. Huang, X. Ling, and M. S. Dresselhaus. Raman spectroscopy of transition metal dichalcogenides. *J. Phys. Condens. Matter*, 28(35), 2016.
- [173] Da Young Hwang and Dong Hack Suh. Evolution of a high local strain in rolling up MoS₂ sheets decorated with Ag and Au nanoparticles for surface-enhanced Raman scattering. *Nanotechnology*, 28(2), 2017.
- [174] Yan Aung Moe, Yinghui Sun, Huanyu Ye, Kai Liu, and Rongming Wang. Probing Evolution of Local Strain at MoS₂ -Metal Boundaries by Surface-Enhanced Raman Scattering. *ACS Appl. Mater. Interfaces*, 10(46):40246–40254, nov 2018.

- [175] Kabeer Jasuja and Vikas Berry. Implantation and Growth of Dendritic Gold Nanostructures on Graphene Derivatives: Electrical Property Tailoring and Raman Enhancement. *ACS Nano*, 3(8):2358–2366, aug 2009.
- [176] Michele Buscema, Gary A. Steele, Herre S. J. van der Zant, and Andres Castellanos-Gomez. The effect of the substrate on the Raman and photoluminescence emission of single-layer MoS₂. *Nano Res.*, 7(4):561–571, apr 2014.
- [177] Yi Zeng, Xing Li, Weibing Chen, Jianhui Liao, Jun Lou, and Qing Chen. Highly Enhanced Photoluminescence of Monolayer MoS₂ with Self-Assembled Au Nanoparticle Arrays. *Advanced Materials Interfaces*, 4(21):1700739, nov 2017.
- [178] Xiaozhuo Qi, Tsz Wing Lo, Di Liu, Lantian Feng, Yang Chen, Yunkun Wu, Hongliang Ren, Guang-Can Guo, Dangyuan Lei, and Xifeng Ren. Effects of gap thickness and emitter location on the photoluminescence enhancement of monolayer MoS₂ in a plasmonic nanoparticle-film coupled system. *Nanophotonics*, 9(7):2097–2105, jul 2020.
- [179] Udai Bhanu, Muhammad R. Islam, Laurene Tetard, and Saiful I. Khondaker. Photoluminescence quenching in gold - MoS₂ hybrid nanoflakes. *Scientific Reports*, 4(1):5575, may 2015.
- [180] Preeti Garg, Radhapiyari Laishram, R. Raman, and R. K. Soni. Photoluminescence Quenching and SERS in Tri-layer MoS₂ Flakes. *Journal of Electronic Materials*, 48(9):5883–5890, sep 2019.
- [181] Tanmay Goswami, Renu Rani, Kiran Shankar Hazra, and Hirendra N. Ghosh. Ultrafast Carrier Dynamics of the Exciton and Trion in MoS₂ Monolayers Followed by Dissociation Dynamics in Au@MoS₂ 2D Heterointerfaces. *J. Phys. Chem. Lett.*, pages 3057–3063, 2019.
- [182] Hang Yin, Dafeng Hu, Xuemin Geng, Hu Liu, Yanfen Wan, Zhanhu Guo, and Peng Yang. 2D gold supercrystal-MoS₂ hybrids: Photoluminescence quenching. *Materials Letters*, 255:126531, nov 2019.
- [183] Thomas Pons, Igor L. Medintz, Kim E. Sapsford, Seiichiro Higashiya, Amy F. Grimes, Doug S. English, and Hedi Mattoussi. On the quenching of semiconductor quantum dot photoluminescence by proximal gold nanoparticles. *Nano Lett.*, 7(10):3157–3164, 2007.
- [184] Yinghui Sun, Yan Aung Moe, Yingying Xu, Yufei Sun, Xuewen Wang, Fangtao Li, Kai Liu, and Rongming Wang. Evolution of local strain in Ag-deposited monolayer MoS₂ modulated by interface interactions. *Nanoscale*, 11(46):22432–22439, 2019.
- [185] Mark A. Bissett, Masaharu Tsuji, and Hiroki Ago. Strain engineering the properties of graphene and other two-dimensional crystals. *Phys. Chem. Chem. Phys.*, 16(23):11124–11138, 2014.
- [186] Jae Ung Lee, Sungjong Woo, Jaesung Park, Hee Chul Park, Young Woo Son, and Hyeonsik Cheong. Strain-shear coupling in bilayer MoS. *Nat. Commun.*, 8(1), 2017.

Bibliography

- [187] C. R. Zhu, G. Wang, B. L. Liu, X. Marie, X. F. Qiao, X. Zhang, X. X. Wu, H. Fan, P. H. Tan, T. Amand, and B. Urbaszek. Strain tuning of optical emission energy and polarization in monolayer and bilayer MoS₂. *Phys. Rev. B - Condens. Matter Mater. Phys.*, 88(12):1–5, 2013.
- [188] Sebastian Heeg, Roberto Fernandez-Garcia, Antonios Oikonomou, Fred Schedin, Rohit Narula, Stefan A. Maier, Aravind Vijayaraghavan, and Stephanie Reich. Polarized Plasmonic Enhancement by Au Nanostructures Probed through Raman Scattering of Suspended Graphene. *Nano Lett.*, 13(1):301–308, jan 2013.
- [189] János Pető, Gergely Dobrik, Gergő Kukucska, Péter Vancsó, Antal A. Koós, János Koltai, Péter Nemes-Incze, Chanyong Hwang, and Levente Tapasztó. Moderate strain induced indirect bandgap and conduction electrons in MoS₂ single layers. *npj 2D Materials and Applications*, 3(1):39, dec 2019.
- [190] Jong Hun Kim, Jinhwan Lee, Jae Hyeon Kim, C. C. Hwang, Changgu Lee, and Jeong Young Park. Work function variation of MoS₂ atomic layers grown with chemical vapor deposition: The effects of thickness and the adsorption of water/oxygen molecules. *Appl. Phys. Lett.*, 106(25), 2015.
- [191] David W.H. Rankin. CRC handbook of chemistry and physics, 89th edition, edited by David R. Lide. *Crystallogr. Rev.*, 15(3):223–224, jul 2009.
- [192] Cindy S. Merida, Duy Le, Elena M. Echeverria, Ariana E. Nguyen, Takat B. Rawal, Sahar Naghibi Alvillar, Viktor Kandyba, Abdullah Al-Mahboob, Yaroslav Losovyy, Khabiboulakh Katsiev, Michael D. Valentin, Chun-Yu Huang, Michael J. Gomez, I-Hsi Lu, Alison Guan, Alexei Barinov, Talat S. Rahman, Peter A. Dowben, and Ludwig Bartels. Gold Dispersion and Activation on the Basal Plane of Single-Layer MoS₂. *J. Phys. Chem. C*, 122(1):267–273, jan 2018.
- [193] Yingang Gui, Wenlong Chen, Yuncai Lu, Chao Tang, and Lingna Xu. Au Catalyst-Modified MoS₂ Monolayer as a Highly Effective Adsorbent for SO₂ Gas: A DFT Study. *ACS Omega*, 4(7):12204–12211, jul 2019.
- [194] Roberto Sant, Simone Lisi, Van Dung Nguyen, Estelle Mazaleyrat, Ana Cristina Gómez Herrero, Olivier Geaymond, Valérie Guisset, Philippe David, Alain Marty, Matthieu Jamet, Claude Chapelier, Laurence Magaud, Yannick J. Dappe, Marco Bianchi, Philip Hofmann, Gilles Renaud, and Johann Coraux. Decoupling Molybdenum Disulfide from Its Substrate by Cesium Intercalation. *J. Phys. Chem. C*, 124(23):12397–12408, jun 2020.
- [195] Guochao Qian, Qingjun Peng, Dexu Zou, Shan Wang, Bing Yan, and Qu Zhou. First-Principles Insight Into Au-Doped MoS₂ for Sensing C₂H₆ and C₂H₄. *Front. Mater.*, 7(February):1–9, feb 2020.
- [196] Ruichun Luo, Wen Wu Xu, Yongzheng Zhang, Ziqian Wang, Xiaodong Wang, Yi Gao, Pan Liu, and Mingwei Chen. Van der Waals interfacial reconstruction in monolayer

- transition-metal dichalcogenides and gold heterojunctions. *Nat. Commun.*, 11(1):1–12, dec 2020.
- [197] Bastian Miller, Jessica Lindlau, Max Bommert, Andre Neumann, Hisato Yamaguchi, Alexander Holleitner, Alexander Högele, and Ursula Wurstbauer. Tuning the Fröhlich exciton-phonon scattering in monolayer MoS₂. *Nat. Commun.*, 10(1):807, dec 2019.
- [198] Thibault Sohler, Evgeniy Ponomarev, Marco Gibertini, Helmuth Berger, Nicola Marzari, Nicolas Ubrig, and Alberto F. Morpurgo. Enhanced Electron-Phonon Interaction in Multivalley Materials. *Phys. Rev. X*, 9(3):31019, 2019.
- [199] Michele Lazzeri and Francesco Mauri. Nonadiabatic Kohn anomaly in a doped graphene monolayer. *Phys. Rev. Lett.*, 97(26):29–32, 2006.
- [200] A. Marco Saitta, Michele Lazzeri, Matteo Calandra, and Francesco Mauri. Giant nonadiabatic effects in layer metals: Raman spectra of intercalated graphite explained. *Phys. Rev. Lett.*, 100(22):1–4, 2008.
- [201] Matteo Calandra, Gianni Profeta, and Francesco Mauri. Adiabatic and nonadiabatic phonon dispersion in a Wannier function approach. *Phys. Rev. B - Condens. Matter Mater. Phys.*, 82(16):1–16, 2010.
- [202] Francesco Tumino, Carlo Spartaco Casari, Andrea Li Bassi, and Sergio Tosoni. Nature of Point Defects in Single-Layer MoS₂ Supported on Au(111). *J. Phys. Chem. C*, 124(23):12424–12431, jun 2020.
- [203] Zhennan Kou, Arsalan Hashemi, Martti J. Puska, Arkady V. Krasheninnikov, and Hannu-Pekka Komsa. Simulating Raman spectra by combining first-principles and empirical potential approaches with application to defective MoS₂. *npj Comput. Mater.*, 6(1):59, dec 2020.
- [204] Sandro Mignuzzi, Andrew J. Pollard, Nicola Bonini, Barry Brennan, Ian S. Gilmore, Marcos A. Pimenta, David Richards, and Debdulal Roy. Effect of disorder on Raman scattering of single-layer MoS_2 . *Phys. Rev. B*, 91(19):195411, may 2015.
- [205] Xin Zhang, Xiao-Fen Fen Qiao, Wei Shi, Jiang-Bin Bin Wu, De-Sheng Sheng Jiang, and Ping-Heng Heng Tan. Phonon and Raman scattering of two-dimensional transition metal dichalcogenides from monolayer, multilayer to bulk material. *Chem. Soc. Rev.*, 44(9):2757–2785, 2015.
- [206] William M. Parkin, Adrian Balan, Liangbo Liang, Paul Masih Das, Michael Lamparski, Carl H. Naylor, Julio A. Rodríguez-Manzo, A. T. Charlie Johnson, Vincent Meunier, and Marija Drndić. Raman Shifts in Electron-Irradiated Monolayer MoS₂. *ACS Nano*, 10(4):4134–4142, apr 2016.

Bibliography

- [207] Soungmin Bae, Natsuki Sugiyama, Takatoshi Matsuo, Hannes Raebiger, Ken-ichi Shudo, and Koichi Ohno. Defect-Induced Vibration Modes of Ar^+MoS_2 -Irradiated MoS_2 . *Phys. Rev. Appl.*, 7(2):024001, feb 2017.
- [208] Pierce Maguire, Daniel S. Fox, Yangbo Zhou, Qianjin Wang, Maria O’Brien, Jakub Jadwiszczak, Conor P. Cullen, John McManus, Samuel Bateman, Niall McEvoy, Georg S. Duesberg, and Hongzhou Zhang. Defect sizing, separation, and substrate effects in ion-irradiated monolayer two-dimensional materials. *Phys. Rev. B*, 98(13), 2018.
- [209] Francesca Amaduzzi, Esther Alarcón-Lladó, Hubert Hautmann, Rawa Tanta, Federico Matteini, Gözde Tütüncüoğlu, Tom Vösch, Jesper Nygård, Thomas Jespersen, Emanuele Uccelli, and Anna Fontcuberta i Morral. Tuning the response of non-allowed Raman modes in GaAs nanowires. *J. Phys. D: Appl. Phys.*, 49(9):095103, mar 2016.
- [210] M Heiss, E Russo-Averchi, A Dalmau-Mallorquí, G Tütüncüoğlu, F Matteini, D Ruffer, S Conesa-Boj, O Demichel, E Alarcon-Lladó, and A Fontcuberta i Morral. III–V nanowire arrays: growth and light interaction. *Nanotechnology*, 25(1):014015, jan 2014.
- [211] Frank Schreiber. Structure and growth of self-assembling monolayers. *Prog. Surf. Sci.*, 65(5-8):151–257, nov 2000.
- [212] J. Christopher Love, Lara A. Estroff, Jennah K. Kriebel, Ralph G. Nuzzo, and George M. Whitesides. Self-Assembled Monolayers of Thiolates on Metals as a Form of Nanotechnology. *Chem. Rev.*, 105(4):1103–1170, apr 2005.
- [213] Damian L. Kokkin, Ruohan Zhang, Timothy C. Steimle, Ian A. Wyse, Bradley W. Pearlman, and Thomas D. Varberg. Au–S Bonding Revealed from the Characterization of Diatomic Gold Sulfide, AuS. *J. Phys. Chem. A*, 119(48):11659–11667, dec 2015.
- [214] Thomas Bürgi. Properties of the gold–sulphur interface: from self-assembled monolayers to clusters. *Nanoscale*, 7(38):15553–15567, 2015.
- [215] Igor Popov, Gotthard Seifert, and David Tománek. Designing electrical contacts to MoS_2 Monolayers: A computational study. *Phys. Rev. Lett.*, 108(15):1–5, 2012.
- [216] Brandon T. Blue, Glenn G. Jernigan, Duy Le, Jose J. Fonseca, Stephanie D. Lough, Jesse E. Thompson, Darian D. Smalley, Talat S. Rahman, Jeremy T. Robinson, and Masahiro Ishigami. Metallicity of 2H-MoS_2 induced by Au hybridization. *2D Mater.*, 7(2), 2020.
- [217] He Liu, Daniel Grasseschi, Akhil Dodda, Kazunori Fujisawa, David Olson, Ethan Kahn, Fu Zhang, Tianyi Zhang, Yu Lei, Ricardo Braga Nogueira Branco, Ana Laura Elías, Rodolfo Cruz Silva, Yin Ting Yeh, Camila M. Maroneze, Leandro Seixas, Patrick Hopkins, Saptarshi Das, Christiano J.S. de Matos, and Mauricio Terrones. Spontaneous chemical

- functionalization via coordination of Au single atoms on monolayer MoS₂. *Sci. Adv.*, 6(49), 2020.
- [218] Arsalan Hashemi, Arkady V. Krasheninnikov, Martti Puska, and Hannu-Pekka Komsa. Efficient method for calculating Raman spectra of solids with impurities and alloys and its application to two-dimensional transition metal dichalcogenides. *Phys. Rev. Mater.*, 3(2):023806, feb 2019.
- [219] Hans Tornatzky, Roland Gillen, Hiroshi Uchiyama, and Janina Maultzsch. Phonon dispersion in MoS_2 . *Phys. Rev. B*, 99(14):144309, apr 2019.
- [220] Andrea C. Ferrari. Raman spectroscopy of graphene and graphite: Disorder, electron-phonon coupling, doping and nonadiabatic effects. *Solid State Commun.*, 143(1-2):47–57, jul 2007.
- [221] Xuanye Wang, Jason W. Christopher, and Anna K. Swan. 2D Raman band splitting in graphene: Charge screening and lifting of the K-point Kohn anomaly. *Sci. Rep.*, 7(1):1–9, 2017.
- [222] A. Molina-Sánchez and L. Wirtz. Phonons in single-layer and few-layer MoS₂ and WS₂. *Phys. Rev. B - Condens. Matter Mater. Phys.*, 84(15):1–8, 2011.
- [223] Weiwei Zhao, Qisheng Wu, Qi Hao, Jinlan Wang, Mei Li, Yan Zhang, Kedong Bi, Yunfei Chen, and Zhenhua Ni. Plasmon-phonon coupling in monolayer WS₂. *Appl. Phys. Lett.*, 108(13), 2016.
- [224] Mark W. Knight, Nicholas S. King, Lifei Liu, Henry O. Everitt, Peter Nordlander, and Naomi J. Halas. Aluminum for plasmonics. *ACS Nano*, 8(1):834–840, 2014.
- [225] Yael Gutiérrez, Rodrigo Alcaraz de la Osa, Dolores Ortiz, José María Saiz, Francisco González, and Fernando Moreno. Plasmonics in the ultraviolet with aluminum, gallium, magnesium and rhodium. *Appl. Sci.*, 8(1):64, jan 2018.
- [226] Vijay K. Agarwala and Tomlinson Fort. Nature of the stable oxide layer formed on an aluminum surface by work function measurements. *Surf. Sci.*, 54(1):60–70, jan 1976.
- [227] Jiahuang Jian, Yang Li, Hai Bi, Xinzhu Wang, Xiaohong Wu, and Wei Qin. Aluminum Decoration on MoS₂ Ultrathin Nanosheets for Highly Efficient Hydrogen Evolution. *ACS Sustain. Chem. Eng.*, 8(11):4547–4554, mar 2020.
- [228] Matthias Drüppel, Thorsten Deilmann, Peter Krüger, and Michael Rohlfing. Diversity of trion states and substrate effects in the optical properties of an MoS₂ monolayer. *Nat. Commun.*, 8(1):2117, dec 2017.
- [229] Hyung Kim and Dong Lee. Near-Infrared-Responsive Cancer Photothermal and Photodynamic Therapy Using Gold Nanoparticles. *Polymers (Basel)*, 10(9):961, aug 2018.

Bibliography

- [230] Hailong Hu, Huigao Duan, Joel K. W. Yang, and Ze Xiang Shen. Plasmon-Modulated Photoluminescence of Individual Gold Nanostructures. *ACS Nano*, 6(11):10147–10155, nov 2012.
- [231] B. Radisavljevic, A. Radenovic, J. Brivio, V. Giacometti, and A. Kis. Single-layer MoS₂ transistors. *Nat. Nanotechnol.*, 6(3):147–150, mar 2011.
- [232] Meng-Lin Tsai, Sheng-Han Su, Jan-Kai Chang, Dung-Sheng Tsai, Chang-Hsiao Chen, Chih-I Wu, Lain-Jong Li, Lih-Juann Chen, and Jr-Hau He. Monolayer MoS₂ Heterojunction Solar Cells. *ACS Nano*, 8(8):8317–8322, aug 2014.
- [233] Alexey Chernikov, Timothy C. Berkelbach, Heather M. Hill, Albert Rigosi, Yilei Li, Ozgur Burak Aslan, David R. Reichman, Mark S. Hybertsen, and Tony F. Heinz. Exciton Binding Energy and Nonhydrogenic Rydberg Series in Monolayer WS_2 . *Phys. Rev. Lett.*, 113(7):076802, aug 2014.
- [234] John R. Schaibley, Hongyi Yu, Genevieve Clark, Pasqual Rivera, Jason S. Ross, Kyle L. Seyler, Wang Yao, and Xiaodong Xu. Valleytronics in 2D materials. *Nat. Rev. Mater.*, 1(11), 2016.
- [235] Riccardo Frisenda, Yue Niu, Patricia Gant, Aday J. Molina-Mendoza, Robert Schmidt, Rudolf Bratschitsch, Jinxin Liu, Lei Fu, Dumitru Dumcenco, Andras Kis, David Perez De Lara, and Andres Castellanos-Gomez. Micro-reflectance and transmittance spectroscopy: A versatile and powerful tool to characterize 2D materials. *Journal of Physics D: Applied Physics*, 50(7), 2017.
- [236] Antoine Reserbat-Plantey, Dipankar Kalita, Zheng Han, Laurence Ferlazzo, Sandrine Autier-Laurent, Katsuyoshi Komatsu, Chuan Li, Raphaël Weil, Arnaud Ralko, Laëtitia Marty, Sophie Guéron, Nedjma Bendjab, Hélène Bouchiat, and Vincent Bouchiat. Strain superlattices and macroscale suspension of graphene induced by corrugated substrates. *Nano Letters*, 14(9):5044–5051, 2014.
- [237] Julien Chaste, Amine Missaoui, Si Huang, Hugo Henck, Zeineb Ben Aziza, Laurence Ferlazzo, Carl Naylor, Adrian Balan, Alan T. Charlie Johnson, Rémy Braive, and Abdelkarim Ouerghi. Intrinsic Properties of Suspended MoS₂ on SiO₂/Si Pillar Arrays for Nanomechanics and Optics. *ACS Nano*, 12(4):3235–3242, 2018.
- [238] Mounika Vutukuru, Hossein Ardekani, Zhuofa Chen, Ryan L. Wilmington, Kenan Gundogdu, and Anna K. Swan. Enhanced Dielectric Screening and Photoluminescence from Nanopillar-Strained MoS₂ Nanosheets: Implications for Strain Funneling in Optoelectronic Applications. *ACS Appl. Nano Mater.*, 4(8):8101–8107, 2021.
- [239] Florian Dirnberger, Jonas D. Ziegler, Paulo E. Faria Junior, Rezlind Bushati, Takashi Taniguchi, Kenji Watanabe, Jaroslav Fabian, Dominique Bougeard, Alexey Chernikov,

- and Vinod M. Menon. Quasi-1D exciton channels in strain-engineered 2D materials. *Sci. Adv.*, 7(44), oct 2021.
- [240] Moshe G. Harats, Jan N. Kirchhof, Mengxiong Qiao, Kyrylo Greben, and Kirill I. Bolotin. Dynamics and efficient conversion of excitons to trions in non-uniformly strained monolayer WS₂. *Nature Photonics*, 14(5):324–329, 2020.
- [241] Lucas Güniat, Philippe Caroff, and Anna Fontcuberta I Morral. Vapor Phase Growth of Semiconductor Nanowires: Key Developments and Open Questions. *Chem. Rev.*, 119(15):8958–8971, 2019.
- [242] Wonjong Kim, Lucas Güniat, Anna Fontcuberta I Morral, and Valerio Piazza. Doping challenges and pathways to industrial scalability of III-V nanowire arrays. *Appl. Phys. Rev.*, 8(1), 2021.
- [243] Jelena Vukajlovic-Plestina, Wonjong Kim, Vladimir G. Dubrovski, Gözde Tütüncüoğlu, Maxime Lagier, Heidi Potts, Martin Friedl, and Anna Fontcuberta i Morral. Engineering the Size Distributions of Ordered GaAs Nanowires on Silicon. *Nano Lett.*, 17(7):4101–4108, jul 2017.
- [244] J. Vukajlovic-Plestina, W. Kim, L. Ghisalberti, G. Varnavides, G. Tütüncuoğlu, H. Potts, M. Friedl, L. Güniat, W. C. Carter, V. G. Dubrovskii, and A. Fontcuberta i Morral. Fundamental aspects to localize self-catalyzed III-V nanowires on silicon. *Nat. Commun.*, 10(1):869, 2019.
- [245] Keng-Ku Liu, Wenjing Zhang, Yi-Hsien Lee, Yu-Chuan Lin, Mu-Tung Chang, Ching-Yuan Su, Chia-Seng Chang, Hai Li, Yumeng Shi, Hua Zhang, Chao-Sung Lai, and Lain-Jong Li. Growth of Large-Area and Highly Crystalline MoS₂ Thin Layers on Insulating Substrates. *Nano Lett.*, 12(3):1538–1544, mar 2012.
- [246] T. L. Atallah, J. Wang, M. Bosch, D. Seo, R. A. Burke, O. Moneer, Justin Zhu, M. Theibault, L. E. Brus, J. Hone, and X.-Y. Zhu. Electrostatic Screening of Charged Defects in Monolayer MoS₂. *J. Phys. Chem. Lett.*, 8(10):2148–2152, may 2017.
- [247] Jason W. Christopher, Bennett B. Goldberg, and Anna K. Swan. Long tailed trions in monolayer MoS₂: Temperature dependent asymmetry and resulting red-shift of trion photoluminescence spectra. *Sci. Rep.*, 7(1):1–8, 2017.
- [248] Elmar Mitterreiter, Bruno Schuler, Ana Micevic, Daniel Hernangómez-Pérez, Katja Barthelmi, Katherine A. Cochrane, Jonas Kiemle, Florian Sigger, Julian Klein, Edward Wong, Edward S. Barnard, Kenji Watanabe, Takashi Taniguchi, Michael Lorke, Frank Jahnke, Johnathan J. Finley, Adam M. Schwartzberg, Diana Y. Qiu, Sivan Refaely-Abramson, Alexander W. Holleitner, Alexander Weber-Bargioni, and Christoph Kastl. The role of chalcogen vacancies for atomic defect emission in MoS₂. *Nat. Commun.*, 12(1):1–8, 2021.

Bibliography

- [249] Yuxuan Lin, Xi Ling, Lili Yu, Shengxi Huang, Allen L. Hsu, Yi Hsien Lee, Jing Kong, Mildred S. Dresselhaus, and Tomás Palacios. Dielectric screening of excitons and trions in single-layer MoS₂. *Nano Lett.*, 14(10):5569–5576, 2014.
- [250] Archana Raja, Andrey Chaves, Jaeun Yu, Ghidewon Arefe, Heather M. Hill, Albert F. Rigosi, Timothy C. Berkelbach, Philipp Nagler, Christian Schüller, Tobias Korn, Colin Nuckolls, James Hone, Louis E. Brus, Tony F. Heinz, David R. Reichman, and Alexey Chernikov. Coulomb engineering of the bandgap and excitons in two-dimensional materials. *Nature Communications*, 8(May):1–7, 2017.
- [251] Haiyan Nan, Zilu Wang, Wenhui Wang, Zheng Liang, Yan Lu, Qian Chen, Daowei He, Pingheng Tan, Feng Miao, Xinran Wang, Jinlan Wang, and Zhenhua Ni. Strong Photoluminescence Enhancement of MoS₂ through Defect Engineering and Oxygen Bonding. *ACS Nano*, 8(6):5738–5745, jun 2014.
- [252] Weitao Su, Honglei Dou, Jinwei Li, Dexuan Huo, Ning Dai, and Li Yang. Tuning photoluminescence of single-layer MoS₂ using H₂O₂. *RSC Adv.*, 5(101):82924–82929, 2015.
- [253] W. J. Moore and R. T. Holm. Infrared dielectric constant of gallium arsenide. *J. Appl. Phys.*, 80(12):6939–6942, 1996.
- [254] S.M. Sze and Kwok K. Ng. *Physics of Semiconductor Devices*. John Wiley & Sons, Inc., Hoboken, NJ, USA, oct 2006.
- [255] Andres Castellanos-Gomez, Michele Buscema, Rianda Molenaar, Vibhor Singh, Laurens Janssen, Herre S.J. Van Der Zant, and Gary A. Steele. Deterministic transfer of two-dimensional materials by all-dry viscoelastic stamping. *2D Materials*, 1(1), 2014.
- [256] J. Siejka, A. Morawski, J. Lagowski, and H. C. Gatos. Electric charge in GaAs native oxides: Annealing characteristics. *Appl. Phys. Lett.*, 38(7):552–554, 1981.
- [257] D. Leonard, K. Pond, and P. M. Petroff. Critical layer thickness for self-assembled InAs islands on GaAs. *Physical Review B*, 50(16):11687–11692, oct 1994.
- [258] L. G. Wang, P. Kratzer, N. Moll, and M. Scheffler. Size, shape, and stability of InAs quantum dots on the GaAs(001) substrate. *Physical Review B*, 62(3):1897–1904, jul 2000.

Akshay Balgarkashi – Curriculum Vitae

Route du Pont-Bleu 21
1023 Crissier, Switzerland
akshaybkiitb@gmail.com
+41 78 699 05 82

Google Scholar: [Akshay Balgarkashi](#)
ORCID: [0000-0003-0504-5542](#)

Personal Information
D.O.B: 16 November 1990
Nationality: Indian
Marital Status: Married

Education

- **PhD Candidate** (Materials Science and Engineering)
École Polytechnique Fédérale de Lausanne (EPFL), Switzerland [January 2018 - Present]
- **Master of Technology** (Electrical Engineering)
Indian Institute of Technology (IIT) Bombay, India [July 2013 - June 2016]
- **Bachelor of Engineering** (Electronics Engineering)
University of Mumbai, India [June 2008 - May 2012]

Research and Work Experience

- **Doctoral Assistant, Laboratory of Semiconductor Materials, EPFL** [January 2018 - present]
Switzerland
- *Marie-Curie ITN fellowship: Project LIMQUET*
- *Growth of InAs/GaAs nanowire heterostructures on Si*
- *Fabrication of hybrid nanowire/transition-metal dichalcogenide heterostructures*
- **Visiting Researcher, L2n, Université de Technologie de Troyes** [September 2018 - February 2020]
France
- *ITN LIMQUET Secondment: Advanced optical characterization of nanostructures*
- **Research Assistant, Cardiff University** [September 2016 - October 2017]
- *Design and growth of 1D nanobeam photonic crystal lasers on SOI platform*
- **Project Research Assistant, IIT Bombay** [July 2013 - June 2016]
- *Epitaxial growth of InAs/GaAs quantum dot heterostructures for infrared photodetection*
- **Junior Research Fellow, IIT Bombay** [August 2012 - July 2013]
- *Study of impact of rapid thermal annealing on InAs/GaAs quantum dot heterostructures using photoluminescence*

Key Publications

- **A. Balgarkashi**, Valerio Piazza, Jakub Jasinski, Riccardo Frisenda, Alessandro Surrente, Michał Baranowski, Didem Dede, Wonjong Kim, Lucas Güniat, Jean-Baptiste Leran, Andres Castellanos-Gomez, Paulina Plochocka and Anna Fontcuberta i Morral, "Spatial modulation of vibrational and luminescence properties of monolayer MoS₂ using a GaAs nanowire array" in preparation.

- M Dimitrievska*, **A Balgarkashi***, J Jiang, E Stutz, M Banerjee, A Fontcuberta i Morral, "On the origin of Raman peak splitting in monolayer 2D materials – metal interfaces: MoS₂/Au," in review.
- Lucas Güniat, Nicolas Tappy, **Akshay Balgarkashi**, Titouan Charvin, Raphaël Lemerle, Nicholas Morgan, Didem Dede, Wonjong Kim, Jean-Baptiste Leran, and Anna Fontcuberta i Morral, "Light emitting InGaAs Heterostructures on Si (100) integrated GaAs Nanospades" in review
- **A Balgarkashi***, S P Ramanandan*, N Tappy, M Nahra, W Kim, L Guniat, M Friedl, N Morgan, D Dede, J B Leran, C Couteau and A Fontcuberta i Morral, "Facet-driven formation of axial and radial In(Ga)As clusters in GaAs nanowires," Journal of Optics, Volume 22, Number 8, July 2020
- Eli Sutter, Jacob S. French, **Akshay Balgarkashi**, Nicolas Tappy, Anna Fontcuberta i Morral, Juan Carlos Idrobo, and Peter Sutter, "Single-Crystalline γ - Ga₂S₃ Nanotubes via Epitaxial Conversion of GaAs Nanowires," Nano Lett., 19, 12, 8903–8910, 2019
- Lucas Güniat, Sara Martí-Sánchez, Oscar Garcia, Mégane Boscardin, David Vindice, Nicolas Tappy, Martin Friedl, Wonjong Kim, Mahdi Zamani, Luca Francaviglia, **Akshay Balgarkashi**, Jean-Baptiste Leran, Jordi Arbiol, Anna Fontcuberta i Morral, "III–V Integration on Si(100): Vertical Nanospades," ACS Nano, no. 100, p. acsnano.9b01546, 2019.

Technical Skills

- **Growth and Fabrication**

Molecular beam epitaxy (MBE), Electron beam lithography, exfoliation and polymer transfer of 2D materials, wet etching, plasma-enhanced deposition and etching, e-beam evaporation

- **Characterization techniques**

Raman spectroscopy, Photoluminescence (PL), Cathodoluminescence (CL), Atomic force microscopy (AFM) Scanning and transmission electron microscopy (SEM and TEM) and Energy-dispersive X-ray spectroscopy (EDX)

- **Modeling/Software**

Lumerical FDTD, Origin, Python and JavaScript (intermediate), L^AT_EX, MS-Office, Blender, ImageJ, Adobe Illustrator

Institutional Responsibilities

- **EPFL**

Co-responsible for the operation and timely maintenance of a DCA P600 UHV cluster molecular beam epitaxy system.

Responsible for optical characterization setup: Training, technical and scientific assistance to users.

YUVA Indians Association

Logistics manager and events organization. Active committee member providing support to the Indian diaspora at EPFL.

- **Cardiff University**

Ground-up installation of a Veeco GEN 930 dual-chamber molecular beam epitaxy system.

- **IIT Bombay**

Responsible for operation and maintenance of Riber EPINEAT molecular beam epitaxy system.

Conferences and Additional Training

- **63rd Electronic Materials Conference (Oral presentation)** *[June 2021]*
"The impact of localized hot spots on the Raman response of monolayer MoS₂"
- **Nanowire Week, Pisa, Italy (Poster Presentation)** *[September 2019]*
"Localized emitters in self-catalyzed InAs/GaAs nanowire heterostructure arrays on silicon"
- **NCCR-QSIT Winter School, Arosa, Switzerland** *[February 2019]*
"Winter workshop on various aspects of quantum technologies"
- **LIMQUET Annual School, Brighton, UK** *[February 2019]*
"Winter school on various aspects of atomic physics, nano-optics and photonics"
- **LIMQUET Annual School, Nessebar, Bulgaria** *[September 2019]*
"Summer school on light-matter interfaces and coherent control strategies"
- **E. Fermi summer school, Varenna, Italy** *[July 2018]*
"Nanoscale Quantum Optics"
- **Certification course, EPFL Extension School** *[July 2020]*
"Thinking and Creating with Code," using python and JavaScript

Teaching and Supervision

- **Teaching Assistant:** Linear Algebra (Bachelors course, EPFL) *[Fall semester 2020-21]*
- **Masters Semester Project:** Elif Nur Dayi (EPFL) *[June 2021]*
"Strain Induced bandgap modulation of tungsten diselenide (WSe₂) monolayers"
- **Masters Semester Project:** Rachel Wong Min (EPFL) *[January 2021]*
"Integration of 2D materials on structured substrates"
- **Masters Semester Project:** Zsófia Sajó (EPFL) *[June 2020]*
"Design and characterization of nanowire based heterostructures"
- **Masters Thesis:** Santhanu Panikar Ramanandan (EPFL) *[January 2020]*
"Facet-drive formation of axial and radial In(Ga)As clusters in GaAs nanowires"
- **Masters Semester Project:** Pranav Kulkarni (EPFL) *[January 2020]*
"Statistical study of tip faceting and Indium droplets on top of Gallium Arsenide nanowire arrays"
- **Masters Semester Project:** Mohammadhossein Montazerian (EPFL) *[January 2019]*
"Growth of GaAs nanowires on monolayer graphene-on-silicon"

Extra-curricular

- **Languages**
Native: English, Kannada (mother tongue), Marathi, Hindi
Intermediate: French (A1/A2)
- **Sports**
Avid yoga practitioner, organized yoga workshops
Active member of Badminton and Tennis clubs